DEVELOPMENT OF SIGNAL AMPLIFIED IMMUNOASSAY FOR ADVANCED VIRUS DETECTION

DISSERTATION

DEVELOPMENT OF SIGNAL AMPLIFIED IMMUNOASSAY FOR ADVANCED VIRUS DETECTION

June 2022

Shizuoka University
Graduate School of Science and Technology,
Educational Division
Department of Bioscience

Indra Memdi Khoris

Content

Table of Content

Chapter 1

Introduction

Chapter 1. Introduction

1.1 Foodborne Infectious Disease Viruses

This well-known gastroenteritis norovirus (NoV) has been reported for its annual outbreak (Harrison and DiCaprio 2018). In 2015, the World Health Organization (WHO published the Foodborne Disease Burden Epidemiology Reference Group (FERG) for a comprehensive estimation of the global burden caused by foodborne illness (WHO 2015). The report estimated a global burden of up to 150 million dollars due to the foodborne disease by both viruses. Besides the heavy loss economically, considering the aging society, NoV, with its high infection, could be a life-threatening foodborne disease agent to the elderly in Japan (Ohfuji et al. 2019). Moreover, a wide range of food, from pork and beef to seashells, can be implicated in outbreaks. Contaminated raw ingredients can be distributed from very distant locations and used as ingredients in various food production, thereby increasing the potential for spreading infection and the impact of illness across the food industry (Bosch et al. 2018). Proper monitoring and reliable surveillance are essential to control the outbreak and achieve a green society, free from the unsafe food of infectious foodborne viruses.

This foodborne virus is the main pathogenic agent responsible for nonbacterial acute gastroenteritis (Patel et al. 2009). NoV commonly occurs annually in developed countries worldwide, such as East Asia, including Japan, South Korea, China, England, Russia, Australia, and the USA. NoV infection mostly had its outbreak from contaminated food industry during the winter season (de Graaf et al. 2015), and has been a serious concern to the public hygiene. According to the Surveillance Report February 2017 for infectious agents, the outbreak of gastroenteritis caused by NoV re-emerged in Japan in 2015 and 2016. NoV infects humans, targeting the epithelium of the gastrointestinal tract, specifically the small intestine. Although it is case-by-case, most clinical symptoms include diarrhea and vomiting; occasionally, fever,

headaches, and abdominal pain can be severe and last longer in low immune system individuals, such as young children and the elderly (Hall et al. 2011). NoV can infect a person at a low infectious dose of approximately 100 virus particles. The infections can spread quickly via food and water, including the stool and vomit of infected persons (Hwang et al. 2017; Yakes et al. 2013).

1.2 Airborne and Mutant-rich Infectious Disease Viruses

In the last decade, the global community has been disarmed upon the outbreak of infectious viruses, including the recent pandemic of SARS-CoV-2 (Petersen et al. 2020), annually occurring influenza virus (Zhang and Miller 2019) and deadly mosquitoes-borne viruses (Dahmana and Mediannikov 2020). The breakthrough effort in monitoring the viral outbreak has led to the innovation and growth of the nanobiosensor (Dang et al. 2020; Ganganboina et al. 2020d; Wu et al. 2019). In the escalating positive cases of SARS-CoV-2 infection, the challenge global in controlling influenza virus type A subtype H1N1 (IV/A/H1N1) and subtype H3N2 (IV/A/H3N2) as the major circulating subtypes of IV/A can be considered a serious risk for its continuing outbreak and sporadic infection with similar spatial and timeline period (Suzuki et al. 2019). And starting from 2011 (Ison 2011) to recently (Lampejo 2020), drug-resistances property was found on several subtypes of influenza viruses and has been continuing challenge for this "old and persistence" respiratory virus. These global issues have been the pictorial urgency of the need of prevention strategies and surveillance technology (Ganganboina et al. 2020b). Hence, a new strategy in virus detection is in demand to fight the rapid, mutating infectious viruses in their early stages for better hygiene control and medical treatments.

1.3 Diagnostic Assay for Infectious Disease Agents

ELISA is a diagnostic immunoassay using signal reporters, utilizing enzyme conjugated to an antibody to determine specific target analytes' presence. Antigens can be referred to as the analyte in an immunoassay, in the form of proteins, antibodies, viruses, drugs, and other molecules. Generally, they are selectively bound by their complementary immunoglobulins on a solid surface (direct or sandwich assay or capture assay) (**Figure 1.1**). It is well-known for its simplicity with a step-by-step procedure to determine the presence of the target analyte (Chen et al. 2018; Stern et al. 2010).

This method commonly uses horseradish peroxidase (HRP)-labeled immunoreagents to realize detection signals' amplification and identify target molecules (Ganganboina and Doong. 2018). These enzymes catalyze the oxidation of a chromogen by hydrogen peroxide (H_2O_2) (Aydin 2015), known as a colorimetric-based ELISA. The intensity of the visual signal corresponds to the number of antigens-antibody immuno-complexes formed. However, natural enzymes have critical limitations despite the catalytic efficiency, such as considerably challenging preparation, purification, and storage (Jiang et al., 2018). Moreover, its low sensitivity has been pointed out as a strong limitation in detecting viral agents, which are infectious in very low concentrations (Chen et al. 2018). This issue can be addressed by the signal amplification used in the platform (Ahmed et al. 2017a; Ramana et al. 1995). Some problems have emerged as these enzymes have high production costs and low stability in harsh conditions, such as pH and temperature (Li et al. 2018; Oaew et al. 2012). In addition to its physicochemical limitations, HRP demonstrates a reduction of its catalytic properties at high nitrites, phenol, or H_2O_2 (Baynton et al. 1994; Samuni et al. 2017). This limits the amplification degree for the sensing use and requires the alternative substitution. Answering the challenge of substituting enzymes, the rapid development of nanotechnology over the past decade has allowed us to witness a new perspective of conventional heterogeneous catalysts, thus offering

great opportunities for nanomaterial-based artificial enzymes (nanozymes) (Wang et al., 2018; Wei et al., 2020).

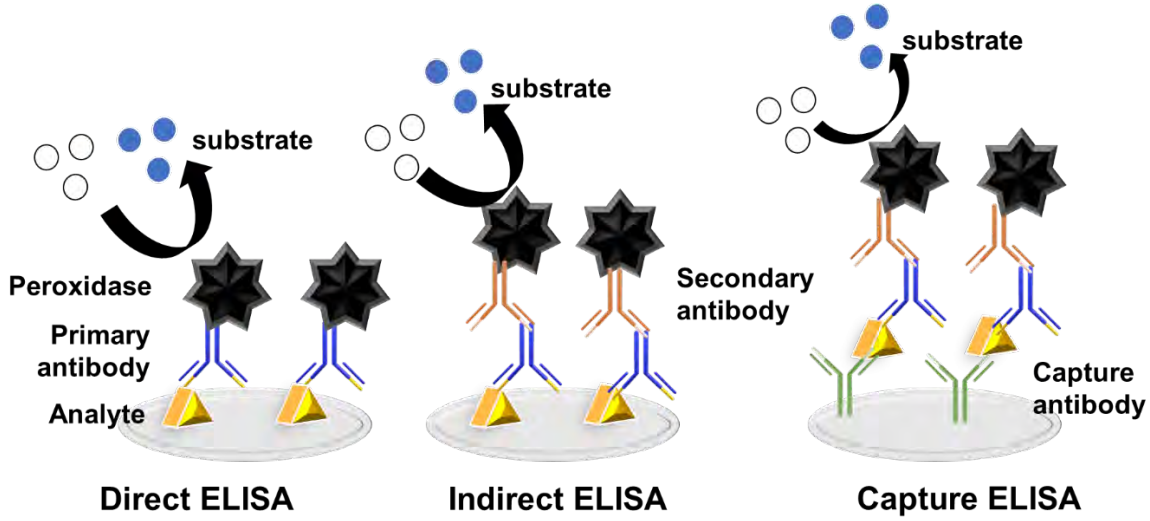

Figure 1.1 Type of ELISA

1.4 Nanozyme

Nanozymes are a class of nanomaterials whose catalytic activity mimics that of biological enzymes (Xia et al. 2015). Since the first discovery of Fe_3O_4 nanoparticles (NPs) exhibiting catalytic activity, more application with various kinds of nanozymes has been discovered, especially in biosensing technology (Ahmed et al. 2017a; Gao et al. 2007; Wang et al. 2018a). Nanomaterials have been shown to either enhance the activity of the coupled enzymes or exhibit robust enzymatic-like activity (Huang et al. 2019; Wu et al. 2016). Various nanomaterials have been investigated, such as metals such as gold (Au) (Wang et al. 2012), silver (Ag) (Karim et al. 2018) and platinum (Pt) (Fu et al. 2014)) and their derivatives, including metal sulfides and metal oxides (Dai et al. 2009), enzyme-conjugated metal nanostructures (Oh et al. 2018), and carbon-based nanostructures (Ahmed et al. 2016b; Zheng et al. 2013). Interestingly, hybrid nanomaterials, such as graphene/gold nanohybrid (Tao et al. 2013) gold-decorated organic framework (Pachfule et al. 2014) and bimetallic (Cheng et al. 2017; Dutta Chowdhury et al. 2017; Kuo et al. 2018; Russo et al. 2018) to trimetallic (Barman

et al. 2018; Kang et al. 2013) nanostructure demonstrated unique morphology and increasing catalytic activity significantly (Wang et al. 2018b). These nanomaterials exhibit tunable catalytic activity and are easily conjugated to most proteins non-covalently and covalently. Despite its biocompatibility, modified AuNPs have lower catalytic activity and lead to lower performance due to the hindrance of the biomolecules on the surface of the AuNPs (Wang et al. 2016). Noble metals have been emerging as a potential platform for the bioconjugation step to make an optimized condition for modified immunoassays.

Among them, the peroxidase-like activity of the nanozyme can use the substrate H_2O_2 to perform a nanozyme-catalyzed reaction (**Figure 1.2**), exemplary is gold nanoparticles (AuNPs), thereby triggering the color change of a specific substrate (Kim et al. 2021). For this nanozyme, noble metals, such as platinum-based nanoparticles in assays, have been developed for ultrasensitive detection of small molecules, ions, nucleic acids, and proteins (Loynachan et al. 2018). Several heterogenous nanozymes have been introduced, such as hollow platinum nanocage (Pt NC) using gold nanorod as the template (Long et al. 2021); core-shell Au-Ag structure (Khoris et al. 2020b; Khoris et al. 2019); heterostructure of Au-Pt (Gao et al. 2017; Panferov et al. 2021), Fe-Pt (Kim et al. 2017) or Ni-Pt (Xi et al. 2021). However, those small nanoparticles tend to agglomerate in solution, which might cause a significant decrease in their catalytic activity during catalytic operation (Huang et al. 2019).

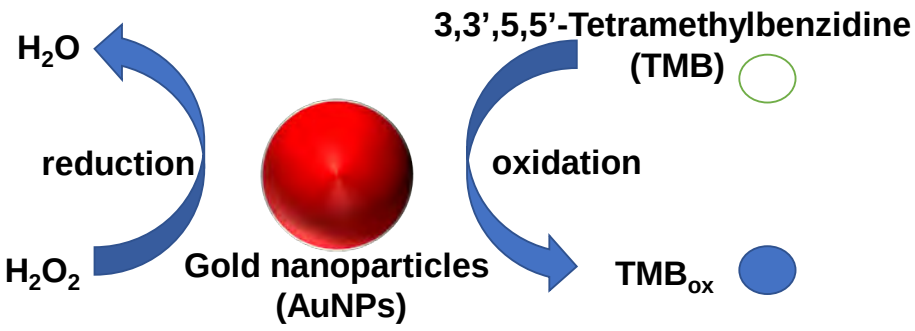

Figure 1.2 Peroxidase-like activity of nanomaterials

1.5. Signal Amplification approach for Advanced Immunoassay

1.5.1 Nanocarrier

Recently, nanozyme has been investigated in a great detail and implemented in several fields. Several optical (Ganganboina et al. 2018) and electronic analytical method (Chowdhury et al. 2018) are used for bio-medical application. Nanozyme has been utilized to substitute natural enzyme in visual detection. However, nanozymes has challenging activity and poor specificity in term of substrates' selection of the catalytic activity and are still lower than the sophistication level of the enzyme (Zhou et al. 2017). Taking it to further mileage to the immunoassay of low detection limit, an individual nanozyme bound to the target analytes was found to be not sufficient to generate high positive signal to achieve highly sensitive detection and its practical need. In establishing the immunoassay, the current modulation is being promoting the presence of the nanozymes' availability in the individual immunocomplex formation binding. In the previous studies, for such approach, immunosorbent-based vesicle was utilized to extravagate the signal of the nanozymes (Ganganboina et al. 2020b; Ye et al. 2017) or in situ seed growth of the nanozyme (Khoris et al. 2020a; Khoris et al. 2019; Wang et al. 2016), which showed escalating detection signal up to a certain degree of amplification but the drawback on its simplicity needs to be reconsidered

Recently, A shift of the approaches to establish biosensing platform immigrates from enzyme-dependent to signal-dependent, pivoting on the amount of the signal molecules present correlating to the successful biorecognition-target conjugation. Miao *et al.* (Miao et al. 2018) and Ren *et al.* (Ren et al. 2018) reported nano-cargo based on MoS_2 nanosheet interaction to hydrophobic substrate curcumin and encapsulation of chromogenic dye and metal-organic framework (MOF)-polydopamine via phi-electron interaction, respectively. By utilizing only these interactions, the hydrophobic and non-covalent interaction have higher probability to loosen out, motivating a premature release of the signal molecules from the corresponding

nanomaterials. In the other developed biosensing, liposomal nanovesicles are being used to carry signal substrates through their bi-phase structure, hydrophic region within the lipid bilayer and hydrophilic within the inner side of the vesicles during the hydration of the lipid bilayer (Ganganboina et al. 2020b; Sercombe et al. 2015). However, the intense ratio optimization and biochemical instability of the lipid bilayer hampered its practical use in which the nanovesicle tends to lose its integrity during the storage and operation by chemical and physical environmental aspects (Lin et al. 2018; Ren et al. 2018). **Figure 1.3** showed a schematic illustration of polymeric encapsulation and formed vesicle nanostructure which is used to entrap or contain drug molecules or proteins, and enveloped by a typical polymer-made membranes. Several candidates of polymer can be used to form vesicles, one of such is poly(lactide-co-glycolide) (PLGA). This polymer is commonly used as nanoencapsulation of therapeutic drug in drug delivery and has good synthetic malleability and biocompatibility. PLGA has high functional moiety such that it has rich-carboxylic end sides and it can be easily conjugated into biomolecules, such as receptor, antibody and other biorecognition molecules. The conjugation would provide selectivity properties to the vesicle and enable the utilization of the nanovesicle for biosensor application (Nagaich 2018; Zhang and Miller 2019)..

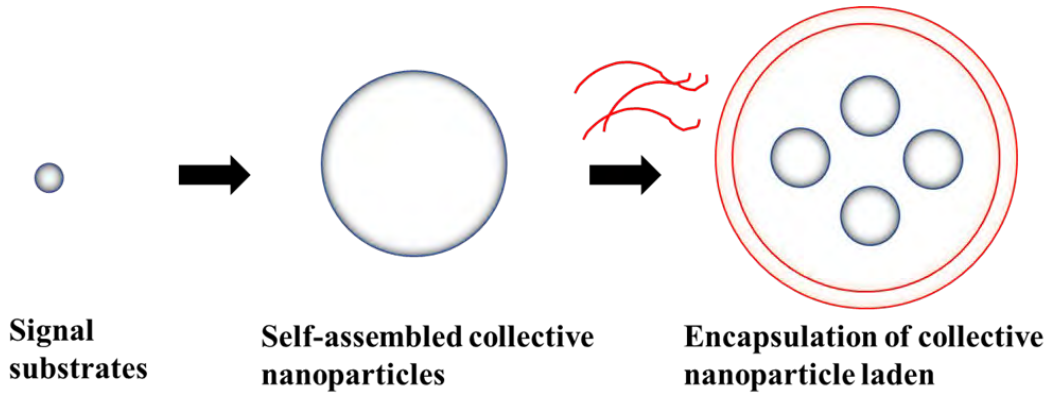

Figure 1.3 Signal enrichment in the nanocarrier

1.5.2 Signal substrate-dependent immunoassay

An immunoassay (Oh et al. 2018; Takemura et al. 2017; Wang et al. 2018a) and DNA/RNA-based assay are used to determine the presence of viral agents in the target samples (Bhardwaj et al. 2019; Duchamp et al. 2010; Yao et al. 2020). Nucleic acid-based detection could detect lower amount of target analytes but slammed with higher operation cost and complex operational steps (Arima et al. 2020; Laconi et al. 2020). On the other hand, immunoassay has basically simpler protocol but suffers from false-negative results due to low magnitude of analytical signal (Khoris et al. 2019; Xu et al. 2017). In addition, the available platform in the society has only utilized single-targeting signal because of existing methodlogy (Wang et al. 2019). Recently, Zhu et al. demonstrated a microfluidic electrochemical sensor with multiple enzymes to monitor the biomarkers in leukemia tumors (Zhu et al. 2020a). Based on the metabolite changes, the biosensor indicated and determined the changes as detection signal via interaction of multiple enzymatic reaction. However, usage of enzyme is again discomforted from its instability to physical condition and affects the biosensors' performance. Instead of using group of enzymes or other biological components in chromogenic mechanism, the compilation of chromogenic dyes should be responsive to a single trigger. Each chromogen could responsible to each target, such as pH indicator dye which will exhibit color change in the same range of acidity (Li et al. 2019). The chromogen-dependent biosensor can transit an existing immunoassay to the multiplex immunoassay. Illustration of **Figure 1.4** showcased the association of the multiple responses in a single readout could give more valuable details on the viruses in the sample, proposing an identification feature in a single detection.

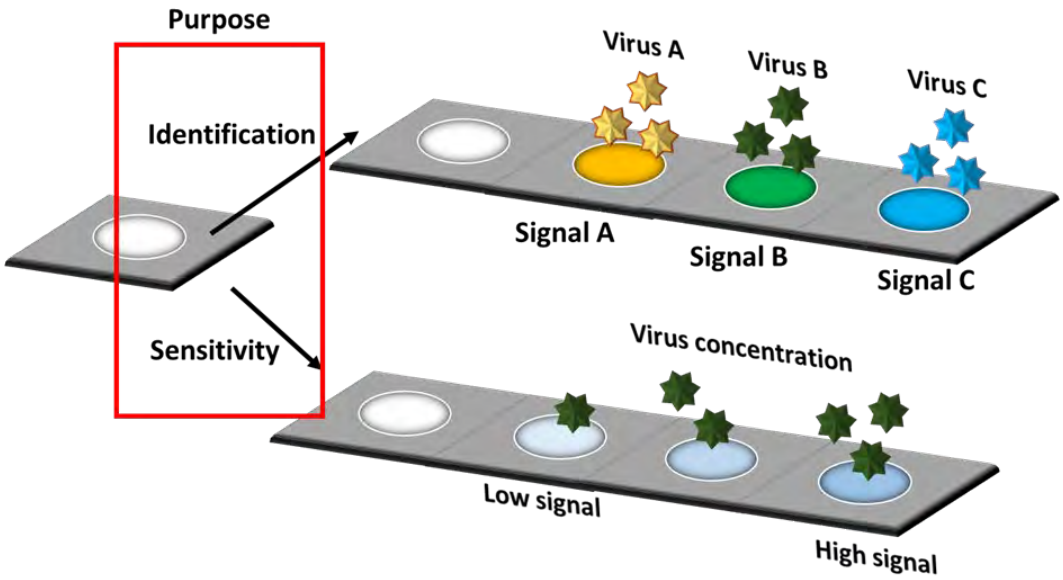

Figure 1.4 Signal-dependent immunoassay for identification property

Nanocarrier has shown integration of substrate encapsulation and signal enrichment. The abundant chromogen should be introduced in the biosensor to integrate the multiple responses and high signal generation. Considering several published nanocarrier-based immunoassay, Yan et al. (Yan et al. 2019) demonstrated dye-encapsulated ZIF-8 for colorimetric biosensing. However, the ZIF nanocarrier has a slight drawback due to the leakage of free signal molecules from the nanocarrier due to the loosened binding (Sun et al. 2020). And the reaction time in the sensing is considered slow because of the slow molecules-releasing mechanism. Other strategies in nanocarrier-based immunoassay require a two-step signal amplification by releasing from nanovesicle as the nanozyme's carrier (Ganganboina et al. 2020c; Ye et al. 2017).

In the progression of self-assembly method in nanomaterial preparation, the technique using nanoprecipitation underlines the effect of solvent in term of solubility to the degree of co-nanoprecipitation (Liu et al. 2020). Recent published work successfully synthesized a crystalized nanoparticles through precipitation of organic dye stabilized by protein (Xu et al.

2020b). The nanoprecipitation composed of antibodies and organic dye all-in-one precipitation, causing random antibody orientation which led to lower immunoassay efficiency. Also, encapsulation efficiency of the organic dye within the protein co-nanoprecipitation is estimated to be as low as less than 10% because of low amount of protein's hydrophobic pocket (Shen et al. 2017). In another study, a high loading of the fluorophore was demonstrated in polymeric encapsulation forming fluorescent vesicles based on anti-solvent precipitation (Wu et al. 2020). This finding showcased an interesting point about co-precipitation engineering to load higher amount of organic molecules within the polymeric membrane by adjusting the solubility and solvent use in the mixture of substrate and the polymer (Bilati et al. 2005; Venkataramanan 2016). Hence, solvent selection and its mixture are essential in sequential nanoprecipitation, which prevails the new chapter to high-loading nanocarrier. Overall the adopted strategies in advancing virus detection in this dissertation is summarized in **Fig.1.5.**

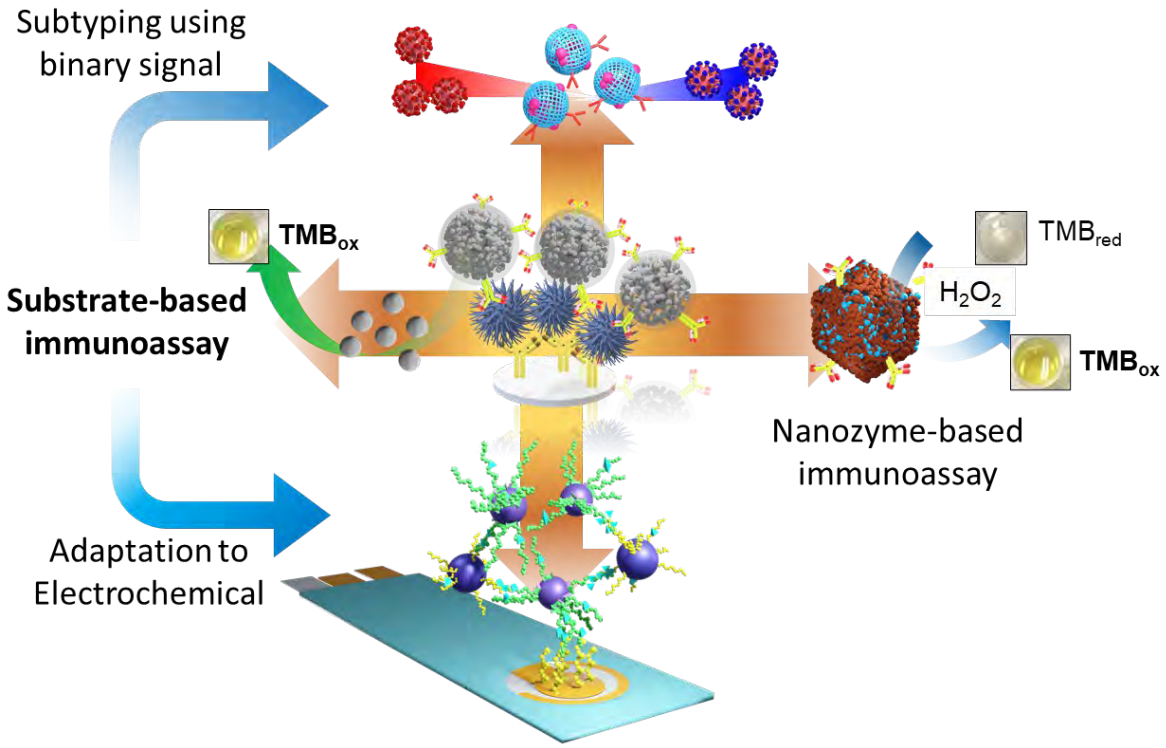

Figure 1.5 Overview of the signal enrichment-based virus detection

Chapter 2

Nanomaterial Synthesis

Chapter 2. Nanomaterial Synthesis

2.1 Introduction

In this section, the main purposes were to elaborate on the preparation of the nanomaterials used in the development of the immunoassay. The nanomaterials were categorized as substrate encapsulating-properties-based nanomaterials (nanocarrier) and catalytic-exhibiting nanomaterials (nanozyme). Two types of nanocarrier were prepared based on the PLGA encapsulation and chromogens substrates nanoprecipitation, including peroxidase substrates, 3,3',5,5'-tetramethylbenzidine (TMB), and pH-sensitive dye, phenolphthalein (PP) and thymolphthalein (TP). The detailed protocolar and parameters of the preparation of the nanomaterials were reported in this following chapter.

2.2 Materials and Instruments

2.2.1 Materials

$CuSO_4 \cdot 5H_2O$, ethyl acetate, Dimethyl sulfoxide (DMSO), polyvinyl alcohol n=1500~1800, and TMB was purchased from Dojindo (Osaka, Japan). Hexachloroplatinum (IV) acid hexahydrate (H_2PtCl_6), Cobalt (II) nitrate hexahydrate, Hydrogen peroxide (H_2O_2), phenolphthalein (PP), thymolphthalein (TP), bovine serum album (BSA), dimethylformamide (DMF), and dialysis cellulose membrane were purchased from Wako Pure Chem Inc. (Osaka, Japan). 3-Mercaptopropionic acid, 2-Methyl imidazole, 3,3',4,4'-tetramethylbenzidine (TMB), N-(3-dimethylaminopropyl)-N'-ethylcarbodiimide hydrochloride (EDC), Ethanol (99%), amicon ultracentrifugation tube, poly(D,L-lactide-co-glycolide) acid terminated (PLGA), N-hydroxysuccinimide (NHS), N-(3-dimethylaminopropyl)-N'-ethylcarbodiimide hydrochloride (EDC) were obtained from Sigma-Aldrich Co. (St Louis, MO, USA). Nunc MaxiSorp Flat-Bottom Plate was purchased from Thermo Fisher Scientific (MA, USA).

2.2.2 Instrument

Scanning electron microscopy (SEM) images were obtained using a scanning electron microscope (SEM, JSM-6510LV, JEOL, Japan). Transmission electron microscopy (TEM, JEM-2100F, JEOL, Ltd., Japan), Powder X-ray diffraction (PXRD, RINT ULTIMA XRD, Rigaku Co., Japan), and UV–Vis absorption spectra measurements (UV-1800, Shimadzu, Kyoto, Japan) are performed

2.3 Nanomaterial Preparation

2.3.1 Synthesis of Nanocarrier

2.3.1.1 Preparation of TMB-NPs and TMB-NPs-encapsulated PLGA

Based on the nano-co-precipitation process for the carrier-free nanodrug in drug delivery systems, small hydrophobic molecules, such as TMB, can assemble into nanoparticles (NPs) because of the sudden change in the solvent environment. TMB-NPs were prepared following previously reported method with minor modification.(Jiao et al. 2019; Xu et al. 2020b) TMB was dissolved in of DMSO (10 mg/mL) and added into 30 mL of BSA (1 mg/mL, w/v) in PBS (pH 6.5) containing 137 mM sodium chloride, 2.7 mM potassium chloride, 8 mM sodium hydrogen phosphate and 2 mM potassium dihydrogen phosphate. The mixture was continuously stirred for 12 h at 4 °C, stabilizing the dispersed TMB-NPs formation. Then, the turbid solution was centrifuged and washed three times with PBS, followed by freeze-drying for further usage.

TMB-NPs redispersed in DI water were encapsulated in PLGA nanovesicles using the previously reported method with minor modifications (Kocbek et al. 2007; Zhang et al. 2019). Four hundred microliter of the aqueous solution of TMB-NPs was added to 2 mL of ethyl

acetate, and 100 mg PLGA and the mixture was gently stirred with alternating sonication. After two minutes of emulsifying, the PLGA/TMB-NPs, 8 mL of polyvinyl alcohol (5%, w/w, aqueous) was added to the w/o emulsion to form a w/o/w double emulsion and stirred further for 5 min. The organic solvent was extracted by stirring the double emulsion with 200 mL of an aqueous solution of polyvinyl alcohol 0.1% (w/w) for 5 min to solidify the nanoparticles. The resulting dispersion of nanoparticles was centrifuged at 15,000 g for 15 min and freeze-dried for further use.

2.3.1.2 Preparation of Phenolphthalein-encapsulated PLGA (PP@PLGA) and Thymolphthalein-encapsulated PLGA (TP@PLGA)

PP@PLGA were prepared using the sequential nanoprecipitation method. Four milligrams PP and 10 mg PLGA were added into a tri-solvent mixture of DMF: DMSO: Ethanol (4: 4: 2 v/v). Then, phosphate buffer saline (PBS, pH 7.2) acted as an anti-solvent and was added to the mixture, and the PP and PLGA were co-precipitated, forming PP@PLGA. The nanocarrier was further diluted to lower the organic solvent percentage and centrifuged using an Amicon filter of 30 kDa cutoff (Millipore, Germany) to remove excess chromogens from the solution and followed with slow centrifugation to remove large aggregates. To synthesize TP@PLGA, TP was used instead of PP using a similar method.

2.3.2 Synthesis of Nanozyme

2.3.2.1 Preparation of copper nanoflower (CuNFs)

Inspired by the protein inorganic hybrid nanoflowers, CuNFs were prepared by a one-pot bio-mineralization process with some modifications (Tang et al. 2019; Wei et al. 2016). Typically, 100 μL of BSA (5 mg/mL) was dissolved into 10 mL of 1 × PBS (pH 7.4) for incubation of 0.5 h under slow stirring. Then, 400 μL of $CuSO_4 \cdot 5H_2O$ solution (120 mM) and

50 µL of 10% KCl solution were added to the BSA solution and further incubated for an additional 48 h. The obtained solution was centrifuged (6500 g, 15 min) at 7 °C and washed three times. Thus, obtained CuNFs were freeze-dried and stored at − 20 °C for further usage.

2.3.2.2 Preparation of PtNPs@Co_3O_4 nanocages (Pt@Co_3O_4 NC)

PtNPs@Co_3O_4 nanocages (NCs) were synthesized involving a one-pot embodiment of Pt NPs within the ZIF-67 by slightly modifying our previously reported work (Ganganboina et al., 2020b). PVP-capped PtNPs were synthesized by reducing Pt ions by PVP in the presence of heat following a reported protocol. In general, 20 µl of hydrogen hexachloroplatinate (H_2PtCl_6) was dissolved in 4 ml of pure water to prepare an aqueous H_2PtCl_6 solution. The entire aqueous solution was added to 36 mL of methanol and 106.6 mg of PVP with a molecular weight of 29 kD and mixed. The solution was then stirred at 75°C for 3 h, washed with acetone, and redispersed in methanol.

Then, a solution of 2-methyl imidazole (0.993 g) and 8 mL of platinum nanoparticles (PtNPs) was mixed with 7 mL of methanol for 2 h at room temperature. The solution was mixed in 0.431 g of cobalt nitrate hexahydrate ($Co(NO_3)_2$-$6H_2O$) in 10 mL of methanol and stirred for another 2 h. The precipitate was redispersed in 2-Methyl imidazole solution and mixed for 1 h at room temperature. Then, centrifugation was performed, and the precipitate was mixed with $Co(NO_3)_2$-$6H_2O$ solution for 1 h. The two solutions were then stirred vigorously for 5 mins at room temperature, and the mixture was then allowed to stand for 20 h at 30°C for reaction. The precipitate was forming the embodiment of Pt in ZIF-67 (Pt@ZIF-67). Then, the resulting Pt@ZIF-67 was washed with ethanol and methanol, collected by centrifugation, and dried, obtaining the Pt@ZIF-67.

Furthermore, the obtained Pt@ZIF-67 was powdered, loaded onto a combustion board, and placed in a tube furnace. The temperature in the furnace was gradually increased from

room temperature to 600 °C at a rate of 2 °C/min. After annealing at 600 °C in the air for 5 h, Pt@Co_3O_4 nanocages (Pt@Co_3O_4 NCs) were formed by decomposition and oxidation of ZIF-67. PtNPs concentration of 0, 0.25, 0.5, 1.0, 3.0 mg/mL was used for preparation of $PtNPs_x$@Co_3O_4 NCs with x as 1, 2, 3, and 4, respectively.

2.3.3 Preparation of Amine-functionalized Magnetic Nanoparticles (A-MNP)

$FeCl_3 \cdot 6H_2O$ (0.33 g) was dissolved in EG (10 mL) to form a clear solution, followed by the addition of potassium acetate (0.78 g) and 1,6-hexanediamine (2.2 g). The mixture was stirred vigorously for 30 min and transferred into a Teflon-lined autoclave. The autoclave was heated to and maintained at 180°C for 10 h. The black products were rinsed using ethanol/water.

2.3 Results and Discussion

2.3.1 Morphology Characterization of the Nanocarrier

2.3.1.1 Nanoencapsulation of TMB-NPs forming TMB-NPS@PLGA

The molecular self-assembly technique for the preparation of the nanoparticles is evolving as a promising strategy to integrate different components for synthesizing desired hybrid nanomaterials spontaneously. The synthesis of TMB-NPs encapsulated within TMB-NPs and NPs inside PLGA nanovesicles NPs@PLGA involves two steps as illustrated in **Figure 2.1a and 2.1b**: a) synthesis of TMB-b) encapsulation of synthesized TMB- preparation commences with the self-assembly of TMB molecules using BSA as a template(Jiao et al. 2019) with excellent dispersibility.

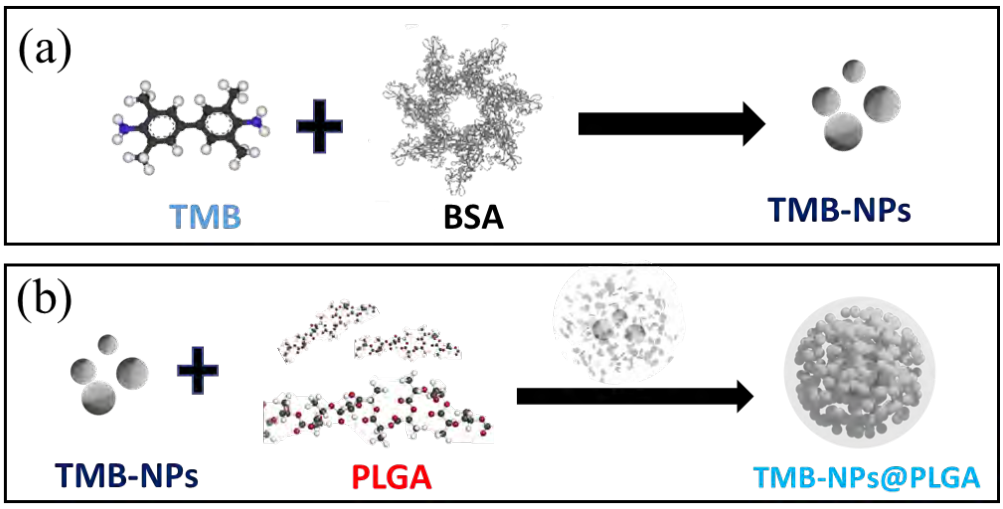

Figure 2.1 The synthesis of TMB-NPs encapsulated within TMB-NPs@PLGA; (a) TMB-NPs nanoprecipitation and (b) TMB-NPs@PLGA encapsulation

In this two-step signal enrichment in the nanovesicle, TMB underwent two-step compression, solvent co-precipitation to form TMB-NPs, and continued being encapsulated by double emulsion solvent diffusion method to form TMB-NPs@PLGA. **Figure 2.2a** showed the TEM analysis of the formed TMB-NPs. The synthesized TMB-NPs are observed to have spherical shape with size 50 nm in diameter as shown in the **Figure 2.2b** as higher magnification of the previous figure, showing the electron density of TMB within the BSA aggregation. After the encapsulation in the polymeric membrane, TMB-NPs@PLGA is analyzed using TEM as shown in **Figure 2.2c**. TMB-NPs@PLGA have presented in the form collective TMB NPs clustering together with a diameter of around 200 nm. The encapsulation of TMB-NPs in the PLGA nanovesicle is confirmed by the TEM image in **Figure 2.2d**, which clearly shows TMB-NPs are agglomerating, as the incorporation of TMB-NPs inside the PLGA nanovesicles with no sign of aggregation.

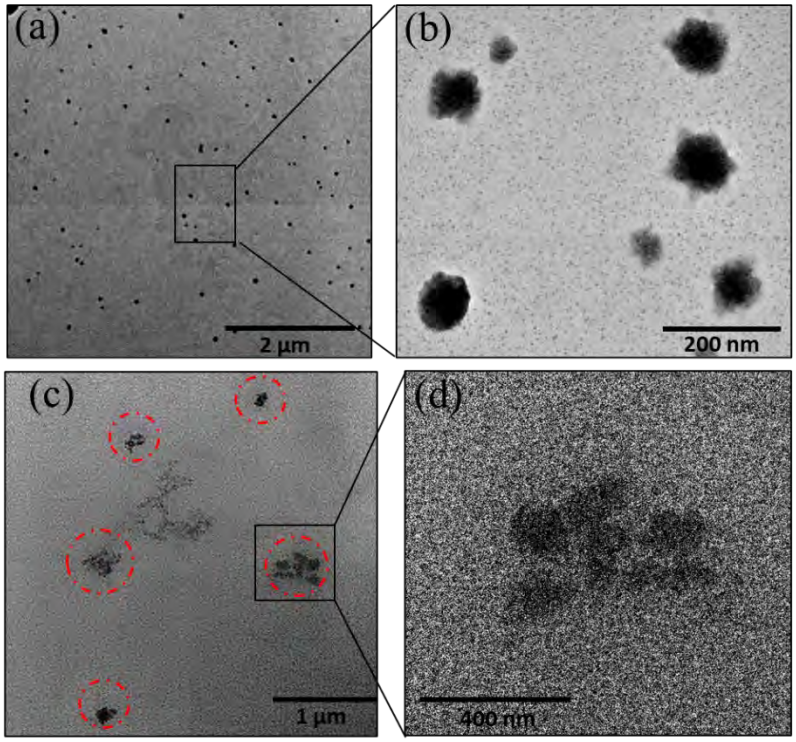

Figure 2.2 TEM analysis of TMB-NPs (a and b) and TMB-NPs@PLGA (c and d)

It is interesting that the stepwise preparation of the TMB-NPs@PLGA is distinguishable visually from the solutions' apparency. As shown in **Figure 2.3**, each derivation of the TMB-NPs@PLGA was prepared in different vials. TMB molecules were dissolved in aqueous (PBS buffer) solution and organic solvent (DMSO) resulting to light yellowish-white precipitate and clear solution, respectively. Then, TMB-NPs are visibly dispersed in aqueous solution, attributing to protein stabilizer that has good dispersibility from the surface's hydrophilicity of BSA. TMB-NPs@PLGA are also found to maintain its uniformly dispersible in PBS which the PLGA membrane is rich of free carboxyl groups from lactic acid sides on the surface of TMB-NPs@PLGA.

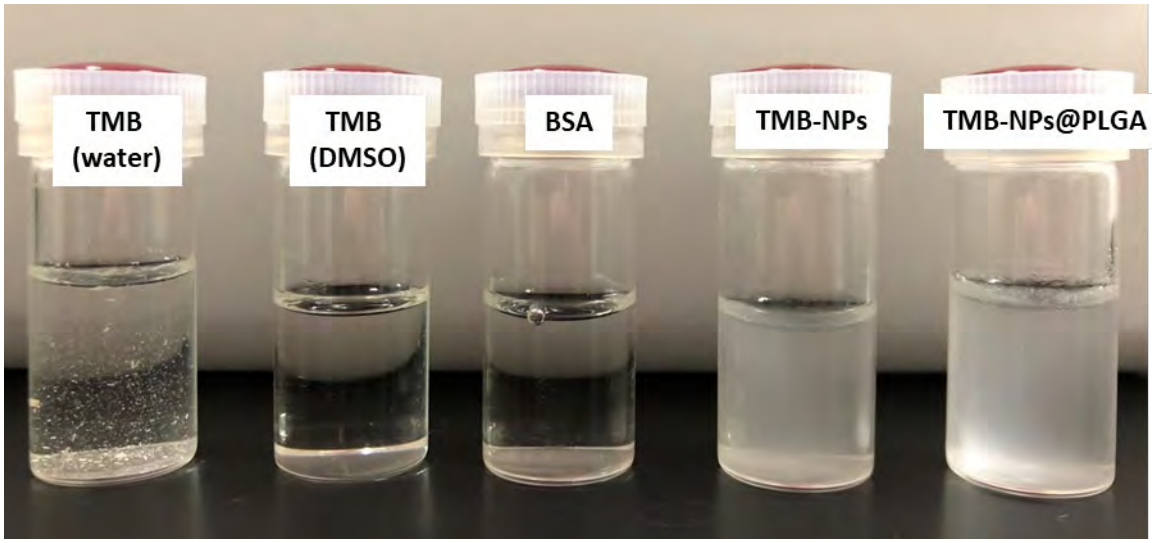

Figure 2.3 The solution visualization of TMB solution, BSA solution, TMB-NPs, and TMB-NPs@PLGA

2.3.1.2 Co-nanoprecipitation of polymer PLGA and chromogen substrate forming polymeric nanocarrier (Dye@PLGA)

The dye@PLGA preparation was conducted by taking account to the self-assembly nanoprecipitation. As illustrated in **Figure 2.4a**, the formation of the Dye@PLGA are initiated by the precipitation of the chromogen dye together with the co-presence of the polymer. In a stepwise manner, the nanoprecipitation of the chromogens, PP or TP, and poly-(lactic-co-glycolic acid) (PLGA) were investigated by varying the organic solvents of the mixture and further phosphate-buffered saline (PBS, pH 7.2) was added as anti-solvent, pushing the formation of the nanoprecipitates. The study started from one-solvent system by dissolving the chromogens and polymer in DMF. **Figure 2.4b** showed the morphology of the Dye@PLGA under scanning electron microscopy (SEM). It was visible in **Figure 2.4b-i** that the Dye@PLGA formed in DMF has various sizes and shapes coming from the observable aggregation (**Figure 2.4b-ii**), moderate nanoparticles (**Figure 2.4b-iii**) and smaller size of nanoprecipitation (**Figure 2.4b-iv**).

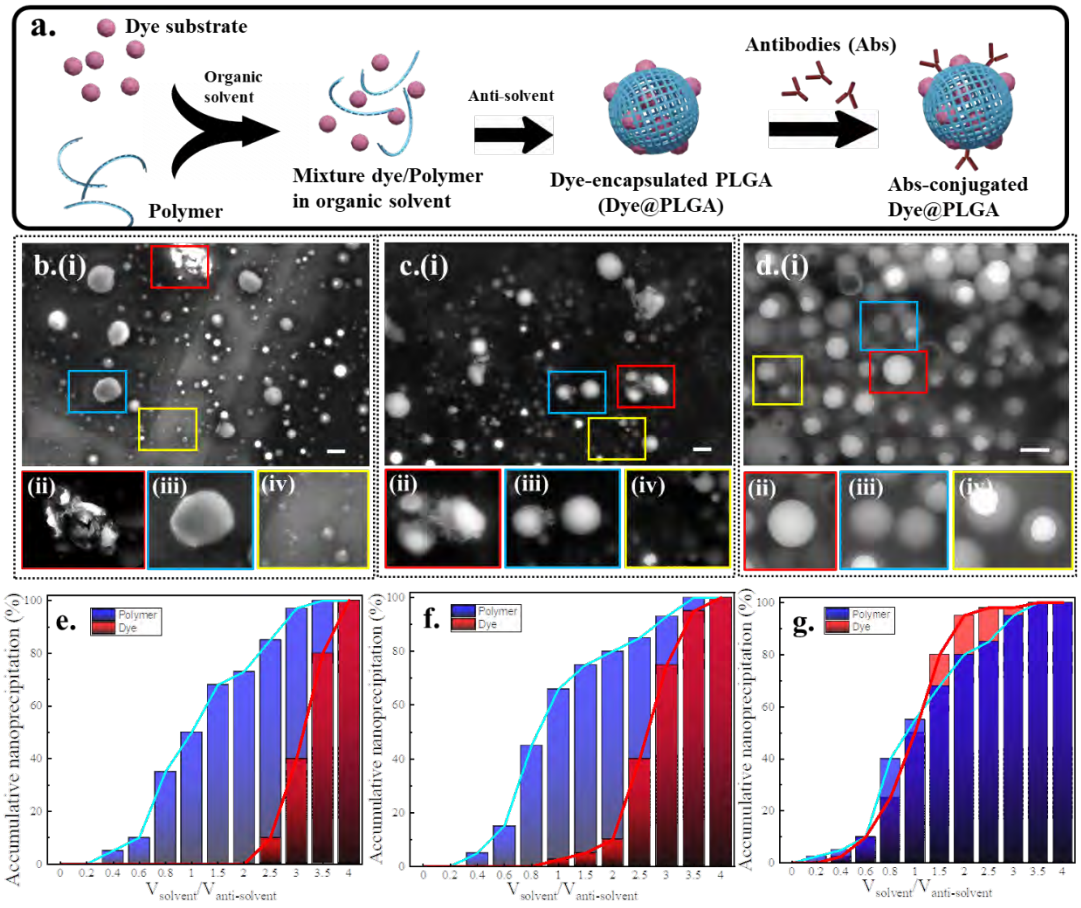

Figure 2.4 The morphology of the Dye@PLGA prepared using nanoprecipitation in a solvent mixture system. (a) The schematic illustration of Dye@PLGA preparation for immunoassay purpose. The SEM images of Dye@PLGA in one-solvent (b), two-solvent (c), and three-solvent (d) systems (scale bar: 1 µm) (ii–iv represent the magnification of the SEM image). The nanoprecipitation percentage of the polymer and the dye in one solvent (e), two-solvent (f), and three-solvent system (g).

Next, similar to previous one-solvent system, the mixture of chromogens and polymer was dissolved using co-solvent of DMF and DMSO system, which is observed to form majorly spherical-like structure (**Figure 2.4c-i**), followed with a smooth and round nanostructure **Figure 2.4c-ii)** and there are also observed several dye aggregates attached on the surface of the Dye@PLGA (**Figure 2.4c-iii**). Moreover, there are observed several aggregates of chromogen which are not associated to the Dye@PLGA as shown in **Figure 2.4c-iv**. Next, comparative to the previous system, three-solvent system composed of organic solvents of DMF and DMSO with addition of ethanol was used to dissolve the chromogen and polymer.As

shown in **Figure 2.4d-i**, the morphology of dye@PLGA was found to be more uniform and definite with neither random chromogen aggregates nor random precipitation on the surface of the Dye@PLGA. It determined that using DMF/DMSO/Ethanol as pre-dissolved solvent can demonstrate the desired nanoprecipitation of the Dye@PLGA.

The morphology of the Dye@PLGA which was formed in the various solvent was investigated further using the scattering intensity of dynamic light scattering (DLS) based on the correlation between the scattering light and the size of the particles (Leong et al. 2018; Shang and Gao 2014; Vysotskii et al. 2009). The attenuation and count intensity of the scattering light was correlated to the change of volumes in unit of ratiometry between the volume of the solvent and volume of the anti-solvent ($V_{solvent}/V_{anti\text{-}solvent}$). Based on **Figure 2.4e,** there is a time lag between the initiation precipitation of the chromogen and the precipitation of the polymer. The chromogen was still soluble in the low level of anti-solvent amount. However, in the meantime, PLGA has started emulsifying, stabilizing the surface tension of the mixture solvents.

The nuclei formation of the chromogen nanoprecipitation is progressively noticed when the anti-solvent is added. It specifies that the polymer precipitates ahead the chromogen. While the latter precipitation is occurring, the polymer NPs may have fully developed, producing particles and causing the chromogen to aggregate. The two-solvent system requires 50% less $V_{solvent}/V_{anti\text{-}solvent}$ than the one-solvent system for the chromogen to induce precipitation, as shown in **Figure 2.4f**. Still, both systems indicate the precipitation of polymer starting at $V_{solvent}/V_{anti\text{-}solvent}$ as low as 0.4. In other comparative system, the chromogen in partial organic solvent DMSO with DMF showed remarkable precipitation in low $V_{anti\text{-}solvent}$, and the co-precipitation can be induced letting both polymer and chromogen's particulate in the similar timeline. Instead of generating self-aggregating colloids, this causes the chromogen nanoparticles to develop on the polymeric membrane. Furthermore, the three-solvent system

includes ethanol in the DMSO and DMF combination. Because of ethanol and anti-solvents like PBS are miscible, the chromogen can precipitate quickly in low $V_{anti\text{-}solvent}$ which was indicated from the **Figure 2.4g**. It was shown that the higher the simultaneous precipitation occurring, it will lead to better forming of the Dye@PLGA. Although, in some points, the particle formation of the Dye@PLGA made bigger size of precipitates in the system. On the sideline, the amount of the chromogen is important aspect in the solubility and the shift of the precipitation phenomenon, such that we found that if the amount of chromogen in the three-solvent mixture is large enough, the aggregation of the chromogen can be deposited on the surface of the Dye@PLGA as shown in **Figure 2.5**.

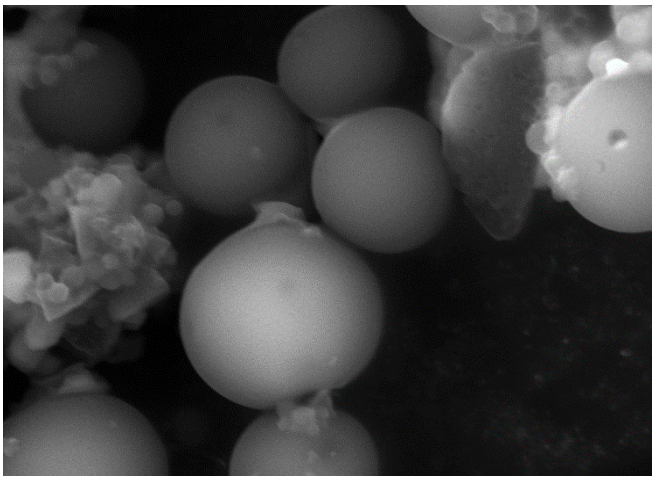

Figure 2.5 The morphology of TP@PLGA under SEM analysis

A solvent-dependent study on the behaviour of the precipitate involving self-assembly of the polymer and the chromogen is attributed to several factors: (1) the particulate of the chromogen dissolved in DMF (**Figure 2.6a**) and DMSO (**Figure 2.6b**) will evoke bigger nanoprecipitates in size (black circles) compared to chromogen dissolved in ethanol (**Figure 2.6c**). All precipitate was induced under the addition of the PBS buffer. They indicate a lower polydispersity index (PDI) (red circles in **Figure 2.6**) than in ethanol. Higher PDI (>0.3) means

bigger instability and heterogeneous nucleation in the system. In high concentrations of PP, DMF and DMSO tend to build up lower dispersity and bigger nanoprecipitation, which can also represent the chromogen aggregates. In ethanol, PP demonstrates self-limiting nanoparticles' growth, but low solubility based on the dispersity compared to DMF and DMSO. (2) DMSO has a more stable and higher energy interaction with water molecule than DMF (Venkataramanan 2016) which invokes a higher diffusion rate of a water molecule to the solvation system and precipitate the solute molecules. (3) Compared to DMSO and DMF, ethanol has higher dielectric properties with less viscosity and is more miscible to water; the high dielectric properties increase the homogenous condition in the mixture solvent to anti-solvent, and (4) ethanol reduces the surface turbulence of the solvent and anti-solvent, increasing the nanoprecipitation of the chromogen in the three solvent system (Salatin et al. 2017).

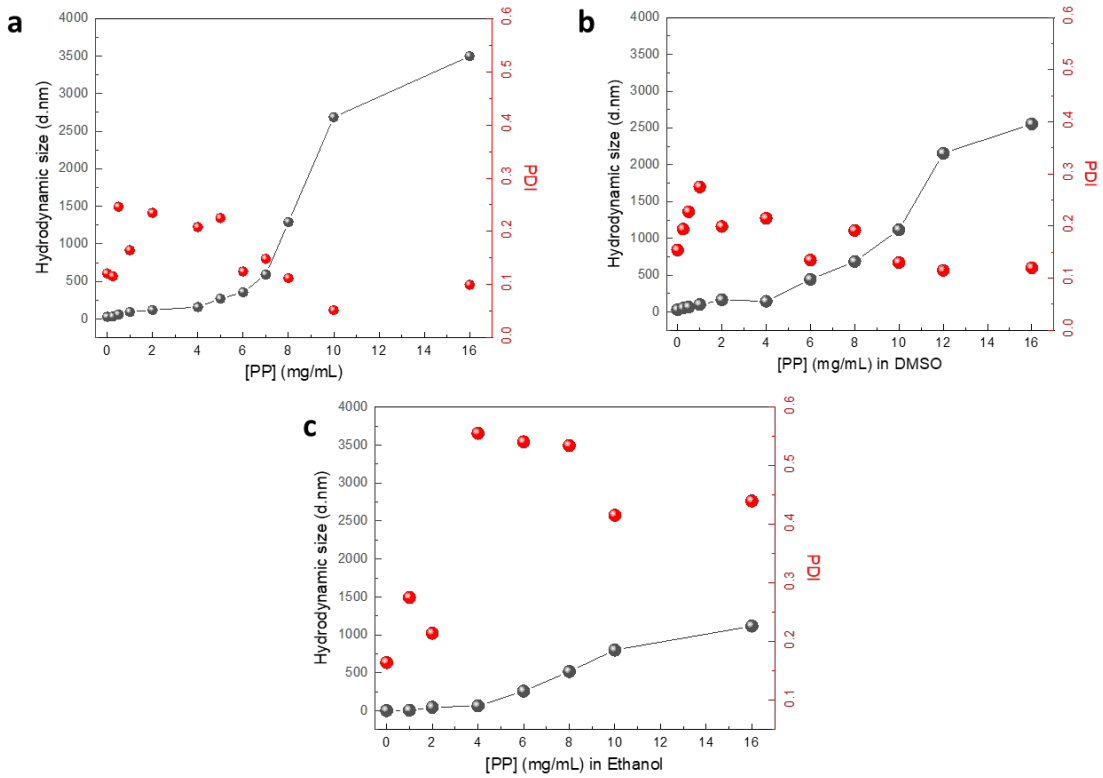

Figure 2.6 Dynamic Light Scattering (DLS) analysis of PP in various solvents

2.3.2 Morphology Characterization of the Nanozyme and Magnetic nanoparticles

2.3.2.1 Characterization of CuNFs nanozyme

Inspired by the unique features of protein-inorganic hybrid nanoflowers through self-assembly, we prepared the BSA-$Cu_3(PO_4)_2 \cdot 3H_2O$ hybrid nanoflower (CuNFs). SEM image in **Figure 2.7a** shows the flower-like structures of CuNFs with an average size of 400 – 500 nm, which have hierarchical structures with high surface-to-volume ratios. The TEM image of CuNFs is shown in **Figure 2.7b,** clearly showing the uniformly dispersed CuNFs attributing to the loaded hydrophilic BSA molecules. To confirm the structural properties of the CuNFs, an XRD analysis is further performed. The XRD patterns of CuNFs (**Figure 2.7c**) are in good agreement with the JCPDS card (00-022-0548) (Ge et al. 2012; Li et al. 2016) indicating that CuNFs crystals are mainly composed of $Cu_3(PO_4)_2 \cdot 3H_2O$ crystals.

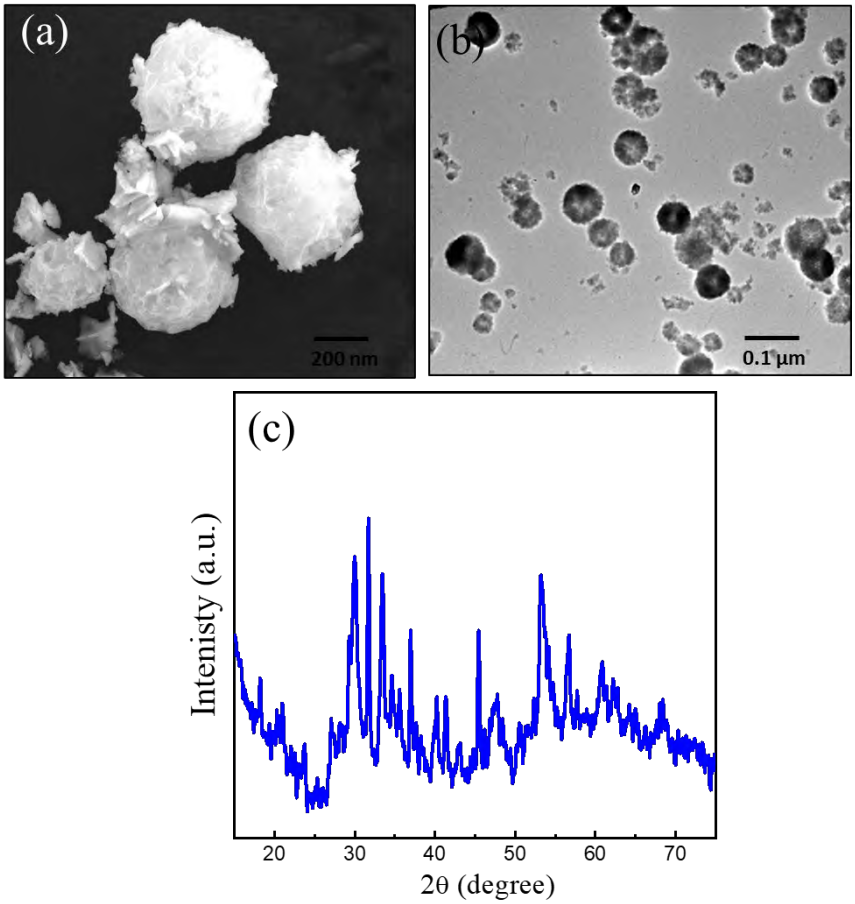

Figure 2.7 Morphology analysis of Copper Nanoflower (CuNFs) under (a) SEM analysis and (b) TEM analysis

2.3.2.1 Characterization of PtNPs@Co_3O_4 NCs

Platinum nanoparticles-embodiment cobalt oxides nanocages (PtNPs@Co_3O_4 NCs) were derived from the oxidation of the ZIF-67 with the embodiment of PtNPs within the framework. The progressive nanostructure of the PtNPs@Co_3O_4 NCs was observed under transmission and scanning electron microscopies (TEM and SEM) to analyze the morphology, topology, and elemental distribution. ZIF-67 was assembled from co-precipitation of cobalt ions and imidazole precursors simultaneously with PtNPs, forming the PtNPs@ZIF-67 nanostructure. The surface of PtNPs@ZIF-67 is shown in **Figure 2.8a-i** from SEM analysis. PtNPs@ZIF-67 was clearly observed as an icosahedron structure. The same shape was also observed in ZIF-67 without PtNPs (**Figure 2.8b-i**). Then, as shown in **Figure 2.8a-ii**, TEM analysis showed ultrasmall 4–5 nm dark dots distributed within the icosahedron structure of ZIF-67. Compared to TEM analysis of the ZIF-67 without PtNPs, **Figure 2b-ii** indicated the same geometrical structure of the PtNP@ZIF-67 without any dark dots inside it. The comparison demonstrated the successful embodiment of the PtNPs within the ZIF-67 with no geometrical distortion. It was attributed to the successive adsorption of the PVP on the surface of the PtNPs to the cavity of the ZIF-67 through the structural coordination of the polymer and its high porous nanostructure of ZIF-67. After the oxidation of the PtNPs@ZIF-67, the surface of PtNPs@Co_3O_4 formed was not as smooth as before the oxidation under SEM analysis in **Figure 2.8c-i**. While the topology profile of the PtNPs@Co_3O_4 was different than PtNPs@ZIF-67, it was still observed that the structure was maintained as an icosahedron shape with mean sizes of 300 nm. The obtained surface morphology analysis was similar to Co_3O_4 in the absence of PtNPs, as shown in **Figure 2.8d-i**.

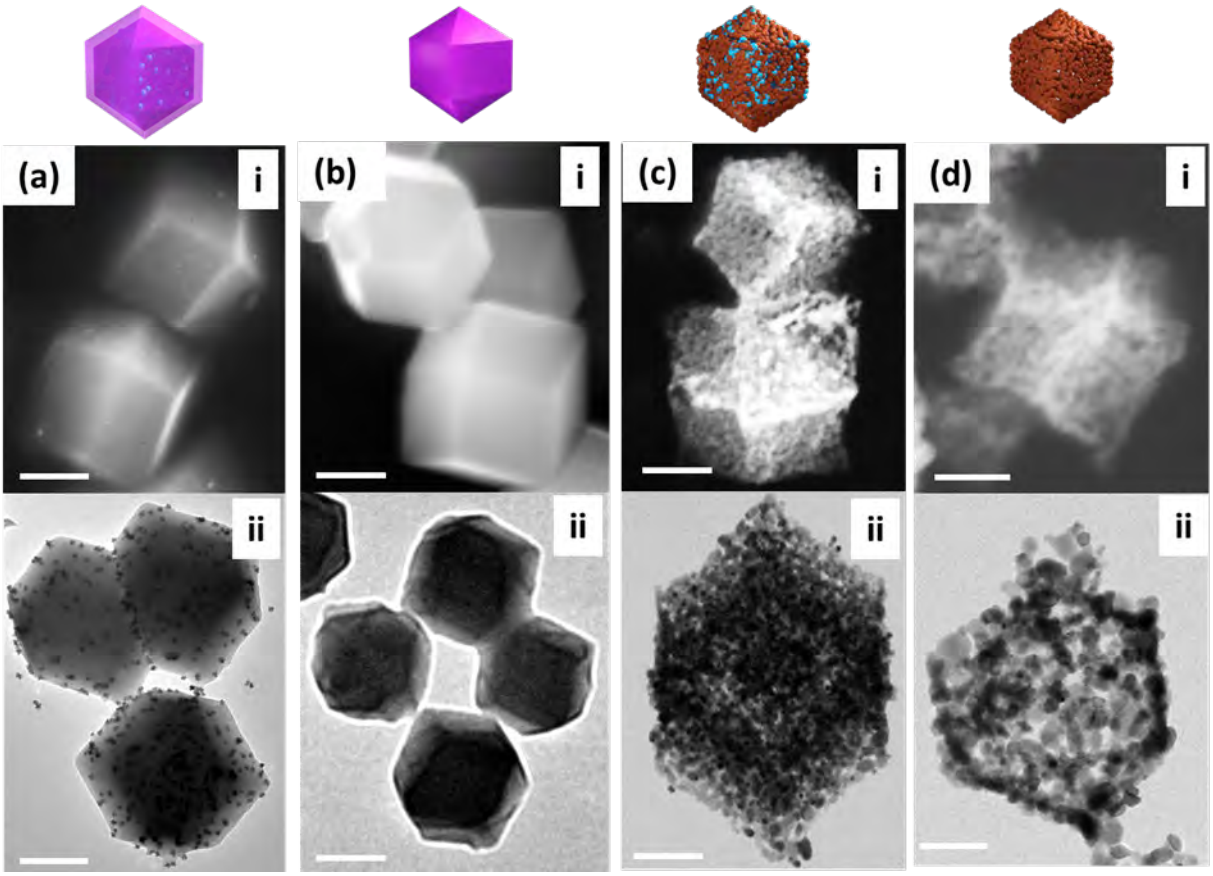

Figure 2.8 Morphological analysis of the nanomaterials by (i) scanning electron microscopy (SEM) and (ii) transmission electron microscopy (TEM) for (a) PtNPs@ZIF-67, (b) ZIF-67, (c) PtNPs@Co_3O_4 NCs and (d) Co_3O_4 NCs

Further, as shown in **Figure 2.8c-ii**, PtNPs@Co_3O_4 was observed under TEM analysis as arranged icosahedron nanostructure. As the Co framework is thermally oxidized in the air to Co_3O_4, the structure was decomposed, forming porous-like void spaces. The process is continued up to the complete conversion of the PtNPs@ZIF-67 to PtNPs@Co_3O_4 NCs. Similarly, the porous-like structure of the ZIF-67-derived Co_3O_4 in the absence of PtNPs was also observed under TEM analysis, as shown in **Figure 2.8d-ii**.

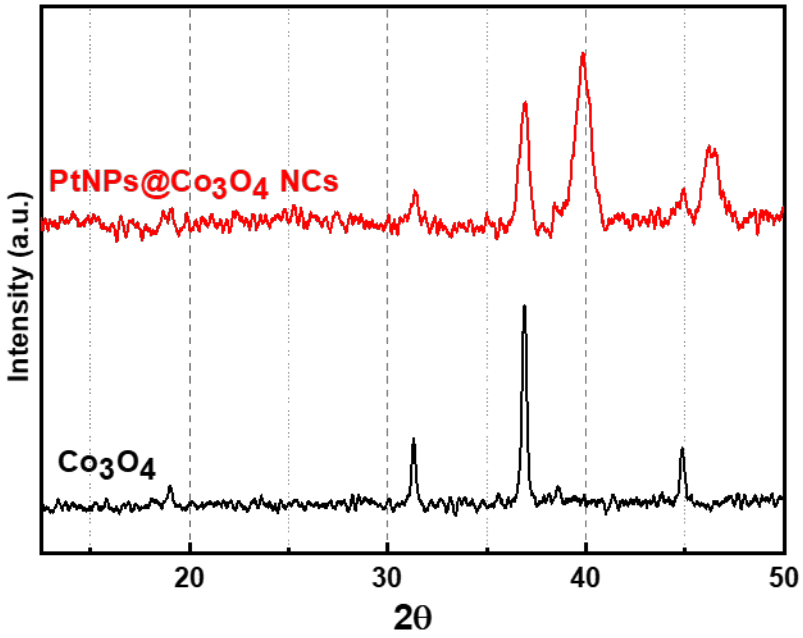

Figure 2.9 XRD analysis of PtNPs@Co_3O_4 NCs and Co_3O_4

Further, Powder X-ray diffraction (XRD) was used to check the crystalline structure of the PtNPs@Co_3O_4 NCs (**Figure 2.9**). The diffraction peaks of Co_3O_4 and PtNPs@Co_3O_4 were observed at 18.9°, 31.2°, 36.9°, and 44.9° 2θ, sourcing from the cubical crystal-structured Co_3O_4 (JCPDS 42-1467) (Yuan et al., 2011). A strong and a moderate diffraction peak at 39.7° 2θ and 46.36° 2θ can be assigned to Pt (111) and Pt (200), respectively (JCPDF No. 04-0802) (Mei et al., 2016), suggesting that PtNPs are integrated with the Co_3O_4 while maintaining the crystalline structure of the Co_3O_4. It may be attributed to sufficient space within the crystal lattice after calcination. The explicit elemental mappings of PtNPs@Co_3O_4 NCs based on the EDS analysis in TEM imaging, as shown in **Figure 2.10**. The overlapped position of oxygen (O) (**Figure 2.10a**) and cobalt (Co) (**Figure 2.10b**) in the elemental mapping indicated the structure of the Co_3O_4 nanostructure. It also showed that the Pt element (**Figure 2.10c**) was uniformly distributed within the Co_3O_4 NCs. These results account for the successful embodiment of the PtNPs and the formation of the nanocage exposing the PtNPs within the nanostructure, which is essential for its nanozyme's activity.

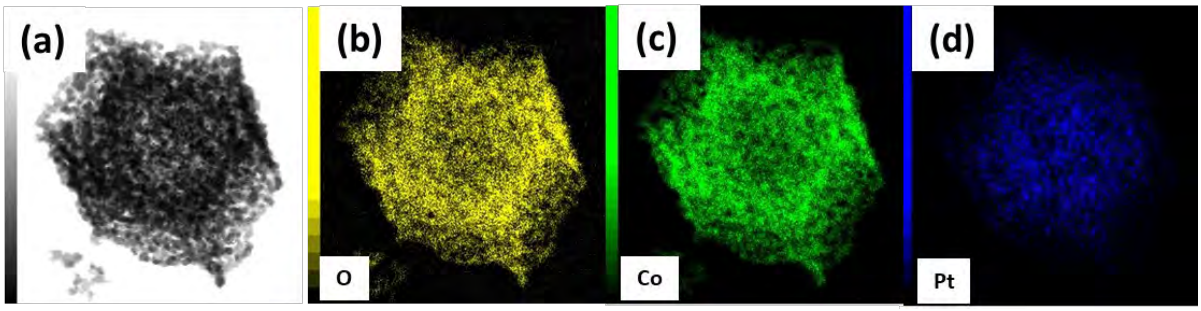

Figure 2.10 EDS analysis of PtNPs@Co_3O_4 NCs based on elemental mapping of (i) oxygen (O), (ii) cobalt (Co), and (iii) platinum (Pt) elementals

2.3.2.1 Characterization of Amine-magnetic nanoparticles

Amine-functionalized magnetic nanoparticles (A-MNPs) are used for separating the Polymeric nanocarrier bound to the influenza virus (IV/A) by a magnetic field. The magnetic separation removes excessive non-target matrix components in the detection sample and reduces the background noise (Chen et al. 2015). A-MNPs are shown to be spherical with a size around 50 nm, as shown in **Figure 2.11a**. The functional group analysis using FT-IR analysis shows the peak at 3427 cm^{-1} (**Figure 2.11b**), indicating an amine functionalization.

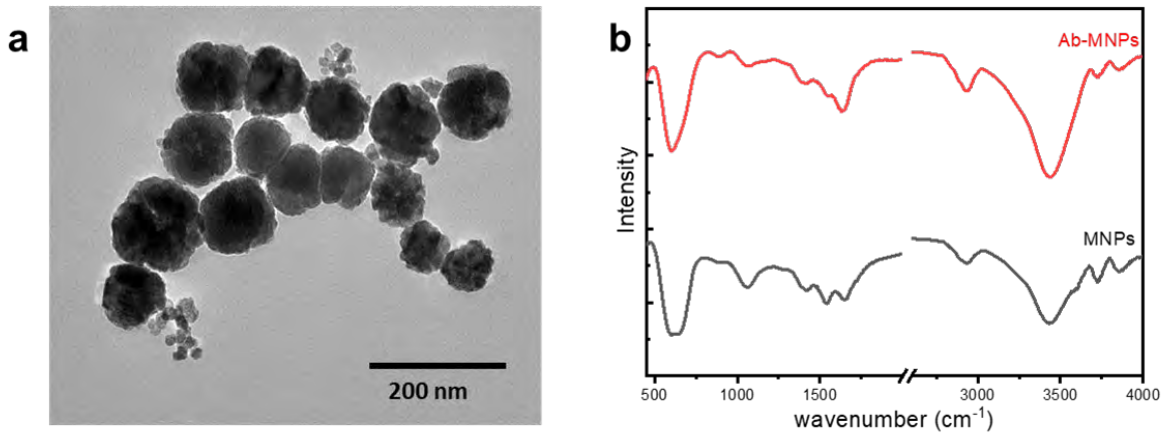

Figure 2.11 Amine-functionalized magnetic nanoparticles (A-MNPs) by (a) TEM analysis and (b) XRD analysis.

2.4 Conclusion

The main purpose of this section was to visualize and characterize the morphology of the nanomaterials. The TEM Image and Hydrodynamic size distribution analysis highlighted the formation of the polymeric nanocarrier, including the two-step method, TMB-NPs formation and its encapsulation of TMB-NPS@PLGA, and the one-step method, using co-nanoprecipitation of Dye@PLGA, showing the self-assembly approach in the preparation of the nanocarrier.

On the other side, in this chapter, we concluded the morphology of the nanozyme used in this dissertation. The nanozyme was formed via self-assembly nanoprecipitation. In the case of copper nanoflower (CuNFs), the lower solubility of copper phosphate formed the backbone of the copper nanoflower with protein bovine serum albumin (BSA) as the stabilizer and increased the solubility of the nanoflower in an aqueous solution. In the case of nanocages (NCs), platinum nanoparticles were integrated within the nanoprecipitation of the Zeolitic imidazolate framework (ZIF), a class of metal-organic framework (MOF), of cobalt ions (Co^{2+}) and 2-methylimidazole (2-MIM). The NCs were prepared by breaking down the organic framework of the formed ZIF.

Chapter 3

Catalytic Activity of Nanozymes and Releasing Mechanism of Nanocarrier

Chapter 3. Catalytic Activity of Nanozymes and Releasing Mechanism of Nanocarrier

3.1 Introduction

In this section, the main objective was to investigate the catalytic activity of the nanozymes. They were assayed based on the kinetic parameter of TMB and H_2O_2. Kinetic parameters showed the affinity of the NPs to both chemical species and the maximal velocity of the catalytic reaction. The aim is to evaluate and investigate methodologically which nanozymes could exhibit sufficient catalytic performance in the lowest concentration of the nanozyme.

Besides nanozymes' activity, in this chapter, releasing mechanism of the nanocarrier was demonstrated and investigated. Each nanocarrier was indicated with a signal change that would be utilized further in the immunoassay application. The mechanism and encapsulation efficiency were elucidated based on the experimental analysis.

3.2 Materials and Methods

3.2.1 Materials and Instruments

Tetramethylbenzidine (TMBZ) was purchased from Dojindo (Osaka, Japan). Bovine serum albumin (BSA) was purchased from Sigma-Aldrich (St. Louis, MO, USA). Hydrogen peroxide (H_2O_2), dimethyl sulfoxide (DMSO), and were purchased from Wako Pure Chem., Inc. (Osaka, Japan). 96-wells microtiter plate was purchased from Thermo Fisher Scientific (Roskilde, Denmark). All experiments were conducted using deionized (DI) water.

The time-dependent absorbance measurement was conducted using a clear transparent cuvette (l = 10 mm) in a UV-vis spectrophotometer (Shimadzu, Kyoto, Japan). The absorbance

was measured using a microplate reader for a 96-wells microtiter plate assay of the catalytic activity (Infinite 200 M Plex, TECAN).

3.2.2 Catalytic Activity Assay

Steady-state kinetic assays were performed to evaluate the kinetic parameter of the nanozyme for the Michaelis–Menten constant (K_m) and the maximal reaction velocity (v_m) by monitoring the absorbance change over time of the charge quinone complex of TMB at 655 nm (blue color). The assay was demonstrated in time-dependent absorbance from the catalytic activity of the NPs to different concentrations of H_2O_2 and TMB as substrate. The obtained absorbance value versus time plots was obtained at a fixed concentration of one substrate versus varying concentrations of the other substrate. Afterward, the linear fitting line from each Abs vs. time plot was obtained. The slope was calculated and plotted as initial velocity (v) versus the corresponding substrate concentration with the ranges of H_2O_2 and TMB were 0.1–5.0 M and 0.1–5.0 mM, respectively. The Michaelis–Menten constant was calculated based on the saturation of the velocity at the maximal catalytic reaction based on the Michaelis−Menten equation (equation 1), where v is the initial velocity, v_m is the maximal reaction velocity, [S] is the concentration of substrate. In understanding the catalytic properties of NPs, the activities were compared based on the turnover number (k_{cat}), which was calculated by equation 2.

$$v = \left(\frac{v_{max}[S]}{K_m + [S]}\right) \qquad \text{(equation 1)}$$

$$k_{cat} = \frac{v_m}{[nanozyme]} \qquad \text{(equation 2)}$$

To investigate the catalytic activity in the function of nanomaterial concentration, AuNPs and AuNPs@Ag were prepared in a two-fold series of dilutions from 760 pM to 6 pM. The fixed substrate concentration was used in this assay, with H_2O_2 and TMB were 5.7 M and

2.67 mM, respectively. The reaction was stopped after 1 min by H_2SO_4 addition. The absorbance of 450 nm/655 nm was measured using a microplate reader.

3.3 Results and Discussion

3.3.1 **Catalytic Activity Assay of Self-assembled CuNFs.**

Self-assembled copper nanoflower (CuNFs) was assayed to obtain its kinetic parameter in order to determine the catalytic activity. In the assay, two substrates, H_2O_2 and TMB, were varied in concentration while the respective co-substrate has fixed concentration to show the catalytic parameter toward the substrate with changing concentration. The Lineweaver-Burk double reciprocal plot is generated regarding the typical Michaelis-Menten kinetics. A plot of catalytic velocity and substrate concentration was shown in **Figure 3.1**. Based on double reciprocal plot, the plot indicated a linear response for H_2O_2 and TMB as shown in **Figure 3.1a** and **Figure 3.1b**, respectively, indicating the intrinsic properties of CuNFs as nanozyme. As listed in **Table 3.1**, the K_m value (mM) and maximal velocity (v_{max}) of CuNFs for both substrates are determined based on the Michelin-Menten graph (Wu et al. 2018). The K_m for both TMB and H_2O_2 are 0.07 mM and 6.5 mM, respectively. It shows CuNFs exhibit a lower K_m value than Horseradish peroxidase (HRP), indicating a higher affinity of the nanozyme to the TMB substrate. Besides, the vmax of CuNFs is 0.12 µM/s for TMB and 0.02 µM/s for H_2O_2. The CuNFs possessing high surface area and essential electrostatic interaction to the positive TMB substrate and H_2O_2 allow a considerably sufficient peroxidase-like activity fulfilling the prerequisite to developing sensitive nanozyme-based colorimetric immunoassay.

Table 3.1 The Kinetic parameter of CuNFs for TMB and H_2O_2

Catalyst	Substrate	K_m (mM)	v_{max} (μM/s)
CuNFs	TMB	0.07	0.12
CuNFs	H_2O_2	6.50	0.02
HRP	TMB	0.43	0.10
HRP	H_2O_2	3.70	0.09

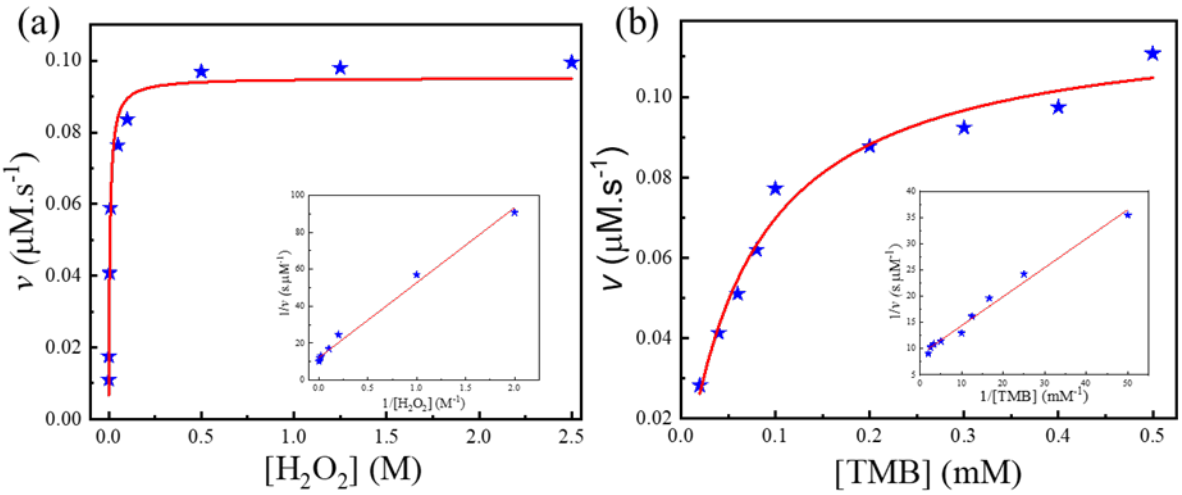

Figure 3.1 The Michelin-Menten plot of steady-state kinetic of CuNFs toward H_2O_2 and TMB, respectively (The inset showed the linearity of the LB plot

Further, the catalytic activity of CuNFs with optimum concentration at 50 μg /mL (**Figure 3.2a**) has been compared to copper (Cu) ions for the beneficial utilization in virus detection in the presence of 0.5 M H_2O_2 (**Figure 3.2b**). Based on the initial concentration of CuNFs precursor, 10 mM Cu ions are assayed against the catalytic properties of the CuNFs in the influenza virus detection.

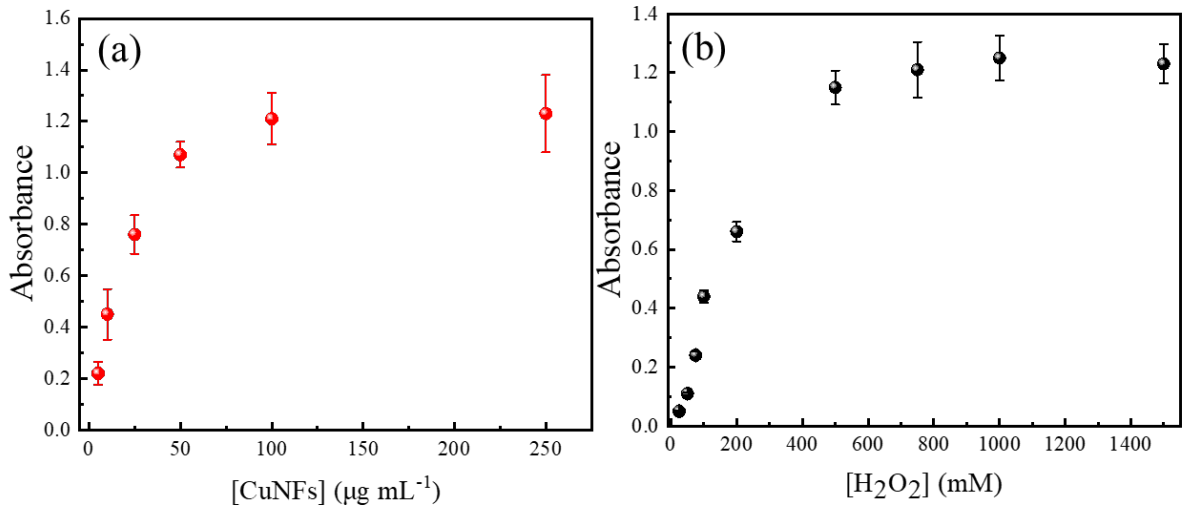

Figure 3.2 The optimization of (a) concentration of the CuNFs and (b) hydrogen peroxide in the developed TMB-NPs@PLGA-based method for virus sensing. The concentration of the Influenza virus A/H1N1 was 100 pg /mL.

Using Cu ions only, the signal is compared to catalytic CuNFs (**Figure 3.3**) in the low concentration of the influenza virus. At the nanogram level of the influenza virus, the signal by Cu ions is generated down to 50% compared to the CuNFs. The advantage of the utilization of the nanozyme implicates the crystalline structure of the copper-phosphate and its catalytic properties of the nanoflower for a better signal generation with a lower baseline signal.

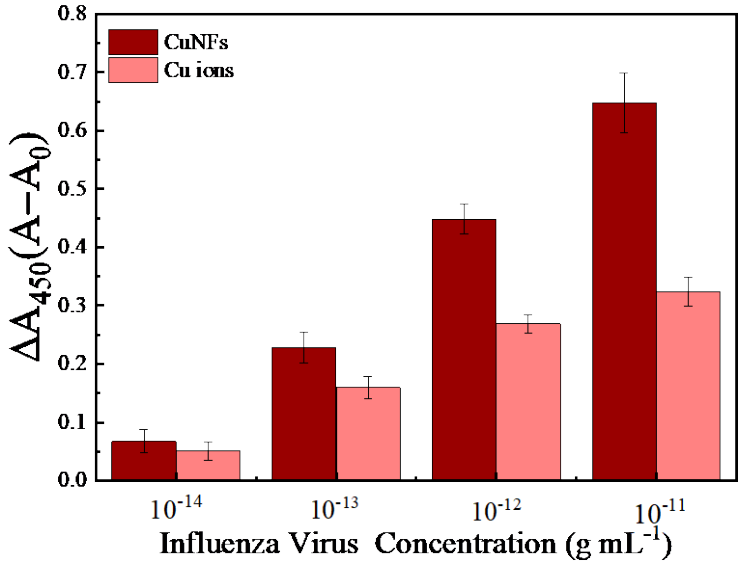

Figure 3.3 The comparative study of CuNFs and Cu ions in TMB oxidation in the immunoassay of TMB-NPs@PLGA

3.3.2 **Catalytic Activity Assay of PtNPs@Co_3O_4 NCs**

Evaluation of the peroxidase-like activity of the nanomaterials, ZIF-67, PtNPs@ZIF-67, Co_3O_4 NCs, and PtNPs@Co_3O_4 NCs was studied preliminary in a solution containing hydrogen peroxide (H_2O_2) and 3,3',5,5'-tetramethylbenzidine (TMB), a chromogen substrate. As shown in **Figure 3.4a**, all nanomaterials could exhibit high absorbance at 655 nm except ZIF-67. This result demonstrated that ZIF-67 is not a peroxidase-like nanozyme, agreeing with previously reported work ((Lu et al. 2020)). However, after oxidizing the ZIF-67, Co_3O_4 NCs demonstrated peroxidase-like activity, showing activation of non-active ZIF-67 into active Co_3O_4 nanozyme. Further, all nanomaterials were also assayed in TMB solution without H_2O_2 (**Figure 3.4b**). Only in PtNPs@ZIF-67 and PtNPs@Co_3O_4 NCs, a peak was observed at 655 nm with an absorbance value of around 0.27. Both nanomaterials could catalytically oxidize TMB without H_2O_2 as the substrate. This was probably due to the oxidase-like activity coming from the PtNPs (Cheng et al. 2020). This is clearly an interesting approach to distinguish the embodiment of PtNPs on the nano-framework.

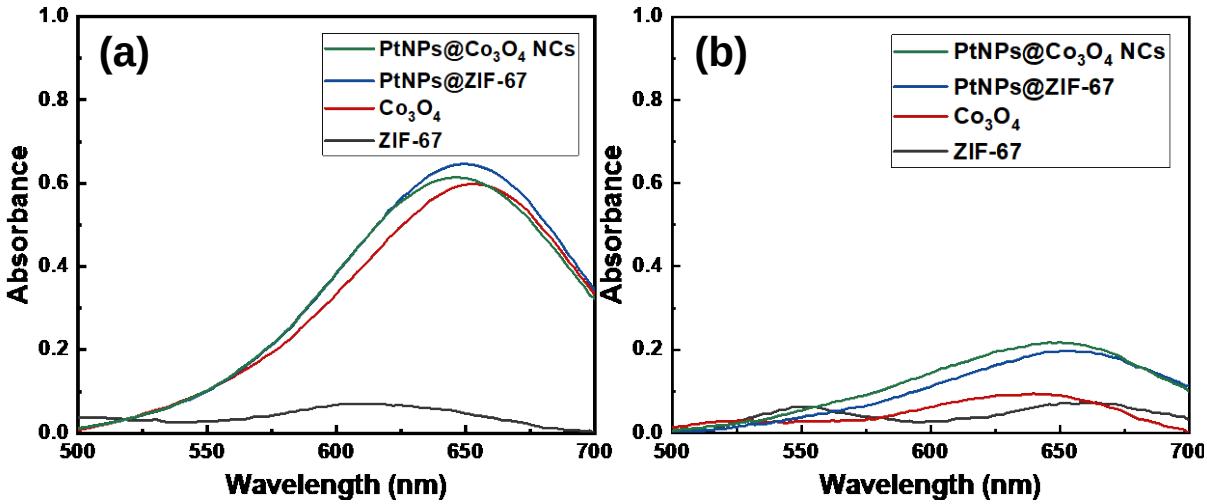

Figure 3.4 Catalytic activity of the nanomaterials with H_2O_2 (a) and without (b).

Further, the nanozymes were added to the H_2O_2/TMB solution with various concentrations of each nanozyme. As shown in **Figure 3.5a**, the catalytic oxidation of TMB by the nanomaterials was recorded at a specific time. By using the lambert-beer law, the obtained TMB (quinone complex) concentration ($\varepsilon = 3.9 \times 10^4\ mol^{-1}\ cm^{-1}$) was calculated and presented as a y-axis (Jiang et al. 2018). The catalytic oxidation of TMB can be re-interpreted as the constant velocity of the reaction at *t* time. Then, the nanozyme concentration (mg/mL) was obtained from the preparation of the nanozyme. The molar mass of each nanozyme was calculated depending on the relative weight percentage of the nanomaterial analyzed from the elemental X-ray dispersion analysis (EDS) by assuming only C, O, Pt, Co, and N contained in each nanomaterial (Yeh et al. 2020). Then, the concentration of the nanozymes (in molar) was calculated and plotted as an x-axis. The obtained plotting of the nanozymes' activity was fitted in the sigmoid curve to understand the threshold of the nanozyme concentration required to undergo the catalytic oxidation of TMB.

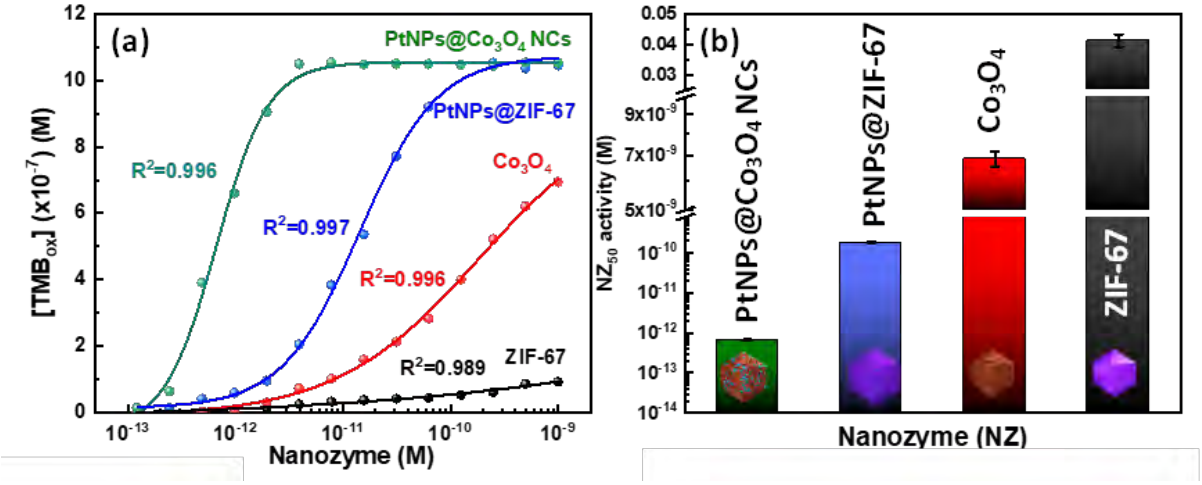

Figure 3.5 Catalytic activity of the derived ZIF-67 nanocages. (a) TMB catalytic oxidation at t=1 as a function of nanomaterial concentration; (b) nanozyme concentration required to achieve half-maximal turnover rate (NZ_{50})

From the logistic function of the sigmoid curve in **Figure 3.5a**, the lower limit and upper limit of the logistic equation indicated the minimum and maximal reaction rate of the catalytic

oxidation of TMB, respectively, related to the function of nanozyme concentration. Minimal reaction rate showed a low rate of TMB oxidation due to insufficient nanozyme concentration, as opposite, maximal reaction rate showed a saturated TMB oxidation rate because of the abundant catalytic site coming from the high concentration of nanozyme. Further, the curve's inflection point was defined as the nanozyme (NZ) concentration required to reach the half-value of the turnover rate (NZ_{50}) and was compared, as shown in **Figure 3.5b**. Higher the NZ_{50} value indicated that it needed a higher amount of nanozyme to oxidize the TMB in the presence of H_2O_2 catalytically. This means that a nanomaterial with higher NZ_{50} has lower catalytic activity than a nanomaterial with lower NZ_{50}. Inactive nanozyme ZIF-67 has an NZ_{50} of 4.13×10^{-3} M. Compared to Co_3O_4 hollow nanostructure, Co_3O_4 NCs exhibited a lower NZ_{50} to 6.85×10^{-9} M. On the other hand, PtNPs@ZIF-67 demonstrated a higher catalytic activity than the ZIF-67 with lower NZ_{50} down to 1.83×10^{-10}, showing PtNPs as an active nanozyme. Lastly, the excellent embodiment of the PtNPs and Co_3O_4 as one-body synergically downfolded the NZ_{50} about 1000 times more than the PtNPs@ZIF-67 and ten-thousands folds than Co_3O_4 hollow nanostructure with NZ_{50} down to 6.63×10^{-13} M.

Based on the stepwise study on the catalytic activity, the synergic properties and its catalytic mechanism were involved in the PtNPs@Co_3O_4 NCs, which was elucidated for several reasons. (1) PtNPs@Co_3O_4 has a porous topological structure exposing a higher number of catalytic sites and gives more accessibility of the substrates to the PtNPs within the nanocages, unlike PtNPs@ZIF-67. (2) Both PtNPs and Co_3O_4 synergically act as peroxidase-like activity nanozyme, which elevates the overall kinetic rate of the nanozyme (Cao et al. 2022). And (3) PtNPs@Co_3O_4 NCs utilize the dissolved O_2 and O_2-generated from excess H_2O_2 (Wang et al. 2021) and as a dual-nanozyme, demonstrating oxidase- and peroxidase-like activities in catalytic oxidation of TMB.

3.3.3 **Releasing Mechanism of TMB-NPs@PLGA**

TMB-NPs are successfully encapsulated inside the PLGA nanovesicles. As the subject of the utilization in immunoassay sensing, these encapsulated TMB-NPs need to be released to exhibit the detection signal required for virus detection. **Figure 3.6a** shows the schematic illustration of the release of TMB-NPs in the presence of water or DMSO. These released TMB-NPs are incubated with H_2O_2 and CuNFs. As shown in **Figure 3.6b**, there is no developed color in the absence of the H_2O_2 as the co-substrate, the CuNFs as the nanozyme, or the DMSO as the releasing agent. The blue color changes to yellow after adding the acid solution to stop the TMB oxidation reaction (**Figure 3.6c)**. The absorbance of the developed color is shown in **Figure 3.6d**, indicating a single peak in the presence of all components of the assay and the stability of TMB as signal molecules in the encapsulation and dissolving-and-releasing process.

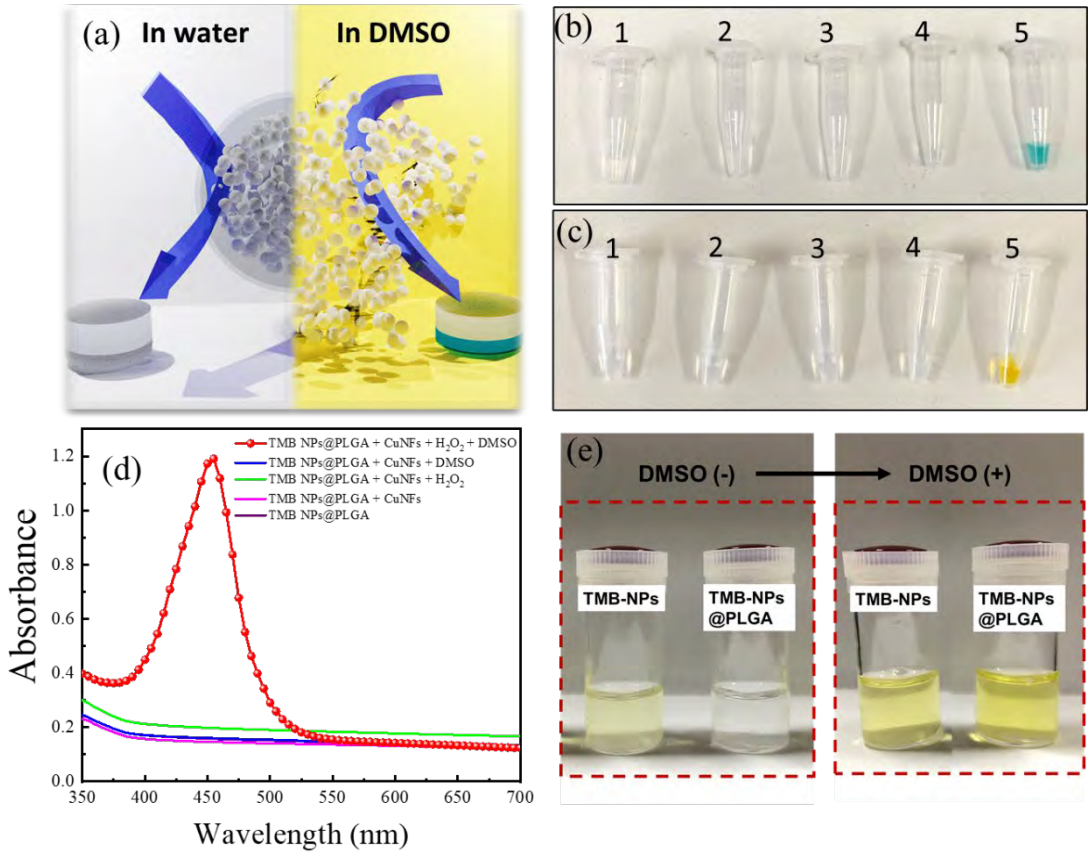

Figure 3.6 (a) The schematic illustration of the DMSO as the releasing agent of the dissolving of TMB-NPs@PLGA; (b) and (c) demonstrate the color change of TMB-NPs@PLGA in the presence of DMSO, H_2O_2, and CuNFs for before and after acid addition respectively. (1) TMB-NPs@PLGA, (2) TMB-NPs@PLGA + CuNFs, (3) TMB-NPs@PLGA + CuNFs + H_2O_2, (4) TMB-NPs@PLGA + CuNFs + DMSO, and (5) TMB-NPs@PLGA + DMSO + CuNFs + H_2O_2; (d) the corresponding absorbance spectrum of the illustration (c) of the catalytic oxidation of TMB-NPs@PLGA; (e) represents the color change of TMB-NPs and TMB-NPs@PLGA with and without DMSO.

Also, the TMB-NPs and TMB-NPs@PLGA are assayed before and after the addition of DMSO. The digital photograph illustrates the difference between TMB-NPs with and without nanoencapsulation of PLGA. It shows a well-dispersed, partially transparent solution to TMB-NPs@PLGA in the absence of DMSO (**Figure 3.6e**). Opposite to its counterpart, TMB-NPs without the PLGA nanovesicle develop a slightly yellowish color with a partially white cloudy solution in the presence of H_2O_2/CuNFs in acidic conditions. These show desirable spatial protection on the TMB-NPs by the PLGA nanovesicle, isolating the TMB-NPs from external stimuli. In the presence of DMSO, the higher catalytic oxidation of TMB is

occurred on both TMB-NPs and TMB-NPs@PLGA, pointing out the dissolving-and-release mechanism of TMB-NPs@PLGA. DMSO dissolves the nanovesicles and follows up with the dissolving of TMB-NPs, releasing the TMB molecules to the H_2O_2/CuNFs solution.

3.3.4 **The release mechanism of the Dye@PLGA**

The chromogenic encapsulation of the dye@PLGA was studied by TEM analysis. As shown in **Figure 3.7a**, PP@PLGA has spherical morphology with several small black dots within the bigger spherical structure. The size of the polymeric nanocarrier and the smaller spherical structure are estimated around 900 nm and 50–100 nm, respectively. There are no observable chromogen aggregates outside the spherical structure, indicating the successive encapsulation of the dye within the polymeric boundary. Similarly, the synthesized TP@PLGA shows a spherical shape with a size of 0.85 µm with observable few black dots within its structure (**Figure 3.7b**).

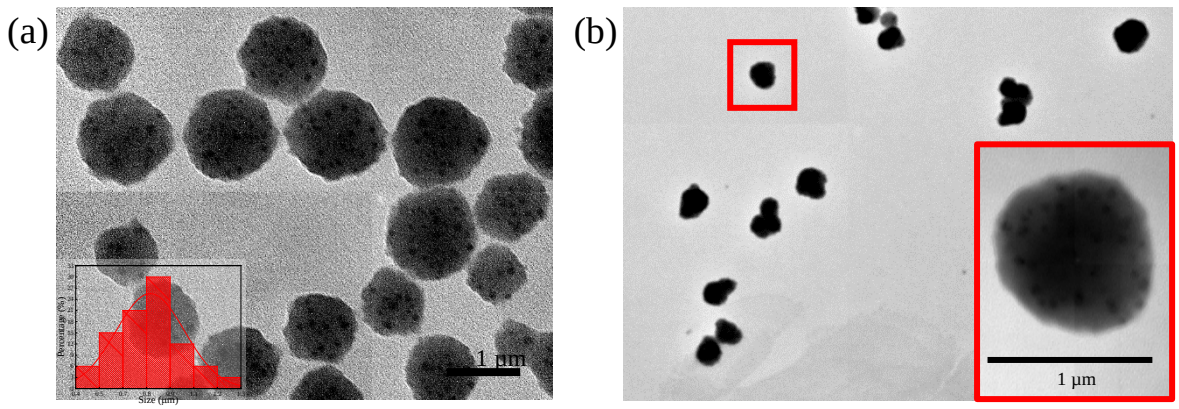

Figure 3.7 TEM Analysis of (a) PP@PLGA and (b) TP@PLGA

The chromogen loading calculation is based on the calibration curve of PP in solution (pH 10). The PP@PLGA are weighted, and the absorbance of the PP@PLGA in pH 10 solution is measured. The calibration curve of PP is obtained from the absorbance at 550 nm as the function of the PP concentration. The loading capacity of the PP@PLGA using one-solvent,

two-solvent, and three-solvent mixtures was estimated at around 29.02%, 32.44%, and 53.15%, respectively. Compared to its counterpart of one-solvent and two-solvent systems, by using three-solvent combinations, the nanoprecipitation demonstrates the Polymeric nanocarrier with higher chromogen co-precipitated inside the polymeric boundary.

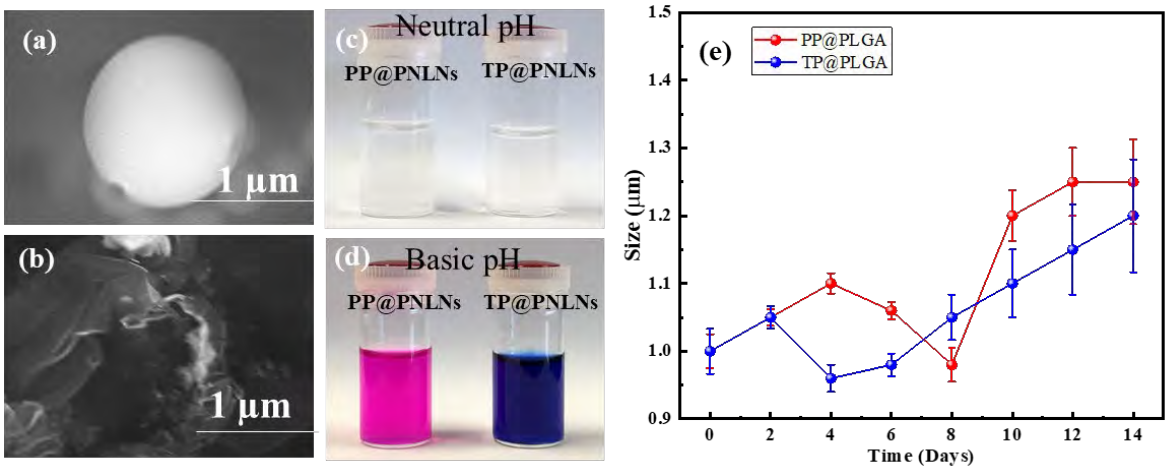

Figure 3.8 Characterization of Dye@PLGA and the release of the chromogen from the polymeric nanocarrier; The SEM image (a and b) of Dye@PLGA and its digital image of the solution color (c) in neutral pH and (d) in alkaline pH. (e) stability test of chromogen@PLGA based on the change of size.

Polymeric nanocarrier was encapsulated pH-sensitive chromogens, PP and TP, which will show color development in basic pH conditions. The Dye@PLGA is investigated in the basic pH to understand its stability. The SEM image analysis observed the polymeric nanocarrier encapsulating chromogens, PP and TP. Under the SEM, the smooth spherical structure of the polymeric nanocarrier is observed (**Figure 3.8a)**. However, as shown in **Figure 3.8b**, the structure is ruptured upon an alkaline treatment and indicates no observable spherical structure. This indicates that the polymer boundary of Dye@PLGA is broken down in the basic pH environment in which the PLGA is known to undergo alkaline hydrolysis to lactic acid and glycolic acid (Gulzar et al. 2015; Li et al. 2011a). As the polymeric boundary is removed, the chromogens are released and stimulated in the basic pH environment, developing color change.

Initially, the solution of the Dye@PLGA is colorless in neutral pH, as shown in **Figure 3.8c**. Upon the alkaline treatment, the PP-encapsulating polymeric nanocarrier (PP@PLGA) solution turns to a pinkish color, and the TP-encapsulating polymeric nanocarrier (TP@PLGA) turns to blueish color (**Figure 3.8d**). Both polymeric nanocarrier was investigated for its stability in neutral environment in storing condition as shown in **Figure 3.8e.** It showed that both has good stability up to 10 days and started to show slightly increasement (<1.5 folds) afterwards which is still considered stable (Liu et al. 2020).

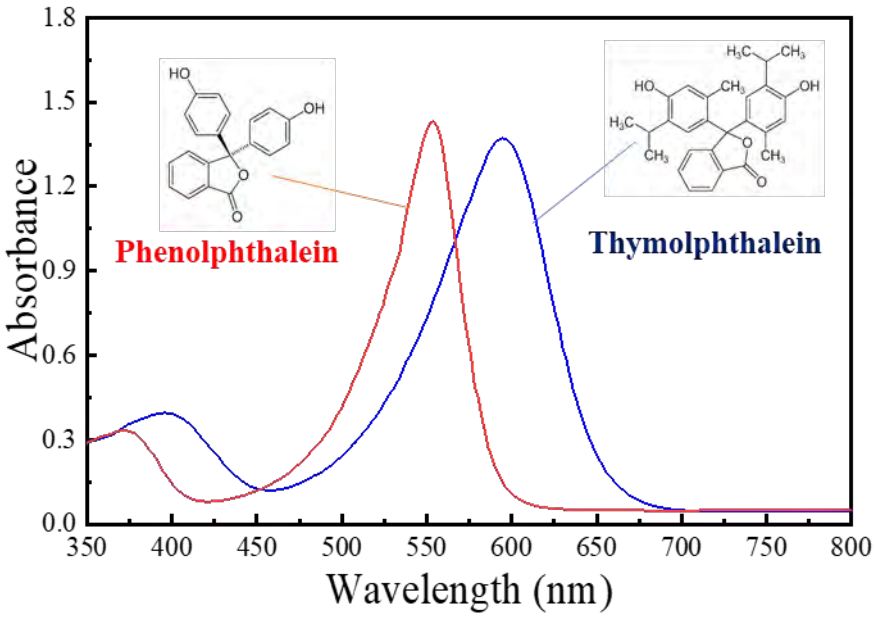

Figure 3.9 Absorbance spectra of pH-sensitive chromogen, phenolphthalein (PP), and thymolphthalein (TP) in alkaline solution

The alkaline-triggered developed color from PP@PLGA and TP@PLGA shows single peak absorbance color at 560 nm and 590 nm (**Figure 3.9**). The colorimetric signal pivots on the dual-response of the lysis of the Polymeric nanocarrier and the pH-sensitive chromogens in the alkaline environment **(Figure 3.10)**. Accordingly, the alkaline treatment on the pH-sensitive polymeric nanocarrier can break down the polymeric membrane and expose the chromogen to the basic pH condition.

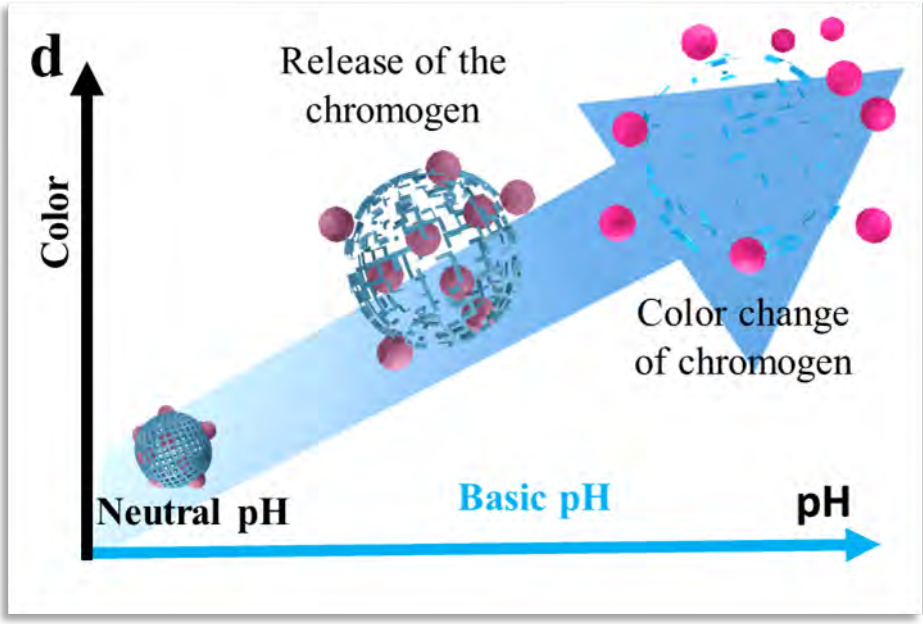

Figure 3.9 The schematic illustration of the alkaline treatment as the release mechanism of Dye@PLGA

3.4 Conclusion

The main purpose of this section was to demonstrate the enhanced catalytic activity in terms of the peroxidase-like activity of the nanozymes. As the CuNFs as nanozymes aimed to substitute the horseradish peroxidase (HRP), the affinity to peroxidase substrate, H_2O_2, and TMB was better than the natural enzyme and also more efficient compared to using only its precursor, copper ions. Other investigation regarding nanozymes related to the derivative nanostructure of ZIF-67 and Pt nanoparticles (PtNPs). It indicated that the formation of nanocages derived from ZIF-67 activated the nanostructure due to oxidation of the framework forming Co_3O_4 nanocomposite. At the same time, higher Pt contents were as expected, exiling the catalytic activity of the nanostructures, giving a superior nanozymes' activity. By this means, less minimal nanozyme is required to reach maximal catalytic activity.

This chapter also investigated and concluded the encapsulation of the signal substrates, interchangeably with dye and chromogen. PLGA polymer was used as the constituent of the polymeric boundary. Using DMSO and alkaline solution, both treatments can induce the

release mechanism of the signal substrates. Selection of the releasing mechanism depends on the need of the application and the property of the cargo, water-soluble or non-water soluble. In the case of TMB chromogen, its solubility is excellent in DMSO as solubilizing TMB from its nanoprecipitation form is essential to provide the interaction of the chromogen to the nanozyme, CuNFs.

On the other hand, pH-sensitive dye such as PP and TP is utilized as a signal transducer by change in environmental pH. This is linearly beneficial to PLGA in which it was highly hydrolyzed in extreme conditions, such as acidic and alkaline solutions. As far as our concern, acidic treatment is not practical compared to alkaline treatment as it is milder than the first.

Chapter 4

Fabrication of the Virus Detection System

Chapter 4. Fabrication of the Virus Detection System

4.1 Introduction

In this section, the main discussion was to evaluate the utilization of the proposed nanomaterials as a signal amplifier. The discussed mechanism of the signal transducer by nanozyme and nanocarrier was applied to the capture immunoassay. This chapter investigated and optimized the capture immunoassay to detect Influenza Virus (IV) and norovirus (NoV).

4.2 Materials and Methods

4.2.1 Buffer and Reagents Preparation

10 × Phosphate-buffered saline (PBS) in 1 L (pH 7.4) buffer solution was prepared in the following composition; 80 g sodium chloride, 11.5 g sodium hydrogen phosphate, 2 g potassium chloride, and 2 g potassium dihydrogen phosphate. 1 × PBS solution was prepared by 10 times dilution of 10 × PBS in water. Washing buffer was prepared by mixing 100 mL 1 × PBS solution with 0.5 mL 20% (v/v) Tween-20. Acetate buffer was prepared by adding 20.4 g sodium acetate trihydrate and 5.7 mL acetic acid, messing up to 50 mL with DI water (pH 5.2). Chromogen solution was prepared by adding 20 µL 10 mg/mL TMBZ in DMSO to 0.2 µL H_2O_2 in 1 mL acetate buffer (pH 5.2). BSA (5%) was used as a blocking agent by dissolving it in 1 × PBS.

4.2.2 Biological Sample Preparation

The various subtype influenza viruses were purchased from ProSpec-Tany Technogene, Ltd. (East Brunswick, NJ, USA). Anti-IV/A/H1, H2, H3 (Anti-HA), Anti-IV/A/H1N1, and

anti-IV/A/H3N2 antibodies were purchased from Sino Biological Inc. (Beijing, China). The Hepatitis E virus-like particles (HEV-LPs) expressed by the baculovirus expression system were provided by Dr. Tian Chen-Li from the National Institute of Infectious Disease Japan.

An anti-NoV antibody broadly reactive to genogroup II (NS14 Ab) was acquired from the spleen cells of orally immunized mice (Kitamoto et al. 2002; Kou et al. 2015). Monoclonal antibody (NS14, isotype-IgG), which is specific and broadly reactive to genogroup II of NoV, was used in this work for the sandwich-type immunoassay. NoV-LPs were expressed in the baculovirus expression system and purified following the virus-like particle preparation protocol (Ahmed et al. 2017b; Boonyakida et al. 2022). Clinically isolated NoVs were collected from fecal samples of the patients with infectious gastroenteritis, including foodborne illness, by inspections based on laws and ordinances. The fecal sample, 0.1 g, was suspended in 900 μL of phosphate-buffered saline (PBS, pH 7.4), followed by separating solids, and the supernatant was used as a detection sample. According to the guideline, this NoV sampling was carried out after approval from the Ethics Committee of Environment and Hygiene Institute in Shizuoka Prefecture (September 14, 2016). The NoV concentration of the supernatants was evaluated to be G II 4: 5.7×10^7 RNA copies/mL by RT-PCR. Recombinant dengue virus 2 NS1 protein (ab181966) was purchased from Abcam (Cambridge, UK), and 293T whole cell lysate was obtained from Genetex (CA, USA).

Recombinant 2019-nCov Spike protein (RBD) (ABL-1-113) and Anti-2019-nCov S Protein (RBD) Monoclonal Antibody (ABN9306) were purchased from Abvigen Inc. (Newark, NJ, USA). Sandwich anti-SARS-CoV-2 spike protein chimeric Ab ($Ab_{SARS\text{-}CoV\text{-}2}$ targeting S protein) was purchased from Sino Biological Inc. (Beijing, China). Sandwich anti-SARS-CoV-2 nucleocapsid protein polyclonal Ab and monoclonal Ab ($Ab_{SARS\text{-}CoV\text{-}2}$ targeting N protein) were purchased from Genetex (CA, USA).

A recombinant baculovirus expression system produced the G3 HEV-LPs described previously (Li et al. 1997; Li et al. 2011b). A series of 14 fecal specimens were collected from 4 to 43-day postinfection (dpi) from a G7 HEV-infected cynomolgus monkey. The fecal specimens were diluted with 10 mM in PBS to prepare a 10% (w/v) suspension. Then the suspension was shaken at 4°C for 1 h, clarified by centrifugation at 10,000 × *g* for 30 min, passed through a 0.45 μm membrane filter (Millipore, Bedford, MA), and stored at –80°C until use. All the HEV samples were inactivated by incubation at 70°C for 20 min before using this study. For the selectivity test, the zika virus (PRVABC-59) was kindly provided by Professor K. Morita of the Institute of Tropical Medicine, Nagasaki University, and Dr. Fuyuki Abe of the Department of Microbiology, Shizuoka Institute of Environment and Hygiene, respectively.

4.2.3 Preparation of Antibody-conjugated nanomaterials

4.2.3.1 Preparation of Antibody-conjugated A-MNPs, PP@PLGA, and TP@PLGA

The anti-IV/A/HA, anti-IV/A/H1N1, and anti-IV/A/H3N2 antibodies were conjugated to A-MNPs, PP@PLGA, and TP@PLGA, respectively, using EDC/NHS carbodiimide conjugation as described in our previous work (Ganganboina et al. 2020b). EDC/NHS carbodiimide chemistry conjugation activates the carboxylic group of the polymeric PLGA membrane of the polymeric nanocarrier and reacts to the amine group on the antibodies. The EDC/NHS chemistry results in the amide bond between the polymeric nanocarrier and the antibodies. As A-MNPs lack a carboxylic group, A-MNPs are initially reacted to succinic anhydride, converting the primary amine group on the surface of the A-MNPs into the carboxylic group by forming an amide bond. The COOH-MNPs are magnetically purified from excess succinic anhydride. Then, the carboxylic group is first activated with EDC and magnetically separated to remove excess EDC reagent. Then, NHS and antibodies are added

to the EDC-activated MNPs to form the amide bond with the amine group of the antibodies. The antibody-conjugated PP@PLGA and TP@PLGA were purified by mild centrifugation and antibody-conjugated magnetic nanoparticles (Ab-MNPs) by magnetic separation and kept in PBS buffer. Blocking of the free surface of Ab-MNPs was carried out using 2% BSA.

4.2.3.2 Preparation of Anti-HA conjugated TMB-NPs@PLGA

The conjugation of anti-HA antibody (Ab) or Anti-IV/A/H3N2 Ab to TMB-NPs@PLGA was done by EDC/NHS conjugation chemistry. In brief, 0.1 M EDC was mixed with TMB-NPs@PLGA, and EDC reacted with the carboxyl group of the PLGA to create an active-ester intermediate within 60 min of stirring at room temperature. Then, 0.1 M NHS solution and 5.1 µg of antibody solution (in phosphate-buffer saline (PBS) were added to enable an amine reaction between an amino group and activated carboxyl-ester and stirred continuously at 7 °C for 16 h. The reaction solution was dialyzed using a 1 kDa dialysis bag to remove unreacted EDC and NHS. Finally, the stock solution of antibody-conjugated TMB-NPs@PLGA in 0.1 M PBS (pH 7.4) was stored at 4 °C.

4.2.4 Detection of Influenza Virus using TMB-NPs@PLGA based immunoassay

Briefly, 100 µL of anti-HA Ab (10 ng/mL) was added into the microtiter plate wells and incubated overnight for immobilization. Followed by the Ab immobilization, the free matrix within the well in the wells was blocked with BSA. The wells were washed with PBS containing 0.1% Tween-20 after each step. Different concentrations of the target virus, IV/H1N1, was added to the wells and incubated for 1 h. Further, 100 µL of anti-HA Ab-TMB-NPS@PLGA complex was added into the wells and incubated for an additional 1 h. The captured IV/A/H1N1 were bound to the anti-HA Ab-TMB-NPs@PLGA, forming the immunocomplex sandwich. The wells were washed with PBS to remove the excess reagents

and interfering substances. After the separation, 50 µL of the DMSO solution was added to disrupt the PLGA nanovesicles and release the encapsulated TMB-NPs. One hundred microliters of prepared substrate solution (H_2O_2 and CuNFs) were added to the wells, and blue color developed rapidly. After 5 min, 10% H_2SO_4 was added to stop the reaction, resulting in changing the blue color to yellow, followed by the absorbance measurement.

4.2.5 Detection of Influenza Virus using Dye@PLGA-based immunoassay

Briefly, the IV/A was prepared in dilution concentration from nanogram level to femtogram level. For IV/A/H1N1 detection, each vial containing the virus was added with 50 µL Ab-MNPs and 50 µL Ab-PP@PLGA and mixed for 2 minutes by pipetting motion by 20 min-incubation time to form the sandwich structure between Ab-MNPs, IV/A, and Ab-PP@PLGA Polymeric nanocarrier. Afterward, the unbound Ab-PP@PLGA in the supernatant was removed by magnetic separation, and the washing step was done with PBS buffer. To exhibit the colorimetric detection, the redispersed sandwich structure Ab-MNPs/(IV/A)/Ab-PP@PLGA was reacted to an alkaline solution. The developed color was measured with a UV-Vis microplate reader.

4.2.6 Detection of NoV-LPs using PtNPs@Co_3O_4 NCs based immunoassay

The developed PtNPs@Co_3O_4-based immunoassay was assayed initially for NoV-LPs detection. Firstly, 100 µL of Ab_{NoV} (100 ng/ml) was immobilized in the microtiter plate wells by overnight incubation at 4^{o}C. Afterward, the wells would be washed by 250 µL 1 × PBS-T three times between each detection step. After immobilization of Ab_{NoV}, the wells were blocked using 2% BSA for 2 h. Subsequently, various concentrations of NoV-LPs were introduced for 1 h, and 100 µL Ab_{NoV}-PtNPs@Co_3O_4 NCs were added and incubated for 1 h. During this stage,

captured NoV-LPs were bound in sandwich formation to Ab_{NoV}-PtNPs@Co_3O_4 NCs. After washing, 100 µl of the reaction solution, containing 250 µl H_2O_2 and 500 µl of TMB solution in 5 ml of acetate buffer (pH=5.2), was added to each well, and incubation was performed for 10 min in the dark. The stop solution of 10% H_2SO_4 was added to obtain oxidized TMB from quinone complex TMB form. After that, absorbance was measured at 450 nm wavelength; 650 nm was used as a reference wavelength) was recorded.

4.3 Results and Discussion

4.3.1 TMB-NPs@PLGA based immunoassay

4.3.1.1 Working principle

The working principle of the developed TMB-NPs@PLGA-based colorimetric sensing method for ultrasensitive detection of IV/A/H1N1 is shown in **Figure 4.1**. It comprises TMB-NPs-encapsulated PLGA nanovesicles (TMB-NPs@PLGA), which are collective self-assembled TMB molecules and bovine serum albumin (BSA) inside PLGA nanovesicles **(Figure 4.1a)**. Initially, the anti-HA Ab is immobilized in the microtiter plate wells via hydrophobic interaction with the polystyrene of the microplate. Different concentrations of the target IV/A are added to the anti-HA Ab immobilized wells **(Figure 4.1b)**. Further, anti-HA Ab-conjugated TMB-NPs@PLGA are added to the wells allowing the formation of an immunocomplex sandwich structure. Anti-HA Ab-conjugated TMB-NPs@PLGA and anti-HA Ab formed a sandwich-like structure with IV/A, as shown in **Figure 4.1c**. After incubation, the wells are washed with PBS to remove the excess reagents and unbound anti-HA Ab-conjugated TMB-NPs@PLGA. After that, the successfully separated TMB-NPs@PLGA sandwich nanoconjugates in the wells are treated with DMSO to dissolve the PLGA membrane and release the encapsulated TMB-NPs **(Figure 4.1d)**. The dissolving of the TMB-NPs@PLGA

represents the first step of releasing the signal molecules in the system. Additionally, the released TMB-NPs are also dissolved by the DMSO solution, acquiring highly concentrated TMB in the solution **(Figure 4.1e)**, marking the second step of presenting the signal molecules in the system. The mixture of self-assembled CuNFs as peroxidase-mimicking nanomaterials and H_2O_2 solution is added to the wells to facilitate the catalytic oxidation of released TMB **(Figure 4.1f),** exhibiting the color signals as the proportional to quantification of the captured virus. The immunocomplex sandwich structure between TMB-NPs@PLGA and the bounded virus will not form in the absence of the target virus. Without the TMB-NPs@PLGA in the system, there is an absence of TMB to be oxidized by CuNFs and H_2O_2 mixture for generating a colorimetric signal.

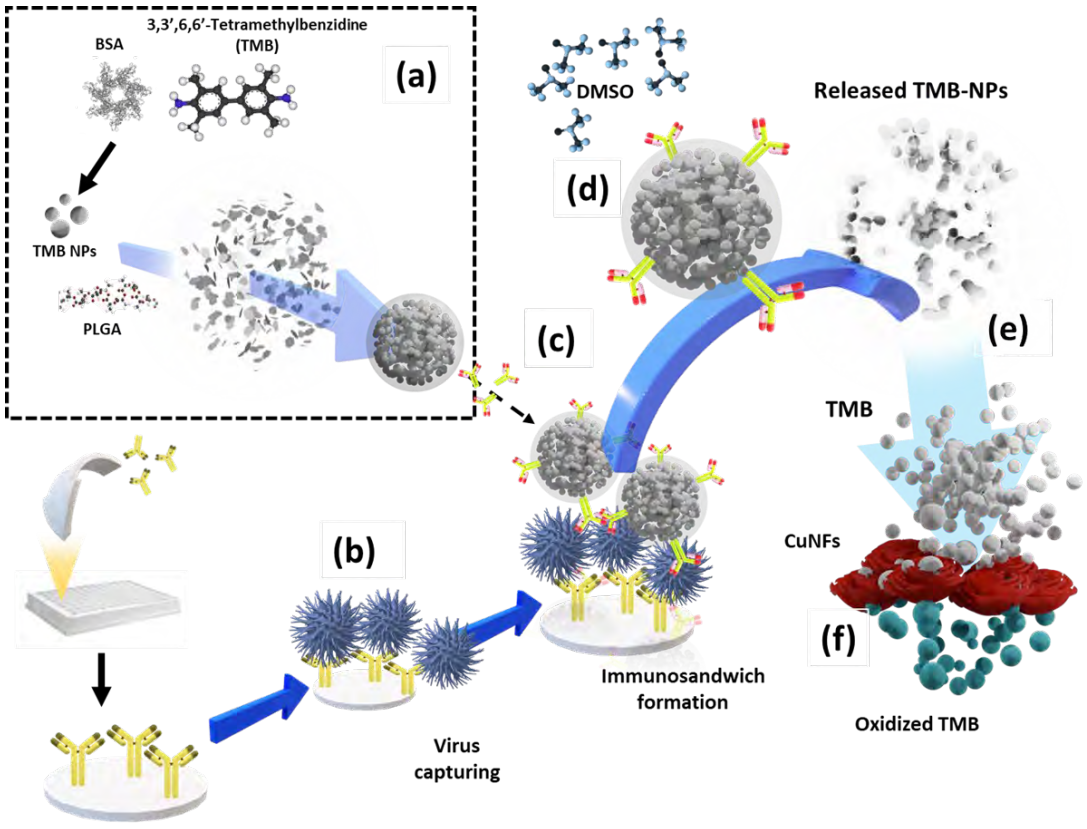

Figure 4.1 The schematic illustration of the TMB-NPs@PLGA-based signal amplification platform. (a) The preparation of TMB-NPs@PLGA; (b) Viruses are captured by the capture probe; (c) Immunosandwich structured nanoconjugate with TMB-NPs@PLGA in the presence of virus; (d) Addition of DMSO and the dissolving of the PLGA nanovesicle; (e) The release of TMB-NPs due to the dissolving of TMB-NPs by DMSO and (f) the catalytic oxidation of TMB by CuNFs/H_2O_2 for colorimetric detection.

4.3.1.2 Optimization of the immunoassay

In this work, the significant points for the signal amplification strategy for immunoassay purposes are the maximal encapsulation of TMB-NPs inside the PLGA nanovesicles and the reaction time required to develop the color change. Firstly, the loading amounts of TMB-NPs are optimized to achieve maximal encapsulation inside the PLGA nanovesicles. The as-prepared TMB-NPs solutions of 25, 50, 75, and 100 mg /mL are used for the PLGA encapsulation, with 0 mg /mL representing empty PLGA nanovesicle. As shown in **Figure 4.2a**, it is evident that the absorbance signal continuously increased along with the increasing concentrations of TMB-NPs, attributing to the increase of TMB-NPs concentration in the presence of CuNFs and H_2O_2. To optimize the encapsulated number of TMB-NPs in the PLGA nanovesicles, the assay is performed using various concentrations of TMB-NPs encapsulated in PLGA nanovesicles with and without the DMSO. It can be seen that there is no signal amplification with and without the addition of DMSO in empty PLGA nanovesicles, showing the TMB signal solely in the form of TMB-NPs. By comparing the signal generated before and after the DMSO addition, 75 mg /mL is the optimal loading concentration in the PLGA nanovesicles.

Further, based on the absorbance value, the concentration of corresponding TMB molecules is calculated corresponding to its molar absorption coefficient. The concentration of the catalytic oxidized TMB molecules is estimated at 43.1 mg /mL, which indicates the loading capacity of the PLGA nanovesicle is up to 53.4%. The absorbance change upon the release of TMB-NPs from PLGA nanovesicles synthesized using 100 mg /mL is relatively similar to 75 mg /mL. The difference in absorbance intensity before and after the release of TMB-NPs upon the addition of DMSO that is expressed in the change of absorbance is highly desirable for obtaining sensitive and reliable detection. Therefore, TMB-NPs@PLGA nanovesicles,

synthesized using 75 mg /mL of TMB-NPs solution, are used to prepare TMB-NPs@PLGA in further experiments.

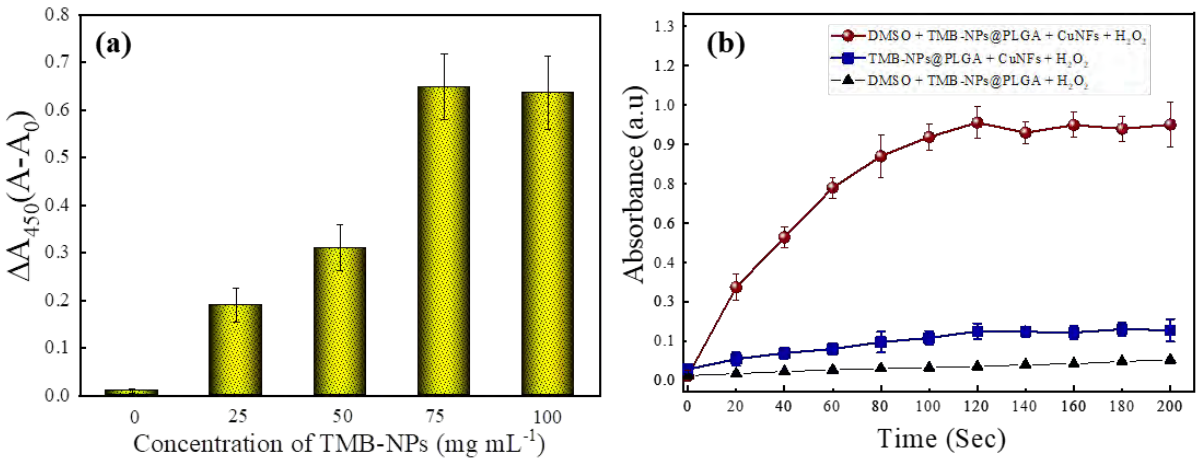

Figure 4.2 (a) The encapsulation amounts of TMB-NPs in PLGA nanovesicles and (b) the incubation time for the change in absorbance intensity of TMB-NPs, CuNFs, and H_2O_2 mixture

Figure 4.2b shows the incubation time as the change in absorbance in the mixture of TMB-NPs@PLGA and CuNFs/H_2O_2 with and without DMSO. Before the optimization, the TMB-NPs@PLGA was reacted with only H_2O_2. Low absorbance was shown due to no involvement of the catalytic reaction by CuNFs and grounding the need for the CuNFs as a nanozyme. Next, although there is increasing in the absorbance response compared to only H_2O_2, a slight change in absorbance is observed in TMB-NPs@PLGA incubated with CuNFs/H_2O_2. In contrast, the absorbance is noticeably and gradually increases after adding DMSO and incubation of TMB-NPs@PLGA with CuNF/H_2O_2. The absorbance increases rapidly from 0 to 100 sec of the incubation time, and the stationary absorbance intensity is observed after 120 sec. There is a provision period to maximize the signal, mainly laid on the equilibrium of the redox reaction between the TMB/H_2O_2 system and CuNFs. After the equilibrium, the absorbance is constant until 200 sec. Therefore, the reaction time for

developing the color is optimized to be 120 sec in the developed colorimetric immunoassay for virus detection.

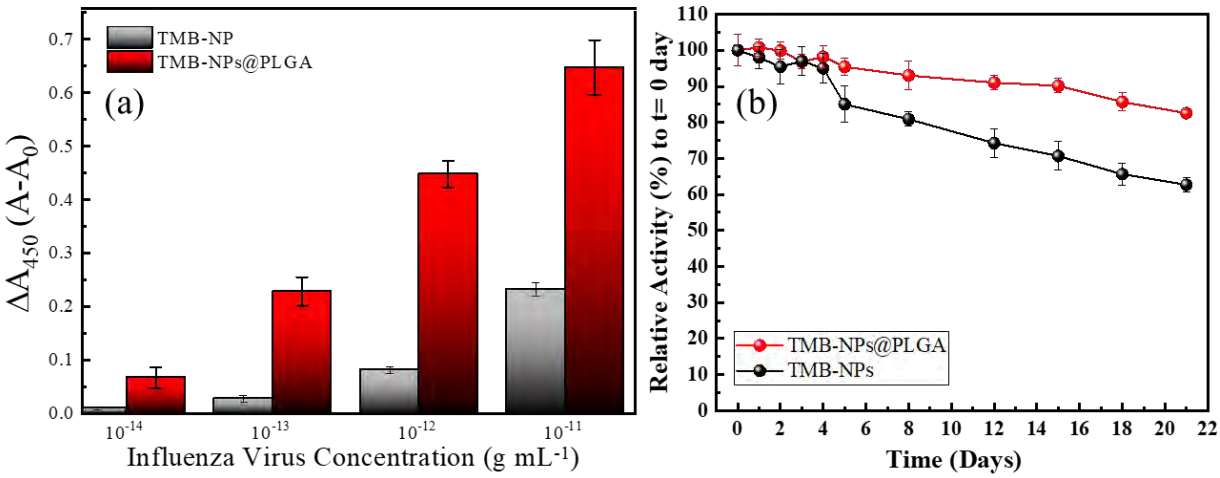

Figure 4.3 The comparison of IV/A detection using TMB-NPs@PLGA and TMB-NPs. A0 and A indicate the absorbance before and after the addition of DMSO, respectively. The error bars indicate the SD of the triple measurement.

The main point weighted heavily is the nanoparticle encapsulation-based signal amplification strategy in this colorimetric immunoassay to achieve a highly sensitive detection limit. First, to underline the advantage of the encapsulation of TMB-NPs inside the PLGA nanovesicles in amplifying the signal, the bare TMB-NPs, which are self-assembled with anti-HA Ab and BSA, are used instead of TMB-NPs@PLGA for detecting IV/A. Hypothetically, the TMB-NP can demonstrate a color signal for IV/A detection similar to the TMB-NPs@PLGA. Based on antigen-antibody interaction, a sole immunocomplex can only be abutted with a single TMB-NP. In contrast, the encapsulation of TMB helps localization of the signal substrate and enriches the signal generation for individual antibody-antigen binding. The IV detection immunoassay using bare TMB-NPs and TMB-NPs@PLGA is shown in **Figure 4.3a**. Interpreting the difference in the absorbance signal, it can be understandably stated that 100-fold higher detection sensitivity is achieved by utilizing the TMB-NPs@PLGA compared to only

TMB-NPs. The encapsulation of the TMB-NPs localizes a higher concentration of TMB molecules even at a low concentration of the virus up to 3.5-folds of localized concentration of the colorimetric signal. Further, after storing the conjugates nanomaterials, as shown in **Fig. 4.3b**, they can retain theirs' activity up to 7 days and noticeably decreasing activity was observed on both nanomaterials with Ab-TMB-NPs down to 60% and Ab-TMB-NPs@PLGA down to 85%, showing a good encapsulation of PLGA enhancing the stability.

Besides the encapsulation of the signal molecules, in the juxtapose to our previous work (Ahmed et al. 2016a; Khoris et al. 2020a) using electrostatic interaction as the conjugation force, the chemical conjugation of the antibodies on the nanovesicles upholds the increase of the antibody-antigen by preventing the random confirmation on the antibodies. Moreover, the PLGA nanovesicles provide the conjugation site; instead of the TMB-NPs, the reactivity and morphology of the NPs are well-preserved within the PLGA nanovesicles. Lastly, the encapsulation of TMB molecules instead of the nanozyme like noble metals or metal oxide nanoparticles (Ganganboina et al. 2020b; Ye et al. 2017) shows more effective signal generation. The catalytic oxidation of the TMB molecules as the determining factor is reflected in the low value of the K_m of the CuNFs, which is shown in numerous published nanozymes (Ganganboina and Doong 2018; Oh et al. 2018; Zhou et al. 2017). Subjection to the low detection limit, the reactiveness of the collective TMB molecules in the form of NPs within the PLGA nanovesicles is essential for amplifying the signal in immunoassay format.

4.3.2 Dye@PLGA-based immunoassay

4.3.2.1 Working principle

Antibodies-conjugated A-MNPs (Ab-MNPs), antibodies-conjugated PP@PLGA (Ab-PP@PLGA), and TP@PLGA (Ab-TP@PLGA) were introduced into the system to separate

and detect the IV/A. As the capturing probe, A-MNPs were conjugated to antibodies specific to H1, H2, and H3. PP@PLGA and TP@PLGA were conjugated with antibodies specific to H1N1 and H3N2. Ab-MNPs and Ab-PP@PLGA or Ab-TP@PLGA will bring substrate and the binding virus for signal generation. As shown in **Figure 4.4**, Ab-MNPs, Ab-PP@PLGA, and Ab-TP@PLGA were introduced to the IV/A solution (sample) (**Figure 4.4a**). After the Ab-MNPs/(IV/A)/(Ab-PP@PNLs or Ab-TP@PLGA) immuno-sandwich complex was formed, the magnetic field separated it, and non-binding PP(TP)@PLGA were removed from the system (**Figure 4.4b**). The separated complex was redispersed and transferred to the reaction chamber containing 1 M NaOH solution (**Figure 4.4c**). As the alkaline solution disrupts the polymeric membrane and exposes the chromogen to the hydroxide ions, the color is developed in the well plate. The color develops depending on the amount of chromogen in the bound Ab-PP(TP)@PLGA in the sandwich complex. As the formation of the sandwich complex can be limited to the amount of the viruses, and the unbound chromogen carrier is washed out, the presence of the virus can be quantified by the color developed.

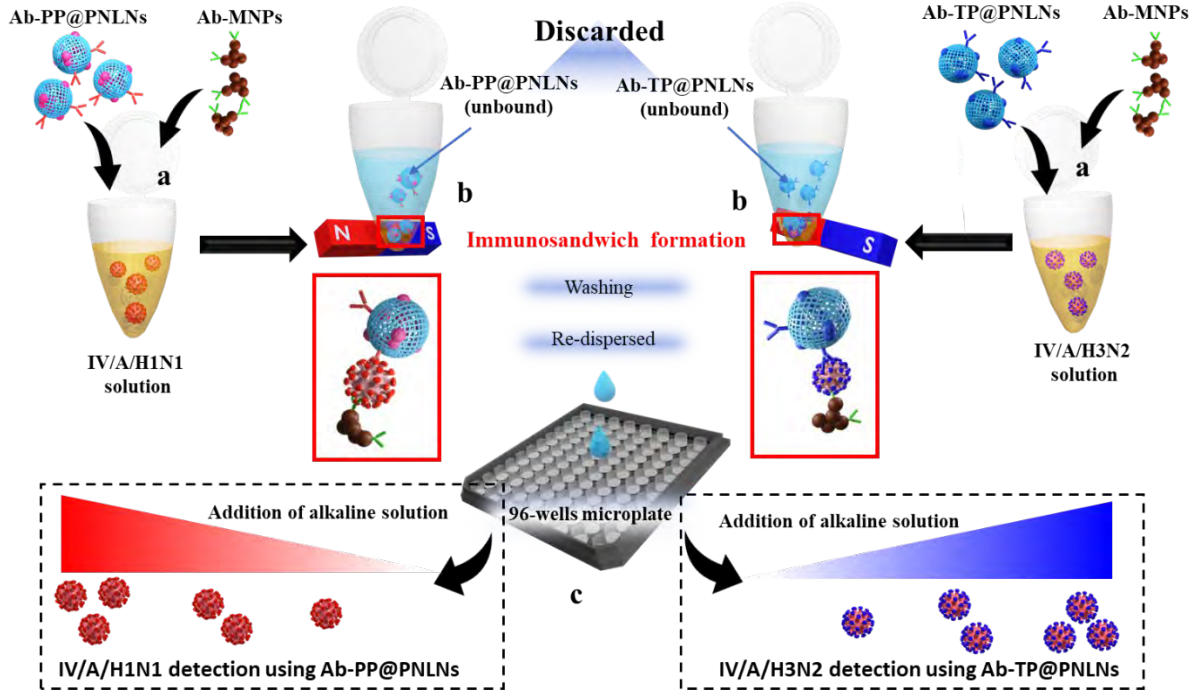

Figure 4.4 The schematic illustration of the PNLNs-based biosensor

4.3.2.2 Optimization of the immunoassay

To be applied in the virus biosensing, the nanocarrier, Polymeric nanocarrier, and the magnetic nanoparticles (MNPs) are required to be conjugated with specific antibodies against the target virus, IV/A. As shown in **Figure 4.5**, ELISA results show higher absorbance in antibodies-conjugated Polymeric nanocarrier (Ab-Polymeric nanocarrier) and MNPs (Ab-MNPs) than those in only Polymeric nanocarrier and MNPs, respectively. In the ELISA, the free antibodies and BSA 2% are used as the positive control and negative control.

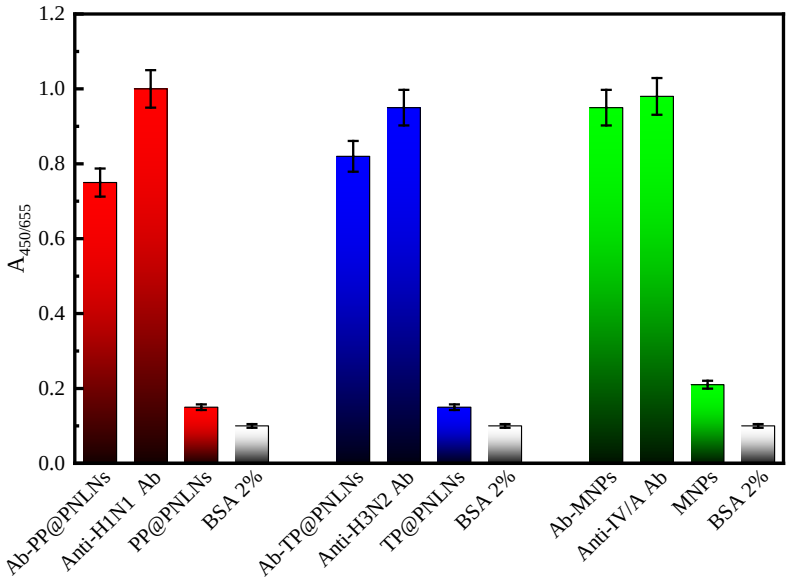

Figure 4.5 Antibody confirmation of the nanomaterials by ELISA

To understand the advantage of the higher loading capacity of the nanocarrier for biosensing purposes, a comparative study is conducted on the IV/A/H1N1 detection using one-solvent mixture-prepared PP@PLGA (PP@1PLGAs), two-solvent mixture-prepared PP@PLGA (PP@2PLGAs), and three-solvent mixture-prepared PP@PLGA (PP@3PLGAs). Three kinds of Ab-PP@PLGA are assayed to the immobilized IV/A/H1N1 solution on the 96-wells microplate. After IV/A/H1N1 was added to the antibody-conjugated PP@PLGA (Ab-PP@PLGA), the well was rinsed to remove unbound Ab-PP@PLGA. The bound Ab-PP@PLGA was alkaline treated, and the color developed was measured. **Figure 4.6** indicates

that Ab-PP@1PLGAs-based biosensor demonstrated the lowest detection signal, followed by Ab-PP@2PLGAs, and Ab-PP@3PLGAs generated the highest signal. Three of the PP@PLGAs show negligible signal in the absence of IV/A/H1N1. This highlights that the three-solvent mixture-prepared Dye@PLGA, which has the highest loading of the chromogen, also provides the highest signal amplification in the virus detection implicating the fundamental advancement in the nanocarrier-based biosensor.

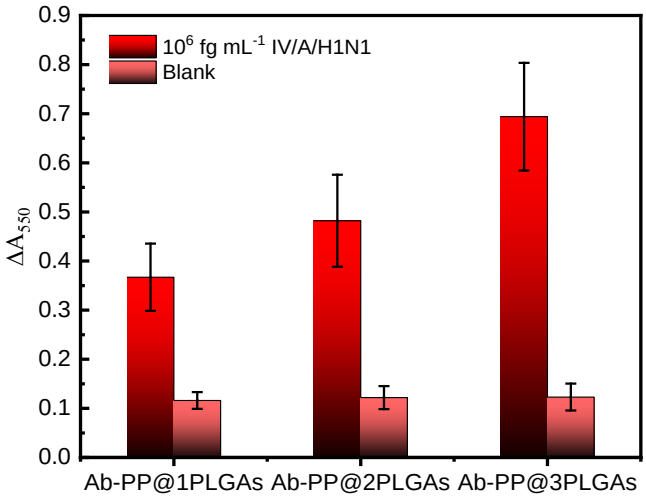

Figure 4.6 The influenza virus detection using Ab-PP@#PNLNs-based biosensor (#=solvent mixtures). The error bars represent the standard deviation of three measurements.

The initial assessment demonstrates the essential components for the immunosandwich formation of Ab-MNPs, IV/A, and Ab-PP(TP)@PLGA. IV/A/H1N1 were mixed with only Ab-MNPs or only Ab-PP@PLGA, or both. As shown in **Figure 4.7a**, only when Ab-MNPs and Ab-PP@PLGA were added to the IV/A/H1N1 solution there is a positive signal, demonstrating the increased absorbance at A_{550}. This shows each component is essential to isolate the virus specifically and generates the detection signal. Additionally, as shown in **Figure 4.7b**, the immunosandwich is roughly visualized by TEM image analysis due to the high contrast of electrons between the MNPs and virus and Polymeric nanocarrier. In addition,

Figure 4.7c shows that the immunosandwich structure is not observed after the alkaline solution is added to the nanocomposite.

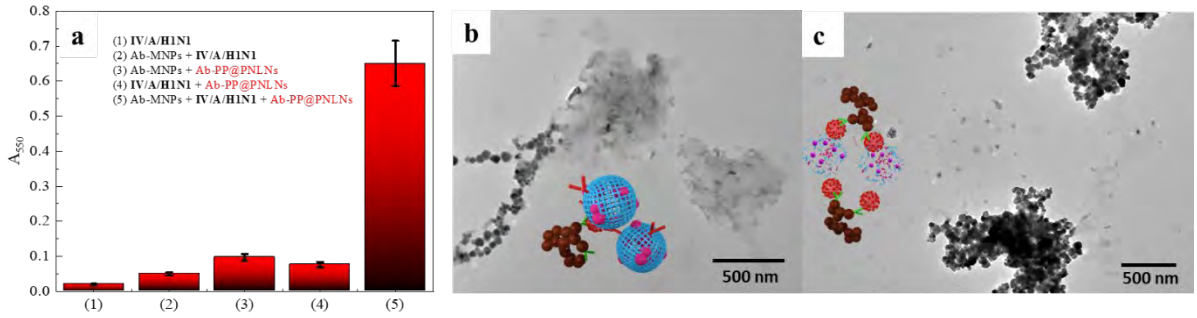

Figure 4.7 (a) Absorbance signal in the immunoassay based on various components (Abs-MNPs, IV/A/H1N1, or PP@PLGAs), (b) and (c) showed TEM analysis of the immuno-sandwich formation before and after alkaline treatment

4.3.3 PtNPs@Co_3O_4 NCs-based immunoassay

4.3.3.1 Working principle

PtNPs@Co_3O_4 nanocage (NCs) was utilized as a nanozyme in immunoassay development. The NCs' utility came from the oxidation of Co into metal oxides Co_3O_4 activating the non-catalytic active ZIF-67 as peroxidase-mimic nanozymes; and the embodiment of other nanozyme, PtNP, in the Co_3O_4 NCs. The preserved well-defined morphology of PtNPs@Co_3O_4 NCs in the synthesis process was illustrated in **Figure 4.8a**. At first, capturing Ab was immobilized (**Figure 4.8b**). As probes in virus sensing, antibody-conjugated PtNPs@Co_3O_4 NCs (**Figure 4.8c**) were introduced in the detection well and formed a sandwich immunostructure to the captured norovirus or SARS-CoV-2 proteins (**Figure 4.8d**). Afterward, chromogen 3,3',4,4'-tetramethylbenzidine (TMB), and hydrogen peroxide (H_2O_2) were employed in the detection. The bound PtNP@Co_3O_4 NCs catalyzed the oxidation of the TMB (**Figure 4.8e**).

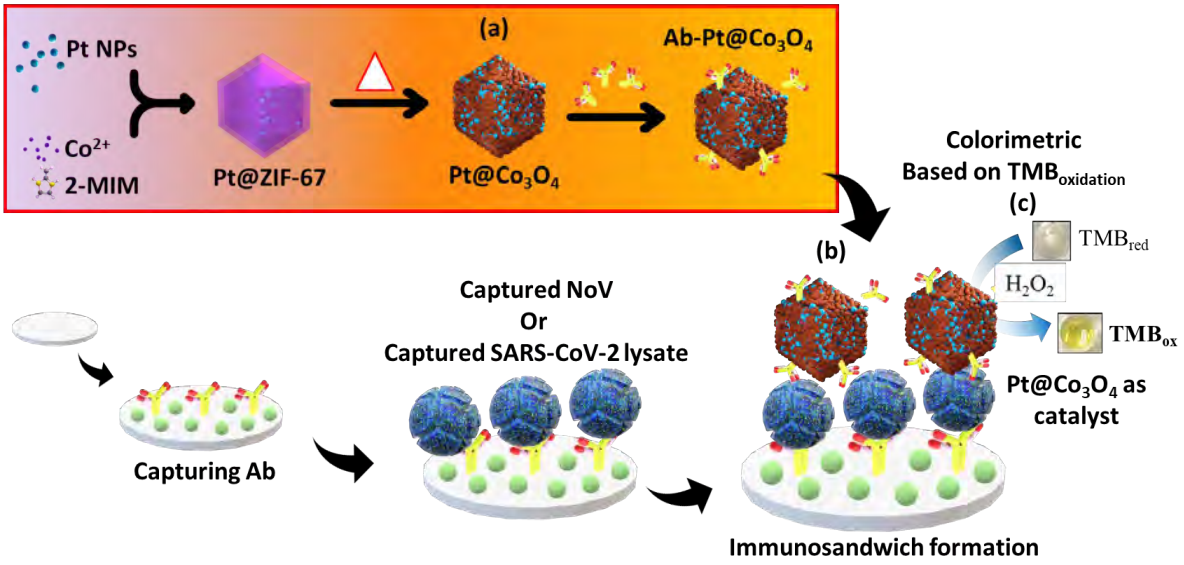

Figure 4.8 Schematic Illustration of the PtNPs@Co_3O_4 NCs-based immunoassay

4.3.3.2 Optimization of the immunoassay

Immunoassay aims to provide a high signal-to-noise ratio. From the perspective of its catalytic activity, PtNPs have been demonstrated to play a vital role in inducing high catalytic activity in a low concentration range. To maximize the performance of the immunoassay, there is a need to optimize the PtNPs embodiment in the Co_3O_4 NCs. By introducing higher PtNPs in the imidazole precursor, it intended to bring more PtNPs inside the ZIF-67 nanostructure. To do so, various PtNPs concentrations (0.25, 0.5, 1.0, 3.0 mg/mL) was added in the preparation of the $PtNPs_x@Co_3O_4$ NCs with x represented as 1, 2, 3 and 4, respectively. Co_3O_4 NCs were used as a negative control. Then, the $PtNPs_x@Co_3O_4$ NCs nanozymes were obtained through pyrolysis of $PtNPs_x$@ZIF-67 in air, and the morphology was analyzed by TEM analysis, as shown in **Figure 4.9.** The obtained $PtNPs_0@Co_3O_4$ NCs to $PtNPs_3@Co_3O_4$ have a size of around 300 nm. In the case of $PtNPs_4@Co_3O_4$, NCs showed a bigger size of 700 – 800 nm and an indication of low uniformity and agglomeration.

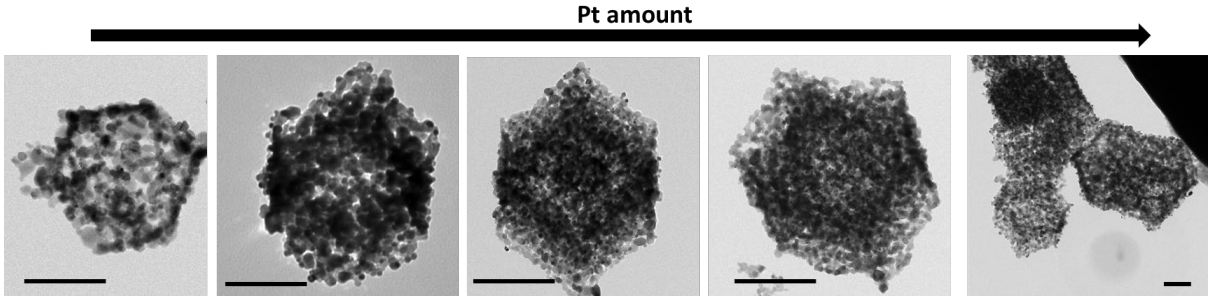

Figure 4.8 TEM analysis of the PtNPs@Co_3O_4 NCs with various concentrations of PtNPs as a precursor

Further, The Pt amount was analyzed based on the X-ray counts from the EDS analysis (**Figure 4.10**). As expected, the Pt amount is increased proportionally to the amount of PtNPs introduced as the precursor. The $PtNPs_4$@Co_3O_4 NCs have the highest Pt amounts, up to 38.84%, followed by $PtNPs_3$@Co_3O_4 NCs, around 32.44 %Pt.

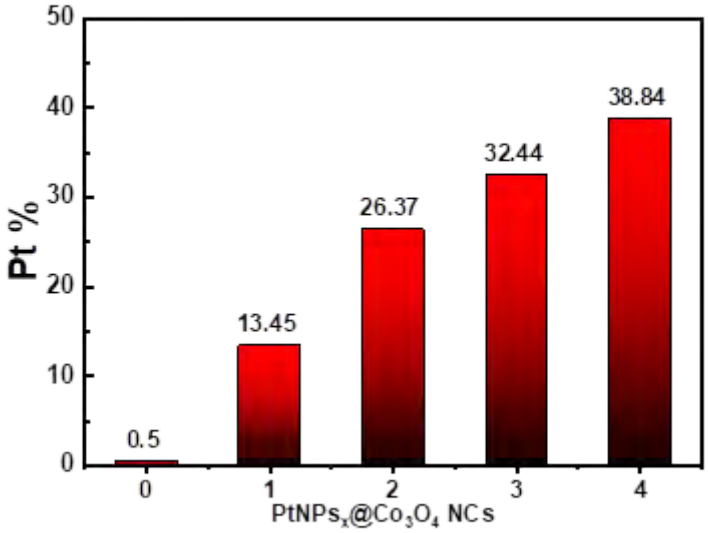

Figure 4.10 Pt amount (in % based on elemental analysis data) of the PtNPs@Co_3O_4 NCs (x = 0 indicates only Co_3O_4 NCs with no PtNPs added as a precursor)

To evaluate the optimal $PtNPs_x$@Co_3O_4 NCs as immunoassay conjugates, the $PtNPs_x$@Co_3O_4 NCs were functionalized with antinorovirus antibody (Ab_{NoV}), forming Ab_{NoV}-

conjugated $PtNPs_x@Co_3O_4$ NCs. The Ab_{NoV}-$PtNPs_x@Co_3O_4$ NCs were assayed on 10 ng/mL norovirus-like particles (NoV-LPs) and bovine serum albumin (BSA) (as a negative control/ blank). The NoV-LPs were used as the protein model of infectious NoV. The results of the assay were plotted in **Figure 4.10**. In the case of a blank signal, the absorbance was obtained around 0.05 – 0.12. The positive signal was obtained higher than the blank signal in all cases of $PtNPs_x@Co_3O_4$ NCs. $PtNPs_0@Co_3O_4$ NCs showed the lowest positive signal around 0.15 $A_{450/655}$ value because of low catalytic activity coming from the Co_3O_4 NCs. The difference between the positive and blank signals suggested that instead of the 38.84%Pt $PtNPs_4@Co_3O_4$, $PtNPs_3@Co_3O_4$ NCs with 32.44%Pt showcased the highest positive-to-blank signal in detecting 10 ng/mL NoV-LPs around absorbance of 0.7.

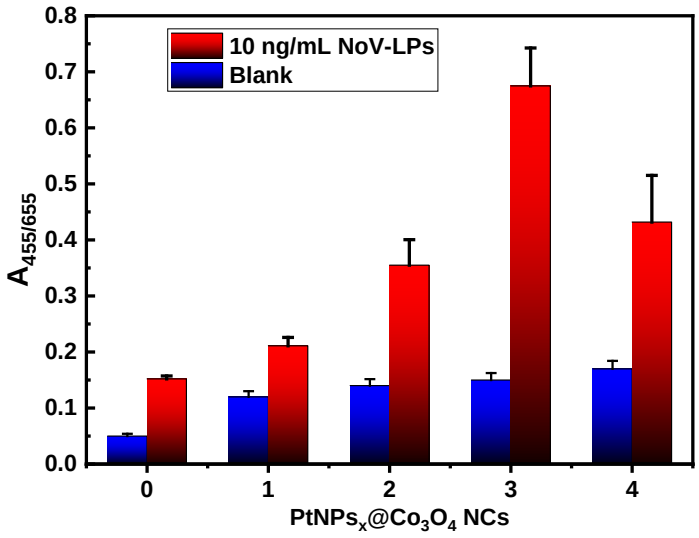

Figure 4.11 The optimization of $PtNPs@Co_3O_4$ NCs-based immunoassay according to the precursor amount of PtNPs

Interestingly, the highest %Pt in $PtNPs@Co_3O_4$ NCs does not ensure the highest applicability of the NCs nanozyme. Several reasons could be elaborated to explain the results. (1) As $PtNPs_4@Co_3O_4$ has a bigger size than the $PtNPs_3@Co_3O_4$ with around 2-folds in diameter, Ab_{NoV}-$PtNPs_4@Co_3O_4$ experiences a higher steric hindrance in the immunoassay, reducing the number of the binding nanozyme in the virus-antibody conjugation (Zhan et al.

2017). (2) the size of the $PtNPs_4@Co_3O_4$ NCs leads to lower specific surface area (ratio of surface area to volume) of the nanozyme, lowering the catalytic activity (Fan et al. 2021) and stability of antibodies (Busch et al. 2019). Overall, $PtNPs@Co_3O_4$ NCs demonstrated a low blank signal because of proper blocking by BSA, denying non-specific binding from the NCs. It is indicated that the porous structure of the NCs and high surface area were only accessible to the small molecules such as the substrates, H_2O_2 and TMB. (Long et al. 2021).

4.4 Conclusion

The main purpose of this section was to elucidate the working principle of the signal amplification in the capture immunoassay purpose, which included replacing the natural enzyme peroxidase from ELISA and substituting it with TMB-NPs@PLGA-based immunoassay in 96-wells microtiter plates and using CuNFs nanozyme, dye@PLGA nanocarrier-based immunoassay using magnetic pre-separation, or $PtNPs@Co_3O_4$ NCs-based immunoassay in a 96-wells microtiter plate. The working immunoassay was optimized mainly focusing on the maximal properties of the nanomaterials, meaning that the optimization is based on the maximal encapsulation of the signal substrates for nanocarrier and maximal metal contents for nanozyme. The optimization was also compared to the counterpart nanomaterials. This insisted that the nanocarrier demonstrated higher signal generation compared to the individual nanoprecipitation, and the derived nanozyme was superior to its preceded precursor nanomaterials. Platform was demonstrated its capability to detect fecal NoV from humans and fecal HEV from a monkey.

Chapter 5

Signal Amplified Virus Detection System in Colorimetric System

Chapter 5. Signal Amplified Virus Detection System in Colorimetric System

5.1 Introduction

In this section, the main discussion was to evaluate the utilization of the proposed enhanced catalytic activity of gold nanoparticles as nanozyme. The discussed mechanism of the silver shell deposition on AuNPs was applied to gold nanozyme in the capture immunoassay to form *in situ* AuNPs@Ag. The capture immunoassay was demonstrated to detect clinically isolated NoV and periodically detect fecal HEV from the monkey. The colorimetric signal was compared to commercial ELISA and RT-qPCR as the gold standard.

5.2 Methods

5.2.1 Detection of Influenza Virus, clinically isolated Influenza Virus and SARS-CoV-2 spike protein (S-protein SARS-CoV-2) using TMB-NPs@PLGA based immunoassay

Briefly, 100 μL of anti-HA Ab (10 ng/mL) was added into the microtiter plate wells and incubated overnight for immobilization. Followed by the Ab immobilization, the free matrix within the well in the wells was blocked with BSA. The wells were washed with PBS containing 0.1% Tween-20 after each step. Different concentrations of the target virus, IV/H1N1, were added to the wells and incubated for 1 h. Further, 100 μL of anti-HA Ab-TMB-NPS@PLGA complex was added into the wells and incubated for an additional 1 h. The captured IV/A/H1N1 were bound to the anti-HA Ab-TMB-NPs@PLGA, forming the immunocomplex sandwich. The wells were washed with PBS to remove the excess reagents and interfering substances. After the separation, 50 μL of the DMSO solution was added to disrupt the PLGA nanovesicles and release the encapsulated TMB-NPs. One hundred microliters of prepared substrate solution (H_2O_2 and CuNFs) were added to the wells, and blue color developed rapidly. After 5 min, 10% H_2SO_4 was added to stop the reaction, resulting in

changing the blue color to yellow, followed by the absorbance measurement. Clinically isolated IV/A/Yokohama/110/2009/H3N2 was applied following the same protocol as IV/A/H1N1 using anti-IV/A/H3N2 Ab-conjugated TMB-NPs@PLGA to confirm the versatility of the assay system. For the specificity of the developed immunoassay, six control experiments were performed: 100 pg/mL of HEV-LPs, NoV-LPs, 10^4 copies/mL of WSSV, and 10^3 PFU/mL of Zika virus, 20 μg/mL of norovirus and mixture all the viruses.

4.2.2 Detection of subtype Influenza Virus H1N1 and H3N2 using Polymeric nanocarrier-based immunoassay

Briefly, the IV/A was prepared in dilution concentration from nanogram level to femtogram level. For IV/A/H1N1 detection, each vial containing the virus was added with 50 μL Ab-MNPs and 50 μL Ab-PP@PLGA and mixed for 2 minutes by pipetting motion by 20 min-incubation time to form the sandwich structure between Ab-MNPs, IV/A, and Ab-PP@PLGA Polymeric nanocarrier. Afterward, the unbound Ab-PP@PLGA in the supernatant was removed by magnetic separation, and the washing step was done with PBS buffer. The redispersed sandwich structure Ab-MNPs/(IV/A)/Ab-PP@PLGA was reacted to an alkaline solution to exhibit the colorimetric detection. The developed color was measured with a UV-Vis microplate reader. For IV/A/H3N2 detection, Ab-TP@PLGA was added to the virus solution instead of Ab-PP@PLGA/ Further, Ab-PP@PLGA and Ab-TP@PLGA (1:1 v/v) were co-added to the virus solution to perform one-pot subtyping IV/A detection.

4.2.3 Detection of NoV-LPs, NoV and SARS-CoV-2 S protein and N protein using PtNPs@Co_3O_4 NCs based immunoassay

The developed PtNPs@Co_3O_4-based immunoassay was assayed initially for NoV-LPs detection. Firstly, 100 μL of Ab_{NoV} (100 ng/ml) was immobilized in the microtiter plate wells by overnight incubation at 4^{o}C. Afterward, the wells would be washed by 250 μL 1 × PBS-T

three times between each detection step. After immobilization of Ab_{NoV}, the wells were blocked using 2% BSA for 2 h. Subsequently, various concentrations of NoV-LPs were introduced for 1 h, and 100 µL Ab_{NoV}-PtNPs@Co_3O_4 NCs were added and incubated for 1 h. During this stage, captured NoV-LPs were bound in sandwich formation to Ab_{NoV}-PtNPs@Co_3O_4 NCs. After washing, 100 µl of the reaction solution, containing 250 µl H_2O_2 and 500 µl of TMB solution in 5 ml of acetate buffer (pH=5.2), was added to each well, and incubation was performed for 10 min in the dark. The stop solution of 10% H_2SO_4 was added to obtain oxidized TMB from quinone complex TMB form. After that, absorbance was measured at 450 nm wavelength; 650 nm was used as a reference wavelength) was recorded. The same procedure was performed to detect stool containing NoV, spike protein, and nucleocapsid protein of SARS-CoV-2 in 293T whole cell lysate using corresponding sandwich Ab_{NoV} for norovirus detection and $Ab_{SARS\text{-}COV\text{-}2}$ targeting S protein and $Ab_{SARS\text{-}COV\text{-}2}$ targeting N protein for SARS-CoV-2 biomarker protein.

5.3 Results and Discussions

5.3.1 TMB-NPs@PLGA based immunoassay

5.3.1.1 Analytical Performance of the immunoassay

Adopting a typical immunosorbent assay, the colorimetric immunoassay is applied on the increasing concentration of IV/A/H1N1 with the corresponding result of blue color showing a gradient pattern from low to intense blue color and changed proportionally to yellow color after the reaction is stopped. The measured absorbance at 450 nm (with 650 nm as the reference absorbance) increased as the function of the concentration of IV/A/H1N1 (**Figure 5.1a**). The calibration line with a correlation coefficient (R^2) of 0.983 was obtained with satisfactory linearity from 10^1–10^6 fg /mL. Also, the limit of detection (LOD) is 32.37 fg /mL, which is determined by calculating with the equation 3σ/S,30, in which S and σ represent the gradient slope of the calibration line and the standard deviation of the lowest detectable signal, respectively. It was superior t the previously developed methodology for IV detection, as

shown in **Table S1**(Ahmed et al. 2014; Ahmed et al. 2016a; Chang et al. 2010; Lee et al. 2010; Takemura et al. 2017). Two contributing factors exploit the low LOD: the presence of optimized nanozyme concentration and high localized TMB molecules in low antibody-antigen conjugation, inclining the increase in the slope of the detection and generating a signal in the low quantity of immuno-conjugation.

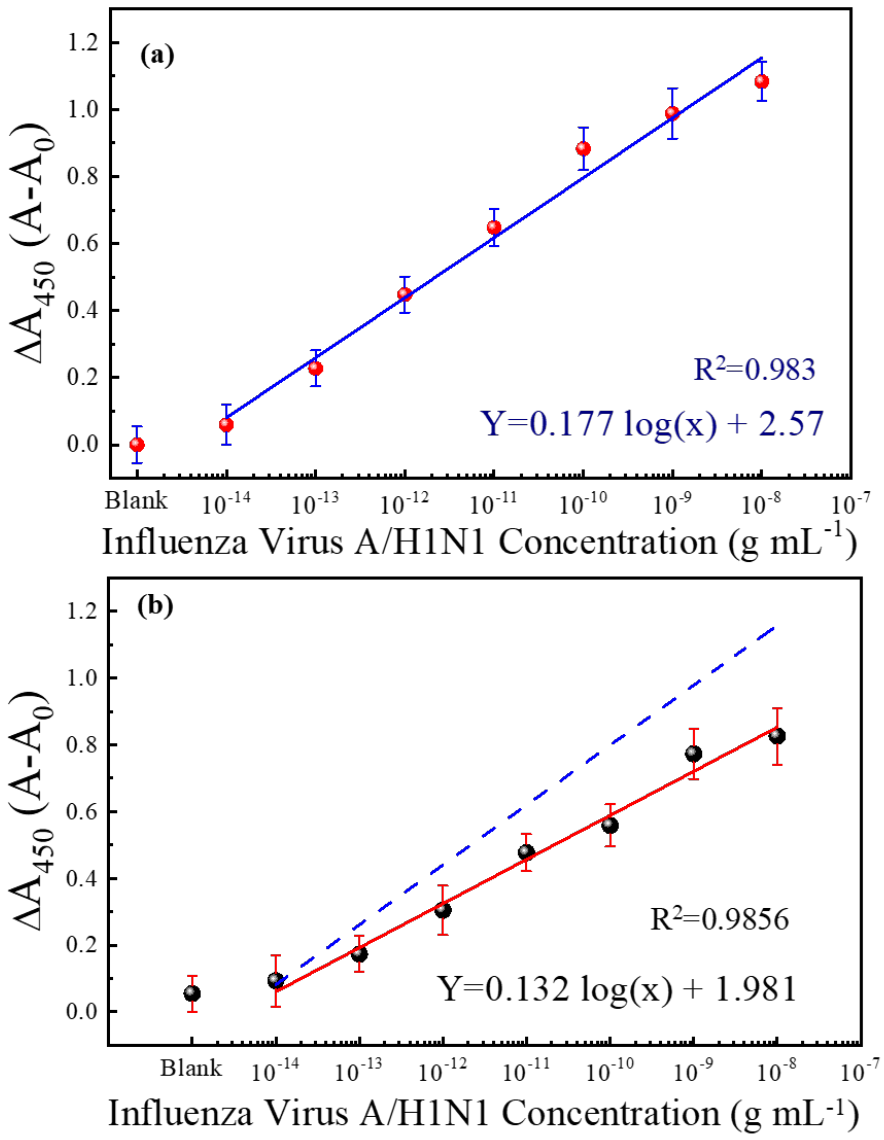

Figure 5.1 Influenza Virus A/H1N1 (IV/A/H1N1) detection using TMB-NPs@PLGA based immunoassay in (a) PBS buffer and (b) spiked 10% human serum

To establish a reliable and practical immunoassay, a dilution series of concentrations of IV/A/H1N1 is spiked in the biological human serum matrix. The developed colorimetric immunoassay shows a linear increase of absorbance to the function of the introduced virus in the medium. **Figure 5.1b** shows the calibration line for IV/A/H1N1 detection using 10% human serum as a detection medium. The gradient of the calibration line is slightly flat shifted compared to the linear calibration from the IV detection in buffer solution up to 15%, however, the responsive linearity.

Table 5.1 Comparative study of IV/A/H1N1 detection

Detection technique	**Strain of IV**	**LOD**
LSPR-induced immunofluorescence	A/New Caledonia/20/99	0.09 pg/mL
Metal enhanced fluorescence	A/New Caledonia/20/99	1 ng/mL
Peroxidase-mimicking nanozyme	A/New Caledonia/20/99	10 pg/mL
LSPR fiber-optic	A/Vietnam/1203/ 2004	13.9 pg/mL
Electrochemical immunosensor	A/Poland/08/2006	2.2 pg/mL
Immunochromatography assay	A/California/12/2009	76.7 ng/mL
TMB-NPs@PLGA based immunoassay	A/New Caledonia/20/99	0.05 pg/mL (This work)

5.3.1.2 Specificity assay

The selectivity of the developed TMB-NPs@PLGA-based colorimetric immunoassay for IV/A/H1N1 detection is evaluated. The dsDNA virus WSSV; the recombinant expressed NoV-LPs and HEV-LPs; and the RNA virus, zika virus, and norovirus are assayed as interferences (negative samples) to examine the anti-interference effect and the selectivity of the developed TMB-NPs@PLGA-based immunoassay which is collated to the response of IV/A/H1N1. **Figure 5.2** shows the change in absorbance intensity of developed immunoassay to the mixture of negative samples and IV/A/H1N1. The intense color developed in the presence of IV/A/H1N1 in the samples, but not in the case of the negative samples containing interferences only. The interfering viruses are unrecognizable by the capturing and anti-HA antibodies on the conjugated TMB-NPs@PLGA, specific to IV/A. As a result, after washing, there is no TMB-NPs@PLGA in the reaction chamber, resulting in no TMB molecules even after the addition of DMSO, the only slight increase in the absorbance intensity in the detection of the negative samples justified the superior specificity of TMB-NPs@PLGA based colorimetric immunoassay towards IV/A detection.

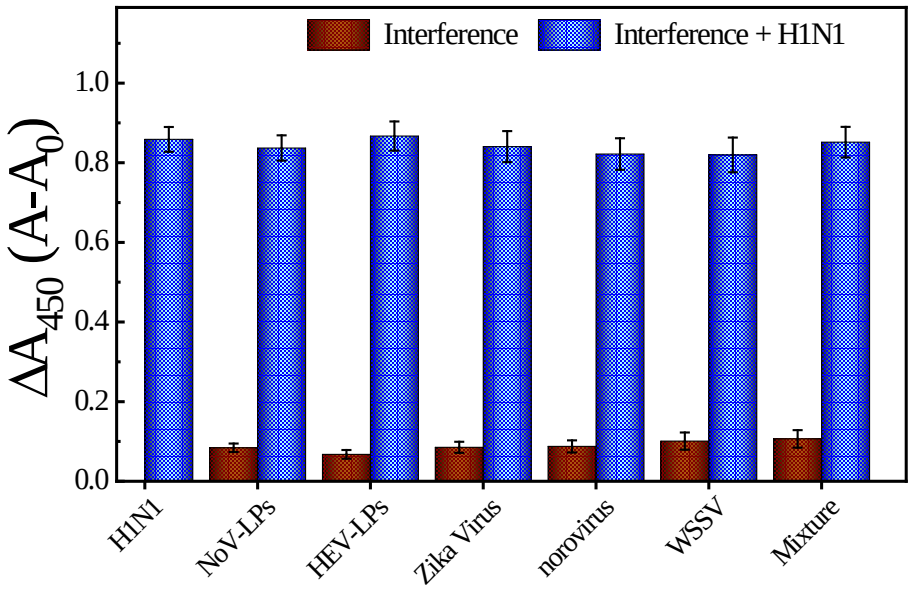

Figure 5.2 Interference study of the TMB-NPs@PLGA based immunoassay

5.3.1.3 Detection of clinical-isolated IV/A/H3N2 and S-protein of SARS-CoV-2

To demonstrate the practicability of the TMB-NPs@PLGA-based immunoassay, the clinically isolated samples containing IV/A/H3N2 are applied to the developed immunoassay (**Figure 5.3**). The absorbance intensity increased continuously proportionally to the increasing concentration of IV/A/H3N2 from 10^1–10^4 pfu /mL, developing the proportional gradient of color (Inset of **Figure 5.3**). The detection of the IV/A/H3N2 shows an R^2 of 0.985 with the LOD of 17 pfu /mL. The developed immunoassay using the TMB-NPs@PLGA nanovesicles proffers a higher sensitivity compared to the available commercial IV detection kit (Quicknavi-Flu 2, Denka Seiken Co., Ltd. Tokyo, Japan) and the conventional ELISA using HRP and gold nanoparticles (**Table 5.2**) (Ahmed et al. 2016a; Takemura et al. 2017). These results strongly demonstrate that our TMB-NPs@PLGA-based immunoassay possesses a strong anti-interference ability and is highly sensitive for practical use.

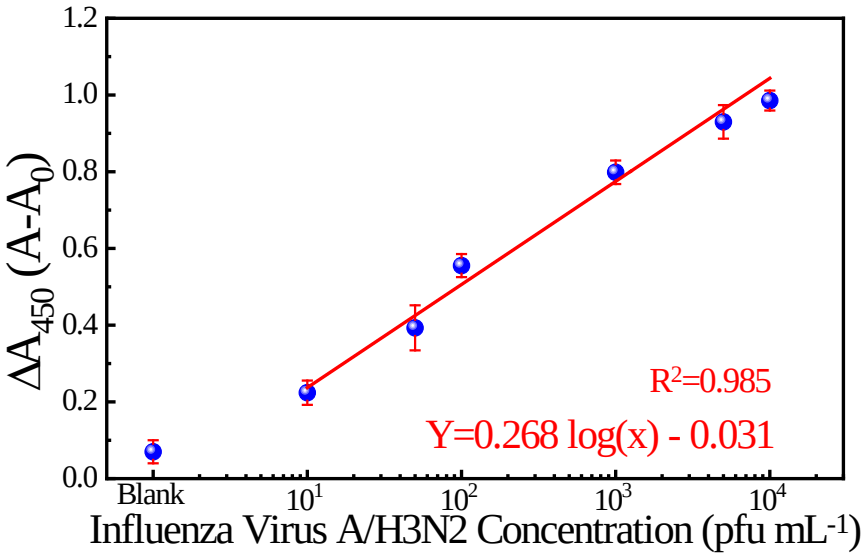

Figure 5.3 Clinically isolated Influenza Virus A/H3N2 (IV/A/H3N2) detection using TMB-NPs@PLGA based immunoassay

Table 5.2 Comparison of clinically isolated IV/A/H3N2 detection

	Virus Concentration (pfu/mL)						
Detection Method	5000	1000	100	50	25	10	1
Commercial IV detection kit	+	-	-	-	-	-	-
HRP-based ELISA	+	+	-	-	-	-	-
AuNPs-based Immunoassay	+	+	+	+	-	-	-
This study	+	+	+	+	+	+	-

In response to the recent outbreak of Covid-19, the TMB-NPs@PLGA-based immunoassay is applied to detect the spike protein of coronavirus. The spike protein is used as the antigen to demonstrate the direct coronavirus detection targeting the surface protein. As shown in **Figure 5.4**, the wide linearity from picogram to nanogram level is achieved with an excellent linear response depending on the concentration of the spike protein (R^2 = 0.992). The LOD is calculated down to 143 fg /mL, in which the femtogram level detection of the spike protein of coronavirus agrees with other biosensors with higher complexity fabrication and analysis (Mavrikou et al. 2020; Qiu et al. 2020; Seo et al. 2020).

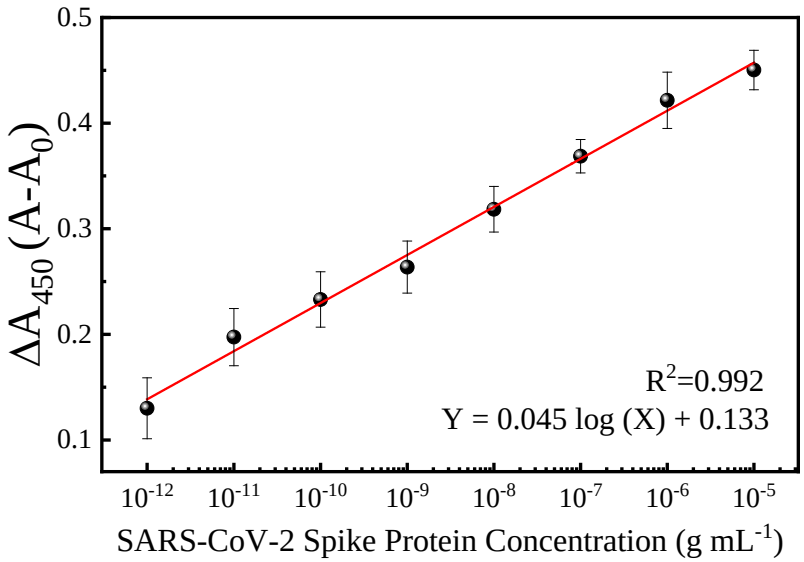

Figure 5.4 Spiked protein SARS-CoV-2 (S protein SARS-CoV-2) detection using TMB-NPs@PLGA based immunoassay

5.3.2 Dye@PLGA based immunoassay

5.3.2.1 Analytical Performance of the immunoassay for IV/A/H1N1 detection

Following the preliminary investigation on the proposed immunoassay, each polymeric nanocarrier is evaluated on the relevant subtype of the IV/A. IV/A/H1N1 and IV/A/H3N2 were detected using Ab-PP@PLGA and Ab-TP@PLGA, respectively. Positive detection results in pinkish hue with absorbance intensity at 560 nm and blue color with absorbance at 595 nm, suggests the existence of IV/A/H1N1 and IV/A/H3N2, respectively.

PP@PLGA-based IV/A/H1N1 biosensor, the absorbance spectra were obtained from the IV/A/H1N1 detection from 10^{0} – 10^{-6} fg /mL virus concentration. **Figure 5.5a** demonstrates that the absorbance at 560 nm increases as the IV/A/H1N1 concentration in the sample increases. The color created in the alkaline solution is pinkish, generating a gradient pattern from low to dark pink as the virus concentration increases. The absorbance at 560 nm (A_{560}) is plotted as a function of the IV/A/H1N1 concentration. The calibration line using A_{560} as the function of IV/A/H1N1 concentration is obtained with a correlation coefficient (R^2) of 0.953 and satisfactory linearity from 10^{1} – 10^{6} fg /mL (**Figure 5.5b)**. Furthermore, the limit of detection (LOD) is 27.56 fg/mL, which is calculated by using the equation $3\sigma/S$ (Ganganboina and Doong 2019) in which S and σ represent the slope function of the linear response and the lowest detectable signal, respectively.

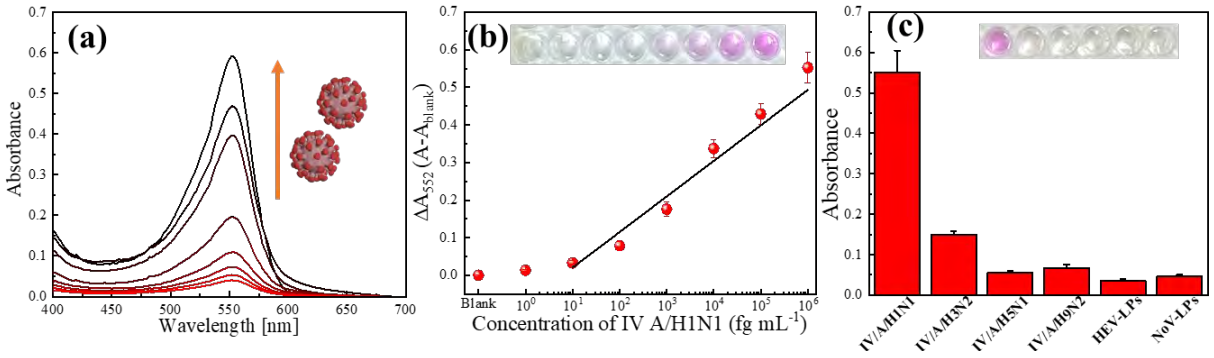

Figure 5.5 IV/A/H1N1 detection using PP@PLGA-based immunoassay (a) absorbance spectra of the detection, (b) the calibration curve (inset image indicated the visual color change of the detection), and (c) the selectivity assay

In specificity assay of the PP@PLGA-based biosensor, several subtypes of influenza virus, such as IV/A/H3N2, IV/A/H5N1, IV/A/H9N2 are assayed in the system, followed with several other recombinant proteins, such as HEV-like particles and NoV-like particles. As shown in **Figure 5.5c**, there is only signal from the biosensor to IV/A/H1N1 but neither to other subtypes because of the specificity coming from the antibodies of the Ab-PP@PLGA to surface protein of H1N1. The background noise is also observed in case of detection to the IV/A/H3N2 that may be consequently attributing from the binding affinity of Ab-MNPs to the major hemagglutinin of the IV/A. However, a slight signal is not adjudged to be a high signal of the IV/A/H1N1 detection signal.

5.3.2.2 Analytical Performance of the immunoassay for IV/A/H3N2 detection

In addition to detecting IV/A/H1N1, a TP@PLGA-based biosensor was used to detect IV/A/H3N2. The escalating absorbance signal at 595 nm as seen in **Figure 5.6a** was observed with respect to the exponential addition of the concentration of the IV/A/H3N2 virus with range of $10^0 – 10^6$ fg/mL. As shown in **Figure 5.6b**, a plot of absorbance value at 595 nm as y-axis of the function and the concentration of the IV/A/H3N2 in the sample as x-axis indicated a linear response of the biosensor. These expressed the function of the A_{595} in respect to the

exponential addition of IV/A/H3N2 in the sample in decent from 10^1 to 10^6 fg /mL with R^2 of 0.982 and calculated lower detection limit around 28.38 fg/mL. The selectivity of the developed TP@PLGA-based biosensor for IV/A/H3N2 detection was evaluated against different subtypes of IV/A and virus-like particles protein recombinants. The high difference between the absorbance value of the target and non-target promotes the excellent selectivity of the developed biosensor (**Figure 5.6c**), which is contributed by the specific binding of the antibodies-conjugated to TP@PLGA to the IV/A/H3N2.

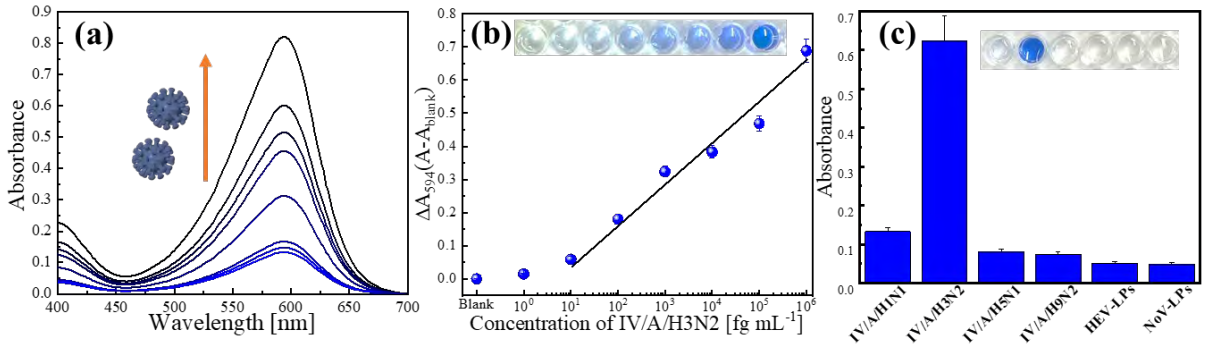

Figure 5.6 IV/A/H3N2 detection using PP@PLGA-based immunoassay (a) absorbance spectra of the detection, (b) the calibration curve (inset image indicated the visual color change of the detection), and (c) the selectivity assay

Several intrinsic points need to be highlighted owing to the superior performance of the Polymeric nanocarrier-based biosensor. (1) As opposed to protein-assisted nanoprecipitation (Xu et al. 2020b) the three-solvent system produces nanoparticles with a greater concentration of chromogens. The higher-loaded nanocarrier can increase the signal on an individual antibody-antigen binding up to the sub-femtogram level. (2) Because the polymeric border and the dye are both reactive to alkaline conditions, the color develops faster than in previous pH-sensitive biosensing systems. (Ren et al. 2018; Yan et al. 2019). (3) Because of its high surface area, magnetic separation in the biosensor may enrich the target analytes, generate a greater

number of immunosandwich structure, and shorten the incubation time for antibody-antigen conjugation. The entire assay took 15 minutes to complete, allowing for a quicker detection time than our previously established biosensor. (Khoris et al. 2021b).

5.3.2.3 Binary Detection as subtype Identification of Influenza Virus detection

The dye@PLGA-based biosensor is designed to outperform the existing immunoassay format in terms of detecting versatility. The existing biosensor is still aiming to accommodate the identification function of subtype viruses, despite its reliance entirely on measuring the substrate's catalytic response. The new biosensor uses chromogens-nanocarrier linked to antibodies specific to IV/A to provide binary colorimetric signals dependent on the viral subtypes in the target analyte.

Upon detecting the IV/A subtype, the absorbance of the mixture of dye@PLGA is measured to examine the composite responsiveness of dye@PLGA-based biosensor. As shown in **Figure 5.7a**, the composite absorbance spectra of mixture dye@PLGA, containing PP@PLGA and TP@PLGA were overlapping and complicated the analysis of the absorbance, . Those mixture in basic solution resulted to a dark bluish-purple in the reaction chamber. The absorbance spectra of the individual TP@PLGA, individual PP@PLGA and the mixture dye@PLGA were transformed into their 1st derivation absorbance spectra. The derivation absorbance emphasized the change of absorbance peaks as derivatives in respect to the interval of wavelength, which decomposed the complicated spectra into several inflection points. From those deconvoluted peaks, the similar peaks to the individual dye@PLGA was determined as the target signals (Shams Nateri and Ekrami 2008; Zhu et al. 2020b). **Figure 5.7b** displays the 1st derivation function of the composite absorbance of the dye@PLGA. There are visible derivative peaks that is the correlating to the individual dye@PLGA in the derivative spectra:

absorbance at 540 nm, 575 nm, and 630 nm. The absorbance of both dye@PLGA, however, is seen to be coexisting around absorbance of 540 nm.

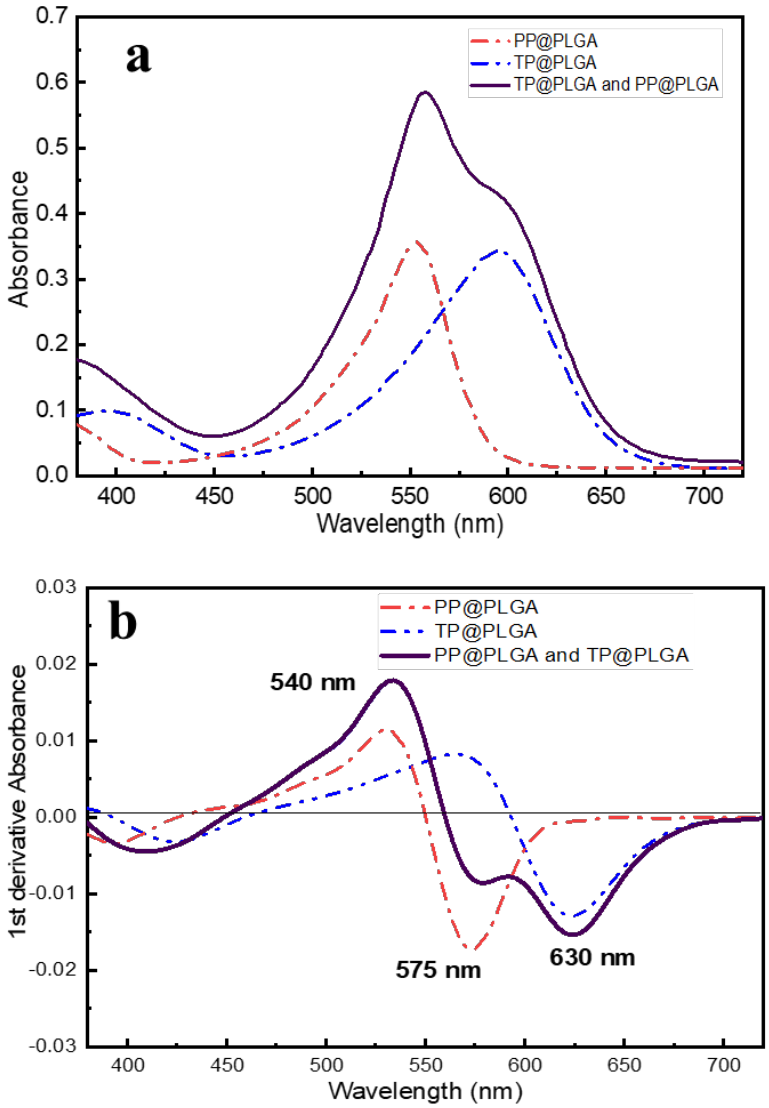

Figure 5.7 Binary response of PNLNs-based biosensor. (a) The absorbance spectra of PP@PNLNs, TP@PNLNs, and the PNLNs mixture. (b) The 1st derivation absorbance spectra of the PNLNs mixtures.

In the opposite side, the absorbance of TP@PLGA indicated a strong intensity absorbance around 630 nm. Moreover, PP@PLGA contributes to the absorbance value at 575 nm which is shifting the absorbance toward positive value and TP@PLGA to the other side.

The 1st derivation absorbance at 575 nm and 630 nm are selected to be the interest signal in the dye@PLGA-based biosensor because those signal is not overlapping together.

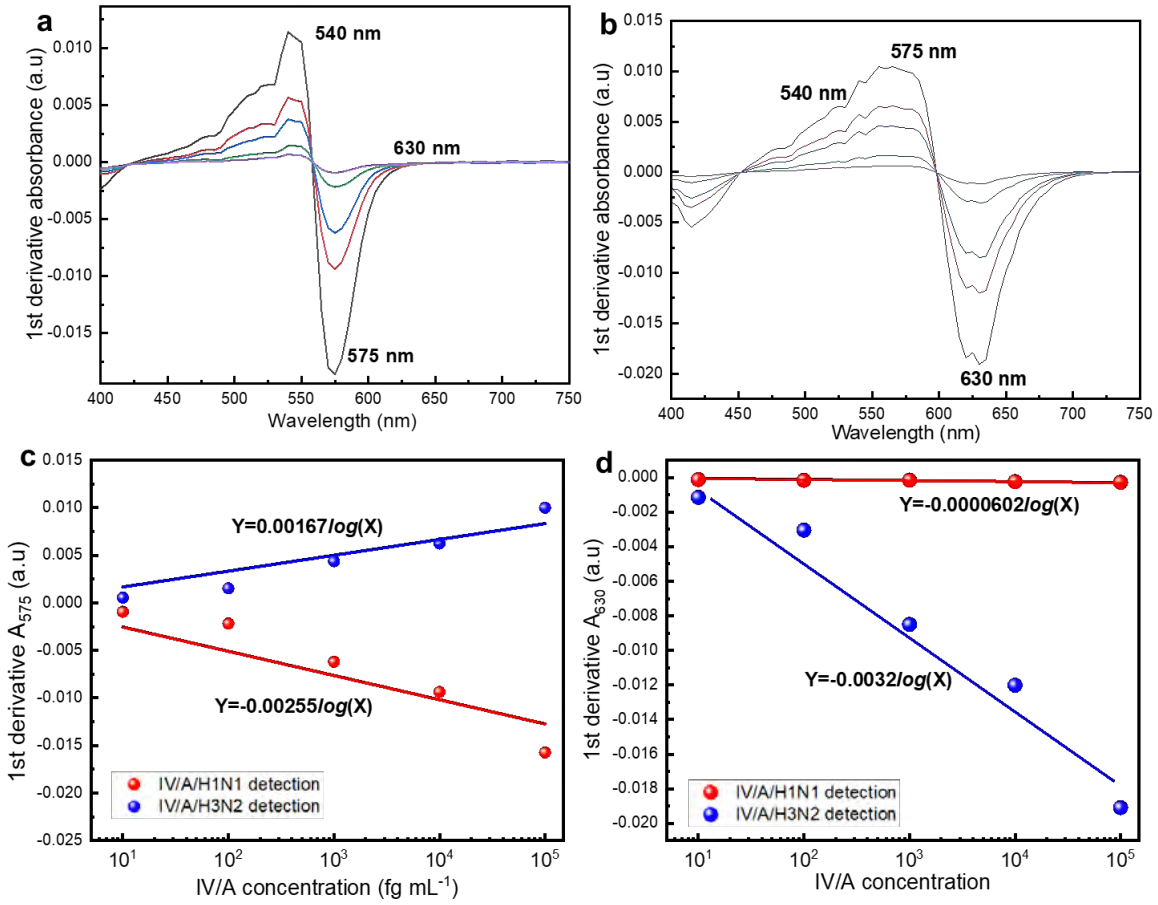

Figure 5.8 The contribution factor of PP@PNLNs and TP@PNLNs in the binary response of the developed biosensor. (a) 1st derivative absorbance of IV/A/H1N1 by PNLNs-based biosensor, (b) 1st derivative absorbance of IV/A/H3N2 detection by PNLs-based biosensor; (c) and (d) represent the 1st derivative absorbance peak of the IV/A/H1N1 and IV/A/H3N2 detections against the IV/A concentration to find the contribution factor of PP@PNLNs from IV/A/H1N1 and TP@PNLNs from IV/A/H3N2.

PP@PLGA and TP@PLGA were mixed together to the dye@PLGA-based biosensor to provide a simple one-pot identification purpose. The biosensor was done on detecting IV/A/H1N1 (**Figure 5.8a**) and IV/A/H3N2 (**Figure 5.8b**) from concentration of 10^1 fg/mL to 10^5 fg/mL. Each dye@PLGA contributed to the binary response and the inflection points of the derived absorbance at wavelength of 575 nm and 630 nm was plotted to the function of the

concentration of each IV/A/H1N1 and IV/A/H3N2, respectively. The slope obtained from th slope represents the own contribution factor (CF) of the PP@PLGA and TP@PLGA in the binary response systems of the dye@PLGA-based biosensor in the function of the concentration of the target viruses. **Figure 5.8c** displayed the signal absorbance pattern at 575 nm of the developed biosensor against the subtype of the IV/A as the absorbance is going negative in presence of IV/A/H1N1 and going positive in the presence of IV/A/H3N2. The CF of the PP@PLGA and TP@PLGA for absorbance at 575 nm is -2.55×10^{-3} and $+1.67 \times 10^{-3}$, respectively. As seen in **Figure 5.8d**, the plot presented the 1st derivate absorbance value at 630 nm alongside the concentration of the subtype IV/A as x-axis. It clearly unveils that the presence of IV/A/H1N1 resulted to a low signal than the signal coming from IV/A/H3N2 detection. It is as expected as PP@PLGA does not exhibit signal up to the absorbance region at 630 nm. As TP@PLGA solely contributes it, the CF of Polymeric nanocarrier at the 1st derivative absorbance at 630 nm is $+6.02 \times 10^{-5}$ for PP@PLGA and -3.20×10^{-3} for TP@PLGA. Hence, the overall equation of the binary response of the Polymeric nanocarrier-based biosensor can be expressed as

$$D^1_{575} = -2.55 \times 10^{-3} \log(C_{H1N1}) + 1.67 \times 10^{-3} \log(C_{H3N2}) \quad (1)$$

$$D^1_{630} = +6.02 \times 10^{-5} \log(C_{H1N1}) - 3.20 \times 10^{-3} \log(C_{H3N2}) \quad (2)$$

with binary response of Polymeric nanocarrier-based biosensor as D^1_{575} and D^1_{630} representing the 1st derivate absorbance at 575 nm and 630 nm, respectively; C_{H1N1} and C_{H3N2} represent the IV/A/H1N1 and IV/A/H3N2 concentrations, respectively.

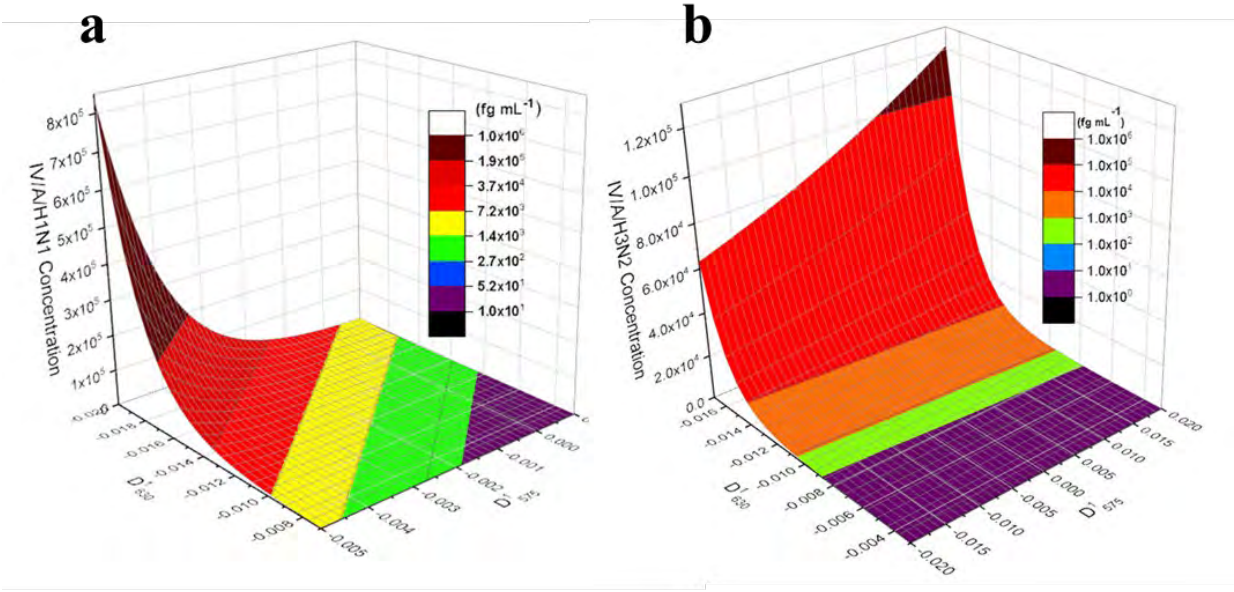

Figure 5.9 The simulated derivative binary response model determines IV/A/H1N1 concentration (c) and IV/A/H3N2 concentration (d).

Then, the equation (1) and (2) can be rearranged to isolate the variable representing the IV/A/H1N1 concentration and IV/A/H3N2 concentration on the left side and the rest of the variable to the right side. Hence, the concentration of the IV/A can be expressed as:

$$C_{H1N1} = 10^{\frac{-3.20 \times 10^{-3} D^1_{575} - 1.67 \times 10^{-3} D^1_{630}}{8.26 \times 10^{-6}}} \quad (3)$$

$$C_{H3N2} = 10^{\frac{6.02 \times 10^{-5} D^1_{575} + 2.55 \times 10^{-3} D^1_{630}}{8.26 \times 10^{-6}}} \quad (4)$$

Based on equations (3) and (4), the range of D^1_{575} and D^1_{630} are plotted in the matrix calculation to simulate the detected. IV/A/H1N1 concentration. **Figure 5.9a** shows the pattern of the IV/A/H1N1 concentration at the limit range from –0.005 to +0.001 for D^1_{575} and –0.007 to –0.02 for D^1_{630}. The concentration obtained has a range with a minimum of 10^0 fg /mL and a maximum value of 10^6 fg /mL. The pattern indicates that the maximal concentration of IV/A/H1N1 is toward the $-D^1_{575}$ and $-D^1_{630}$. On the other side, **Figure 5.9b** shows the plot of the IV/A/H3N2 as the function of D^1_{575} and D^1_{630}. The range of the D^1_{575} and D^1_{630} are

determined from –0.02 to +0.02 and –0.004 to –0.016, respectively. The pattern demonstrates that the shifting value of D^1_{630} could determine the range of the IV/A/H3N2 concentration as the window of the concentration scale upon the D^1_{575} is wider than the window scale of D^1_{630}. Overall, the derivative binary response of the biosensor can be utilized to determine the concentration of the IV/A/H1N1 and IV/A/H3N2 based on the coefficient factors of PP@PLGA and TP@PLGA as the parameters.

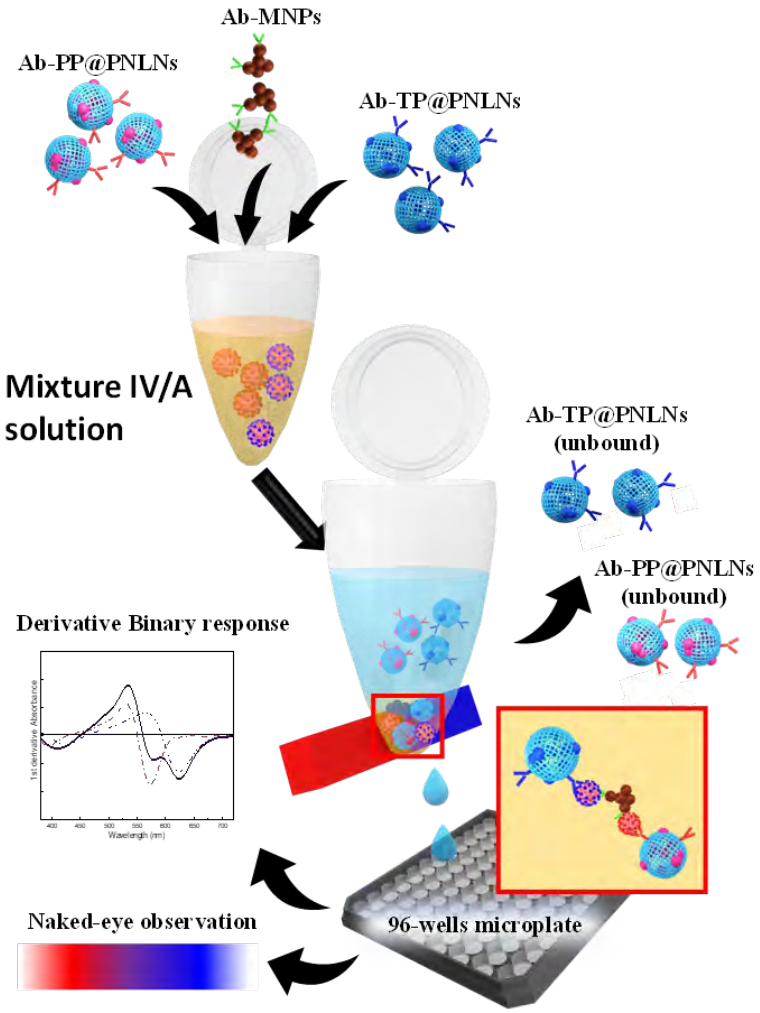

Figure 5.10 Schematic illustration of binary IV subtype detection

The schematic illustration of the dye@PLGA-based biosensor is displayed in **Figure 5.10** which indicated a condition of the presence of IV/A subtypes mixed in the sample solution. When a series of IV/A/H3N2 concentration from 10^1–10^4 fg /mL was mixed to 10^5 fg /mL IV/A/H1N1 it was defined as "Mixture set A". On the other hand, when a series of IV/A/H1N1 concentration from 10^1–10^4 fg /mL was mixed to 10^5 fg /mL IV/A/H3N2 it was defined as "Mixture set B". As shown in **Figure 5.11a**, the dye@PLGA-based biosensor was assayed using mixture set A as the detection sample. The absorbance shows a sole peak at 575 nm in a negative value of $– 1.2 \times 10^{–3}$attributing to the presence of IV/A/H1N1 in the solution. Along the gradual change of the concentration of the f IV/A/H3N2, the peak absorbance at 575 nm is gradually decreasing in respect to the increasing concentration of the IV/A/H3N2, and absorbance at 630 responsively intensifies as the increasing concentration of the IV/A/H3N2. Similarly, **Figure 5.11b** displayed the performance of dye@PLGA-based biosensor in assessment to the mixture set B. The obtained derivative absorbance at 575 nm and 630 nm in the presence of each IV/A/H3N2 in mixture set B. are $5.98 \times 10^{–3}$ and $– 1.38 \times 10^{–2}$, respectively. The progressive shift in the positive value to of the 1st derivative absorbance at 575 nm correlates to a larger concentration of IV/A/H1N1 in mixture set B.

The binary response equations (1) and (2) of the constructed biosensor were utilized to determine the detected concentrations of IV/A/H1N1, and IV/A/H3N2 in Mixture sets A and Mixture sets B based on the derivative absorbance spectra to assess the binary detection performance of the dye@PLGA-based biosensor. Then, the plot aims to analyze the binary response signal as displayed in **Figure 5.12**. **Figures 5.12a** displays the assessment of dye@PLGA-based biosensor to the Mixture set A and **Figures 5.12b** displays the assessment of dye@PLGA-based biosensor to the Mixture set B. It was obtained that IV/A/H1N1 in Mixture set A is around $(1.58 \pm 0.33) \times 10^5$ fg /mL IV/A/H1N1 concentration with linear function in respect to the concentration of the IV/A/H3N2 in the Mixture set A starting from

10^1 to 10^4 fg /mL with R^2 of 0.955. Next, the developed dye@PLGA-based estimated that IV/A/H3N2 in Mixture set B is around (7.23±1.27) × 10^4 fg /mL IV/A/H3N2 concentration with linear function in respect to the concentration of the IV/A/H3N2 in the Mixture set B starting from 10^1 to 10^4 fg /mL with R^2 of 0.963 and a variance coefficient of around 25.8%. Overall, the biosensor exhibits binary signal in a single detection which could target subtype IV/A subtype in the simultenous readout with a background cut-off down to 13.9 fg /mL based on the blank sample detection. Moreover, looking at the slope function of the signal-vs-concentration of the detected virus concentration, there is an overestimation of 18.6% of IV/A/H1N1 detection than the determined IV/A/H1N1 concentration from ELISA which we considered as the comparative data. and underestimation down to 15.1% for IV/A/H3N2 detection from the ELISA data.

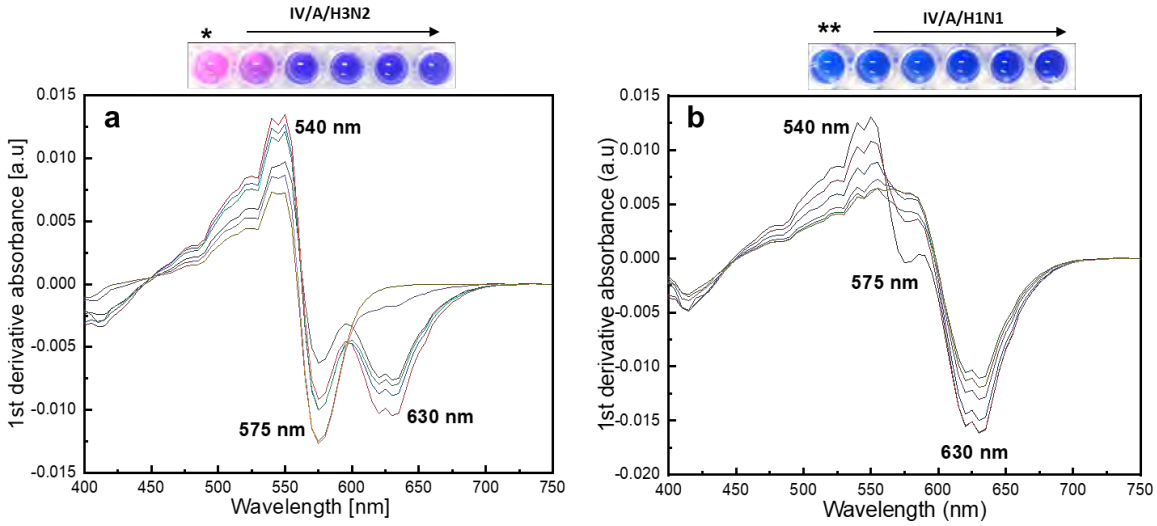

Figure 5.11 The 1st derivative absorbance spectra of multiplex detection on the IV/A by PNLNs-based biosensor. (a) mixture set A and (b) mixture set B. The digital image shows the color developed taken by a smartphone camera (* indicates the detection of only IV/A/H1N1 and ** indicates the detection of only IV/A/H3N2). Both serve as the positive control in the binary detection).

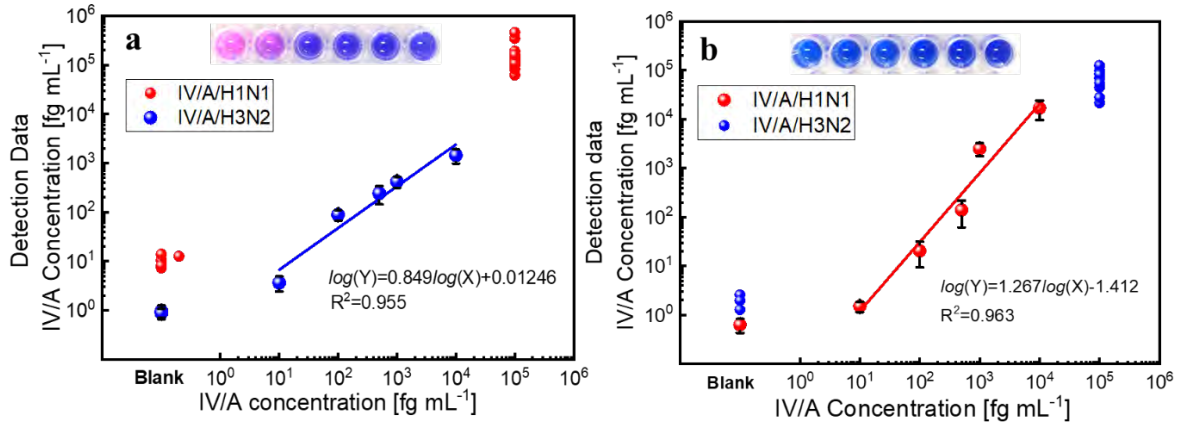

Figure 5.12 The binary detection of IV/A/H1N1 and IV/A/H3N2 in mixture IV/A solution by dye@PLGAs-based biosensor. (a) represent the detected concentration of IV/A/H1N1 (red circle) and IV/A/H3N2 (blue circle) in the Mixture set A; (b) represent the detected concentration of IV/A/H3N2 (blue circle) and IV/A/H1N1 (red circle) in the Mixture set B. Mixture set A contains a fixed concentration of 10^5 fg /mL IV/A/H1N1 and a series concentration of IV/A/H3N2 from 10^1–10^4 fg /mL (0, 10, 100, 500, 1000, 10000 fg /mL); Mixture set B contains a fixed concentration of 10^5 fg /mL IV/A/H3N2 and a series concentration of IV/A/H1N1 from 10^1–10^4 fg /mL (0, 10, 100, 500, 1000, 10000 fg /mL). The digital image shows the color developed taken by a smartphone camera.

Next, the evaluation on the performance of the dye@PLGA-based biosensor for subtype detection of IV/A was performed in the human serum. As shown in **Table 5.3**, the detection shows 86.1 – 124.8% recovery is concentrated in 10% human serum and 93.5 – 110.67% recovery in diluted 2% human serum. Because of the Ab-MNPs and the magnetic separation, matrix solutions such as human serum have the minimum effect on detecting the influenza virus by the developed biosensor. The major factor drawback of the dye@PLGA-based biosensor is probably attributed to the ratio binding to the IV/A/H3N2 and IV/A/H1N1 in order to make immuno-sandwich structure during the magnetic separation step and the difference in the deprotonation of the both chromogens.

Table 5.3 The recovery test of the multiplex detection of IV/A/H1N1 and IV/A/H3N2 in human serum using PNLNs-based biosensor

Sample No.[2]	Added IV/A concentration (fg /mL)[1]		Detected IV/A concentration (fg /mL)			
	IV/A/H1N1	IV/A/H3N2	IV/A/H1N1	Recovery (%)	IV/A/H3N2	Recovery (%)
1	1000	1000	1236.7	123.7	1257.1	125.7
2	500	500	541.3	108.3	645.6	128.2
3	200	200	172.3	86.2	169.4	84.7
4	1000	1000	1141.3	114.1	1105.8	110.7
5	500	500	619.5	103.9	582/9	116.6
6	200	200	221.1	110.5	187.9	93.8

[1]The subtypes of the IV/A concentration were equivalent in the sample.
[2]Sample 1,2 and 3 contain 10% human serum, and Samples 4,5 and 6 contain 2% human serum

The composite responses consisting of TP@PLGA and PP@PLGA in the developed biosensor demonstrated a feasible analysis for subtype detection of the IV/A. In the one-pot format along the magnetic separation to the detection step, the developed biosensor envoys the simplicity and practical in the dual-targeting virus detection, which does not require complex platform fabrication (Yao et al. 2020) nor complex signal analysis (Pang et al. 2020; Wu et al. 2019). Further, compared to the presently developed biosensor (**Table 5.4**) (Achadu et al. 2020; Han et al. 2016; Khoris et al. 2021b; Kushwaha et al. 2019; Lee et al. 2018; Lin et al. 2017; Oh et al. 2018; Takemura et al. 2021), the developed biosensor using dye@maintains a low detection limit down to sub-femtogram level even with additional response to a simultaneous binary IV/A subtype detection. However, it has to be said that the developed binary response biosensor could not guarantee a higher degree of signal amplification in term of challenging the bottleneck of single virus detection. Nevertheless, it can enrich the information within the virus detection platform. Several factors impede the further scale of this biosensor. The limited

variety of the chromogen in a similar range of stimuli and the physicochemical properties, such as solubility and colloidal stability. Further studies with multiple polymers are recommended to show the performance of the polymeric nanocarrier in the biosensor.

Table 5.4 The comparison of the present biosensor technique for IV/A detection

Detection Technique	Nanomaterial	Target IV/A	Detection range (g mL^{-1})	Detection limit (LOD, g mL^{-1})
Colorimetric	PP@PNLNs	H1N1	10^{-15} –10^{-9}	2.76×10^{-14}
	TP@PNLNs	H3N2	10^{-15} –10^{-9}	2.84×10^{-14}
Colorimetric	HRP@Liposome	H5N1	10^{-10} – 10^{-8}	4.00×10^{-11}
Colorimetric	TMB-NPs@PLGA	H1N1	10^{-15} –10^{-9}	3.24×10^{-14}
Fluorescent	AuNP/CdSe QDs/Fe_3O_4/graphene	H1N1	10^{-13} –10^{-9}	6.07×10^{-12}
Fluorescent	gCNQDs/Fe_3O_4 - MoO_3 QDs	H1N1	10^{-12} –10^{-7}	9.00×10^{-13}
Volumetric assay	MWCNT-IDE	H1N1	10^{-14} –10^{-10}	1.00×10^{-14}
Colorimetric	(+)AuNZ/MNPs	H1N1	10^{-15} – 10^{-7}	1.00×10^{-14}
Fluorescent and Electrochemical DPV	AuNP-MNP-CNT	H1N1	10^{-15} – 10^{-6}	9.05×10^{-15}
Electrochemical - Amperometry	ZnO nanorod/multichannel electrode	H1N1 H5N1	10^{-12} – 10^{-7}	1.00×10^{-12}

5.3.3 PtNPs@Co_3O_4 based immunoassay

5.3.3.1 Analytical Performance of the immunoassay

Based on the optimization of the Pt embodiment, Ab_{NoV}-$PtNPs_3$@Co_3O_4 NCs were further employed in the NoV-LPs detection to determine the correlation of the target concentration to

the response of the immunoassay. After Ab_{NoV}-PtNPs@Co_3O_4 NCs were prepared, the PtNPs@Co_3O_4-based immunoassay was employed, from the capturing Ab immobilization, blocking, sample introduction, and the detection using nanozyme activity. The sensitivity of this sensing system was evaluated by monitoring the change of sample detection signal from the blank signal ($A_{sample} - A_{blank}$) as a function of the concentration of NoV-LPs. A sigmoid response was obtained as a function of the concentration of NoV-LPs with a correlation coefficient (R^2) of 0.991 (**Figure 5.13**). In addition, the calculated limit of detection (LOD) was approximately 3.322 fg/mL based on the slope of the linear response and the standard error of the blank (Khoris et al. 2021a) with linearity from $10^1 - 10^7$ fg/mL

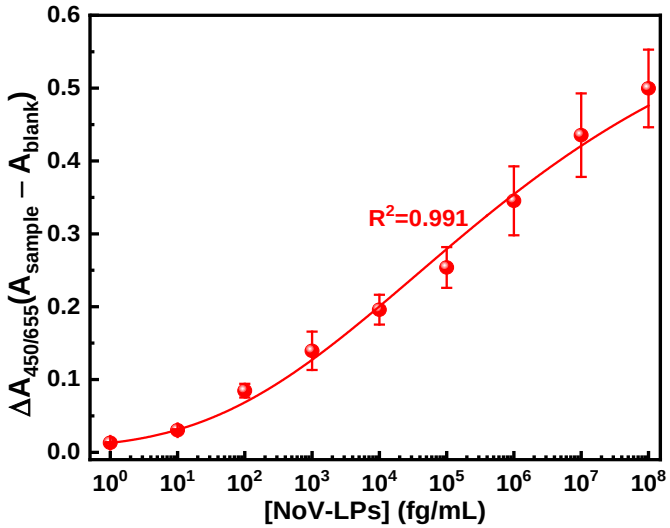

Figure 5.13 NoV-LPs detection using PtNPs@Co_3O_4 NCs-based immunoassay

5.3.3.2 Specificity assay

The selectivity of this sensing system was assessed with several biological agents such as influenza virus, recombinant Hepatitis E virus-like particles (HEV-LPs), recombinant Non-Structural 1 protein (NS1), and BSA. As shown in **Figure 5.14**, only the wells containing 1 ng/mL NoV-LPs showed a higher absorbance with the value of 0.6. Other wells were introduced with non-target proteins or viruses with average absorbance of around 0.15. This

result demonstrated that Ab_{NoV}-PtNPs@Co_3O_4 did not bind to other viruses or proteins due to the specificity of the antibodies and blocking process.

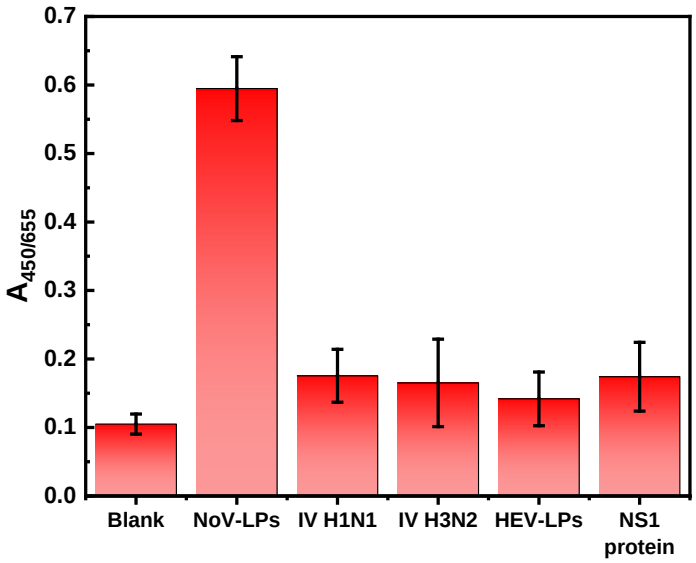

Figure 5.14 Selectivity assay of PtNPs@Co_3O_4 NCs-based immunoassay

5.3.3.3 Detection of clinical-isolated IV/A/H3N2 and S-protein of SARS-CoV-2

To demonstrate the practicability of the PtNPs@Co_3O_4-based immunoassay, clinically isolated stool samples containing NoV are applied to the developed immunoassay (**Figure 5.15**). The absorbance intensity increased continuously proportionally to the increasing concentration of NoV GII.4 (in copies/mL) from 10^1–10^6 copies/mL, developing a linear response between the signal absorbance and the concentration of NoV in the stool sample. The detection of the NoV shows linear calibration with an R^2 value of 0.986, and the LOD was calculated at around 33.53 copies/mL, which is equivalent to 335.3 copies of viral RNA/g feces. The developed immunoassay was compared to the commercial NoV detection kit (Denka Seiken Co., Ltd, Tokyo, Japan), in which the signal was inferior in the low concentration range of NoV.

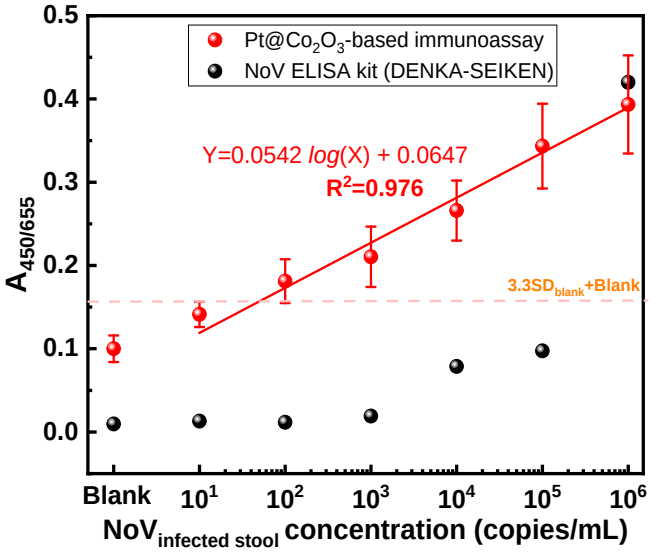

Figure 5.15 Clinically isolated fecal NoV detection using PtNPs@Co_3O_4 NCs-based immunoassay

In addition to the NoV detection, by substituting the corresponding antibodies from Ab_{NoV} into $Ab_{SARS\text{-}CoV\text{-}2}$ targeting S (Spike) protein or N (Nucleocapsid) protein of SARS-CoV-2, the developed $Ab_{SARS\text{-}CoV\text{-}2}$-PtNPs@$Co_3O_4$-based immunoassay demonstrated a good response of SARS-CoV-2 protein biomarker in complex media such as cell lysate (**Figure 5.16**). Detection limits for S protein and N protein were 148.28 and 124.85 fg/mL with a linear response with an R^2 value of 0.988 and 0.981, respectively. The obtained linear range is 10^1 – 10^7 fg/mL for both biomarkers. The immunoassay could demonstrate concentration-dependent detection of various viruses' proteins by substituting the recognition antibodies. The linear responses are considered reliable, with a high R^2 value >0.98 compared to the reported work of SARS-CoV-2 detection in a complex biological sample (de Lima et al. 2021). These results strongly showcased how the developed nanozyme-based immunoassay possesses a reliable detection for the target viruses and their biomarker protein and is superior in the detection limit due to the enhanced nanozyme activity in the immunoassay.

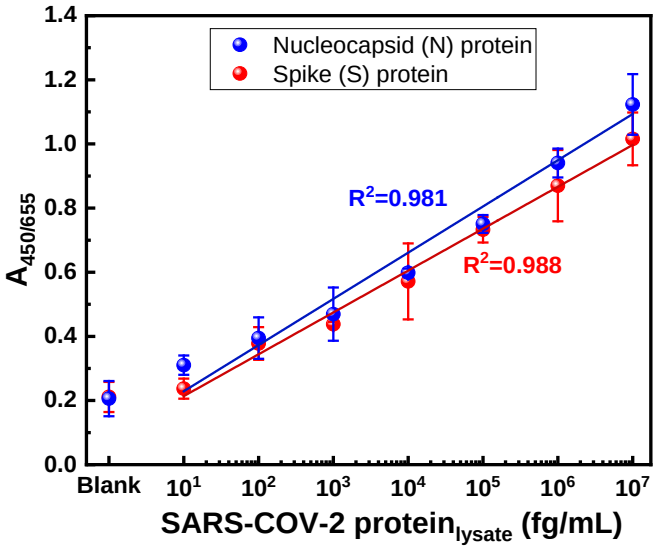

Figure 5.16 SARS-CoV-2 protein detection using PtNPs@Co_3O_4 NCs-based immunoassay

4. Conclusions

The main purpose of this section was to show the practical features of developed immunoassays. The signal amplification was showcased from the two-step-signal enriched TMB-NPs@PLGA based immunoassay, followed by magnetic binary responsive dye@PLGA based immunoassay and enhanced PtNPs@Co_3O_4 NCs based immunoassay. The detection was focused on the Influenza Virus type A (IV/A), subtype species of the IV/A, spike protein (S) and nucleocapsid protein (N) of SARS-CoV-2 proteins, and fecal NoV from human and clinically isolated human influenza virus. To show the performance of the immunoassay platform, several types of proteins, interferences, and other viruses were assayed to the immunoassays. All platforms were selectively showing signals only to the respective specific target because of the specific conjugated antibodies at capturing probes and detecting nanoprobes. Last but least, all platforms are based on colorimetric, which means the signal was based on change of signal molecules and produced visible color in the detection of the presence of the target viruses.

Chapter 6

Signal Amplified Virus Detection in Electrochemical System

Chapter 6. Signal Amplified Virus Detection in Electrochemical System

6.1 Introduction

6.1.1 Mosquito-borne Infectious Disease

In the developing countries, especially in tropical region, dengue virus (DENV) infection has been becoming a huge health risk and burden worldwide (Yanagisawa et al. 2018). This tropical disease is predicted to expand to sub-tropical and further from the equator region and threaten continually more lives due to urban movement, rising temperature and climate crisis (Colón-González et al. 2021). Henceforward, tropical infectious diseases should have been an anticipated threat globally (Kabir et al. 2021). Currently, the available methods used for detecting DENV rely on cell culture (Iswardy et al. 2017), PCR (Abraham et al. 2021) and ELISA assays (Vázquez-Guardado et al. 2021). These conventional diagnosis methods are shown to be resource-demanding in term of establishment and operation which are not likely suitable in poor environment and scarcity setting (Eivazzadeh-Keihan et al. 2019). Moreover, DENV is known for its low dose infection and availability during its earlier infection stage, which is considered a good model in countering the bottleneck of early detection (Lai et al. 2019), (Parkash et al. 2021). For early stage detection based on its cycle and available biomarker, the non-structural protein 1 (NS1) protein of DENV (DENV-NS1) can be suitable diagnosis target due to its early presence in the DENV infection (Dhal et al. 2020; Wasik et al. 2018), (Suthanthiraraj and Sen 2019).

6.1.2 Aptamer biosensor (Aptasensor)

Aptamer-based biosensor (Aptasensor) is explored intensively in biomedical field, pollutant analysis and chemical sensor (Liu et al. 2019; Zhang et al. 2021; Zhang et al. 2018). Aptamer is a single-stranded oligonucleotide which is capable to bind specifically to

corresponding target with good structural stability and sufficient affinity. It is known for moiety functionality, chemical stability, and cost-favorable with low batch variation (Nguyen et al. 2022). Aptasensor have been developed in several analytical methods using nanozyme (Weerathunge et al. 2019), plasmonic nanomaterial (Xu et al. 2020a), and magnetic nanoparticles (Xu et al. 2020a). On the other side, aptasensor has recently been dominating by analytical electrochemical due to its high signal-to-noise transducing mechanism (Idili et al. 2021; Sheibani et al. 2021). Unfortunately, the developed methods may suffer from limited method of assay design and modulation to establish a reliable detection (Ganganboina et al. 2020a; Takemura et al. 2021).

6.1.1 Signal Amplification in Electrochemical System

In the previous work, the utilization of liposomal nanoencapsulation to bring signal transducer into the detection platform enhanced the electrochemical detection signals (Ganganboina et al. 2020c; Nasrin et al. 2020). However, such a solution necessitated encapsulation homogeneity as well as a lengthy interim phase to release and activate the sensing probes during the detection protocol. Signal enrichment concepts, on the other hand, have opened up a new technique for generating higher positive signals to baseline, as well as meeting the urgent demand for a wider dynamic range of detection with more complementary information. (Khoris et al. 2021a; Zhang et al. 2021). However, unlike the existing signal amplification method, the system was in bulk solution. Unlike others, electrochemical detection depended on the interfacial electrochemical reaction and electron transfer. As a result of the requirement to convert such a technology from bulk to interface, signal enrichment suited for electrochemical detection must be adapted, and existing aptasensors must be tuned to a higher level of dependability.

A versatile and simple aptamer conjugation has been performed on gold nanoparticles (AuNPs) (Gupta et al. 2021). A more functional and dependable platform with a combination feature, very sensitive detection from an electrochemical signal, and a practical sensing probe fabrication was developed using an electrochemical aptaensor. Combining the two principles resulted in a signal enrichment and sense-antisense competitive hybridization technique. The aptasensor was created and developed to have a competitive electrochemical detection of DENV-NS1, with the goal of detecting DENV infection early and with high sensitivity. Unlike a single AuNPs-Apt (Morya et al. 2020), the complementary AuNPs-Apt induced a 3D-nanoassembly structure of AuNPs, resulting in a larger level of self-assembled layers on the electrode. Unlike with the conventional electrochemical aptasensor (Wang and Zhao 2020), this study took full advantage of a greater quantity of methylene blue chelation by inserting methylene blue (MB) in the 3D-nanoassembly structure via MB-duplex aptamer interaction (Wang and Zhao 2020). The electrochemical signal from MB proved that it could enhance the detection signal down from picogram to femtogram level. Excitingly, the created aptasensor provides a greater tool for efficient, straightforward, and label-free DENV-NS1 detection, which has significant potential as an early-diagnostic biosensor to target infectious viruses at low concentrations in the early stages of illness.

6.2 Materials and Methods

6.2.1 Materials

Two kinds of gold nanoparticles (AuNPs) (5 nm and 20 nm) were obtained from Sigma-Aldrich (St. Louis, MO, USA). Disposable gold electrode (DGE) was purchased from Metrohm Dropsens (C220-BT, Herisau, Switzerland). Streptavidin was obtained from Wako Pure Chemical (Tokyo, Japan). Anti-dengue type 2 NS1 protein aptamer (Apt_1) (Sequence name:

ATW0005-BY5-100) and its complementary aptamer (Apt_2) were purchased from Pair Biotechnologies, Inc. (TX, USA). Apt_1 and Apt_2 have a length of 32 nucleotides and 14 nucleotides, respectively. Apt_2 was custom ordered with 3 mismatches evenly spaced over the 14 base lengths.

Influenza virus A and its subtypes were obtained from ProSpec-Tany Technogene, Ltd. (East Brunswick, NJ, USA). Recombinant dengue virus 2 NS1 protein (ab181966) was purchased from Abcam (Cambridge, UK), and 293T whole cell lysate was obtained from Genetex (CA, USA). According to our previous work, norovirus-like particles (NoV-LPs) were prepared from a silkworm expression system (Boonyakida et al. 2022). All experiments were conducted using deionized (DI) and autoclaved water.

6.2.2 Instruments

The absorbance was measured using a clear transparent cuvette (l = 10 mm) by UV-vis spectrophotometer (Shimadzu, Kyoto, Japan) and by using a transparent 96-wells microplate reader (INFINITE 200 M Plex, TECAN, Kanagawa, Japan). Transmission electron microscopy (TEM) images were generated using TEM (JEM-2100F, JEOL, Ltd., Tokyo, Japan) operated at 100 kV. The electrochemical measurement was conducted using Bio-Logic SP-200 Potentiostat and EC-Lab V11.02 software (Bio-Logic Sci. Instruments, Seyssinet-Pariset, France).

6.2.3 Preparation of Apt_1- and Apt_2-conjugated AuNPs

The conjugation of the aptamers to AuNPs is based on the general streptavidin-biotin binding (Hu et al. 2014) for anti-dengue type 2 NS1 protein aptamer (Apt_1) forming AuNPs-Apt_1. Initially, 2 mL of AuNPs (0.5 a.u) was mixed with 50 µL streptavidin solution (1 mg/mL)

and was incubated for 2 h. Then, the solution containing non-conjugated streptavidin was removed. AuNPs-streptavidin was redispersed in phosphate-buffered saline (PBS) buffer containing 1 mM $MgCl_2$. Apt_1 with biotin on its 5'-end was prior resuspended and refolded according to the instructed protocol from the provider. After refolding, 5 µM of Apt_1 was added to the AuNPs-streptavidin and incubated for 2 h at room temperature. Afterward, the AuNPs-Apt_1 solution was centrifuged to remove excess aptamer. The Apt_1-conjugated AuNPs (AuNPs-Apt_1) were redispersed in PBS buffer containing 1 mM $MgCl_2$.

The conjugation of AuNPs-Apt_2 uses a thiol-Au affinity reaction with Apt_2 aptamer having a thiol-group at its 5'-end (Giorgi-Coll et al. 2020). The conjugation was simply done by mixing AuNPs (2 mL, 0.5 a.u) and the Apt_1's complementary aptamer (Apt_2) (5 µM) and was incubated for 2 h at room temperature. Afterward, AuNPs-Apt_2 was redispersed in PBS buffer containing 1 mM $MgCl_2$. According to the provider's protocol, the Apt_2 was priorly resuspended, refolded, and reduced.

6.2.4 DENV-NS1 binding confirmation to Aptamer-conjugates

The production of the DENV-NS1 target sample included a series of dilutions. DENV-NS1 was then mixed with PBS buffer containing $MgCl_2$ (1:1 v/v) and added to 100 µL of AuNPs-Apt_1. The aptamer was allowed to bind to the DENV-NS1 by incubating the mixed solution at room temperature. Because of the small number of DENV-NS1 binding site to the aptamer, the visual color and plasmonic shift of the AuNPs were slightly limited. The mixture was then introduced to a 50 µL AuNPs-Apt_2 solution as complimentary probes into the AuNPs-Apt_1 solution to further induce aggregation. Apt_2 was bound to Apt_1 of the AuNPs-Apt_1 which was not bound to DENV-NS1 after the combination was incubated.

6.2.5 Detection of dengue virus 2 NS1 protein in buffer and spike solution

An Apt_2-modified disposable gold electrode (DGE) was used for the electrochemical detection. Apt_2-modified DGE was prepared by incubating 10 µL of 1 µM thiol-functionalized Apt_2. The AuNPs-Apt complex solution was supplemented with a 10 mM methylene blue (MB) solution (1:1 v/v) to convert the aptasensor into an electrochemical detector. The mixture was dropped onto the Apt_2-modified DGE. The solution was then discarded, and the electrode was repeatedly washed in PBS buffer containing 1 mM $MgCl_2$. PBS buffer with an extra 0.5 M NaCl is used as the working solution during the electrochemical run. The differential pulse voltammetry (DPV) study was performed at a step potential of 25 mV/s and modulation pulse and time of 50 mV and 50 ms, respectively, from –0.5 V to +0.2 V. The electrochemical signal was analyzed based on the DPV's oxidation profile.

6.3 Results and Discussions

6.3.1 Mechanism of the 3D-nanoassembled gold nanoparticles aptasensor

The reported aptasensor is constituted of aptamer-conjugated AuNPs which form a competitive binding of AuNPs-Apt_1 to DENV-NS_1 and a complementary binding of AuNPs-Apt2 to AuNPs-Apt2. As shown in **Figure 6.1**, the sensing mechanism was built in two contexts: colorimetric detection to confirm the competitive binding and electrochemical for enhanced detection. First, AuNPs-Apt_1 and DENV-NS1 solution were mixed and incubated for binding time via the affinity of the aptamer-DENV-NS1 (a). As they attached, AuNPs-Apt_1/DENV-NS1 was formed (b). Then, a complementary AuNPs-Apt_2 was added into the mixture (c) to match the unoccupied Apt_1 of AuNPs-Apt_1, generating a 3D-nanoassembled aggregation (AuNPs-Apt complex) via Apt_1-Apt_2 hybridization (d).

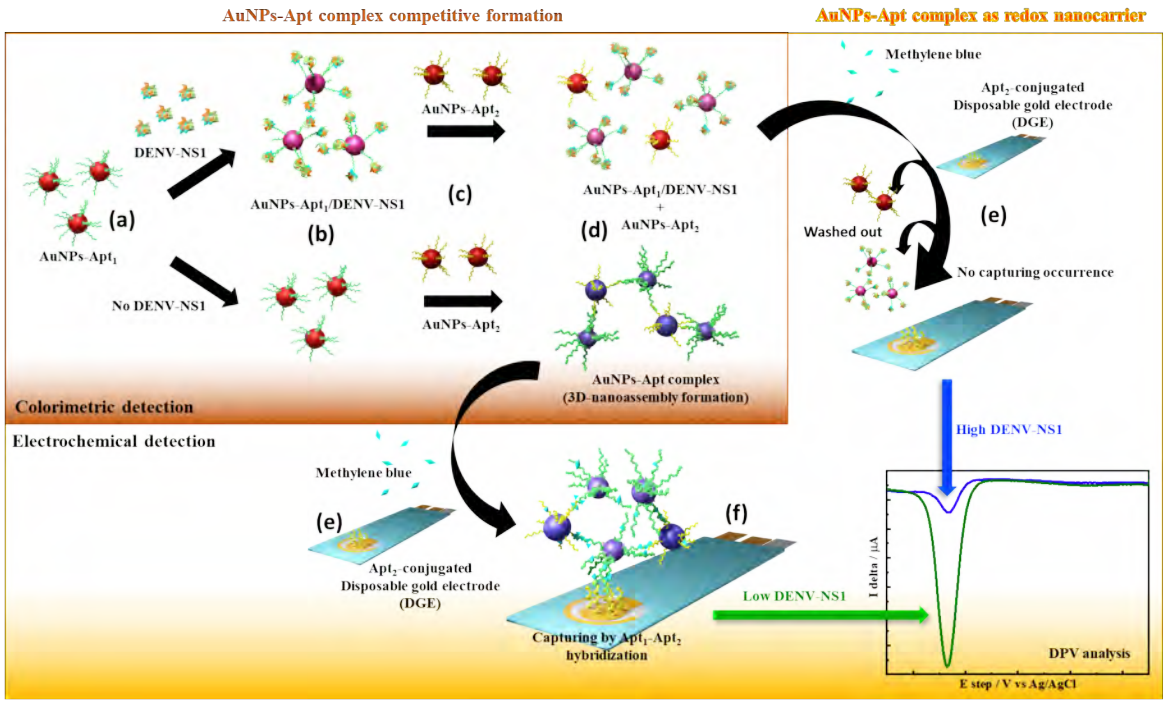

Figure 6.1 Proposed 3D-nanoassembled gold nanoparticles-based aptasensor designed for colorimetric and electrochemical detections. **(a)** and **(c)** indicate AuNPs-Apt_1 and AuNPs-Apt_2 as the detection probes; **(b)** shows DENV-NS1 binding to AuNPs-Apt_1 and **(d)** shows 3D-nanoassembly of AuNPs; **(e)** indicates electrochemical detection step and **(f)** shows the 3D-nanoassembled AuNPs captured on the Apt_2-modified DGE.

Methylene blue (MB), a redox active molecules, adapted to the system to capable the existing 3D-nanoassembled AuNPs-Apt for electrochemical detection (**e**) and electrostatically intercalated to the duplex structure of the AuNPs-Apt complex (Farjami et al. 2010). The captured DGE/Apt_2/AuNPs-Apt_1(AuNPs-Apt_2) was formed when the duplex structure of Apt_2 aptamer conjugated to the free Apt_1 of the AuNPs-Apt complex on the surface of the DGE (DENV-NS1) (**f**). The MB amount is inversely proportional to the DENV-NS1 concentration in the sample solution, as it represents the amount of the hybridized complex of Apt_1 and Apt_2 within the 3D-nanoassembly. The oxidation peak in the DPV analysis indicates the amount of MB carried only by the AuNPs-Apt complex after the free MB was washed out.

6.3.2 Characterization of the AuNPs-Apt1, AuNPs-Apt2, and 3D-nanoassembled AuNPs-Apt complex

Affinity binding was used to attach aptamers to AuNPs., as illustrated in **Figure 6.2a**. The biotin-streptavidin conjugation was used to bind biotin-functionalized Apt_1 with streptavidin-functionalized AuNPs, and Au-thiol coordination attached the AuNP with thiolated Apt_2 to form the AuNPs-Apt_2. Both functionalized AuNPs were characterized by absorbance to confirm the AuNPs-Apt conjugation, as seen in **Figure 6.2b.** AuNPs maintain their plasmonic characteristics after conjugation of the two Apts, with peaks at 525 nm and no noticeable shoulder. Unlike the single AuNPs-Apt, the combination showed a shift in absorbance spectra, with diminished absorbance at 525 nm and immersion of a second broad peak at about 616 nm, implying AuNP aggregation. (Baeissa et al. 2010). The visual color of the solution's color as seen in the inset image of **Figure 6.2b** indicated that AuNPs-Apt_1 and AuNPs-Apt_2 both have red-pinkish color, but it turned to blueish color by time when they are mixed together.

Further, Transmission electron microscopy (TEM) analysis was done to observe the morphically nano assembled formed between AuNPs-Apt_1 and AuNPs-Apt_2. As shown in First, as shown in **Figure 6.2c**, with the size of 20 nm in dimater, the AuNPs-Apt_1 was visibly monodispersed. The agglomerating of the AuNPs-Apt complex was visible started even as early as 5 minutes after the mixing, indicating the feasibly interaction between the AuNPs-Apt_1 and AuNPs-Apt_2. The aggregation of the AuNPs was evitable in the presence of two AuNPs-Apt. With same approach, AuNP-Apt with different sizes were conjugated to the aptamers; 20 nm AuNPs for Apt_1 whereas 5 nm AuNPs for Apt_2. Under the TEM analysis, it was more visibly that the aggregation of the AuNPs attributed to the Apt complex and duplex formation because of the difference sizes of the conjugated AuNPs as seen in **Figure 6.2d**. Individual AuNPs-Apt_1 was visibly well-dispersed with size of 20 nm. Then, it started to interact to

smaller AuNPs-Apt$_2$ that introduced in the system. The agglomeration of AuNPs was progressing along the time and visibly observed when the AuNPs-Apt$_1$ was shown to be surrounded and bounded by the AuNPs-Apt$_2$, forming larger collective body of AuNPs which is bridged via duplex sense-antisense (He et al. 2019b; Luo et al. 2020). The aggregation of the AuNPs-Apt complex resembled a 3D-nano network attributed to the fact that several aptamers were conjugated on the AuNPs' surface and capable of binding to each other in three-directional manner. These resulted to a formation of 3D-nanoassemble network of AuNPs.

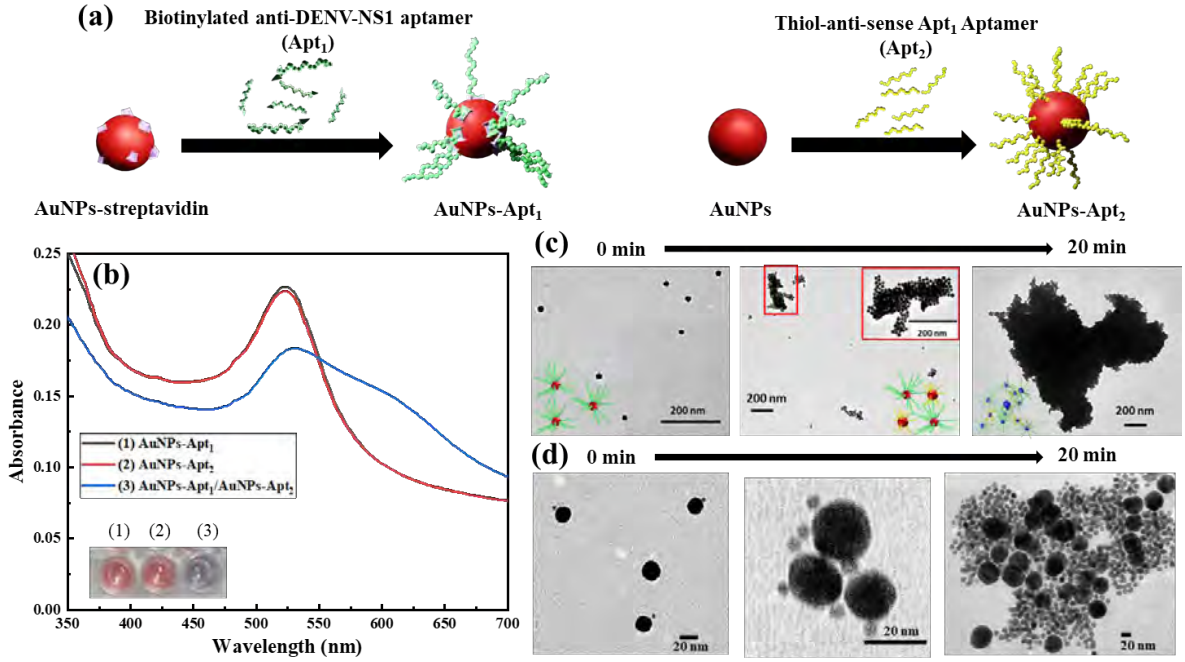

Figure 6.2 Characterization of 3D-nanoasembly aggregation of AuNPs-Apt$_1$ and AuNPs-Apt$_2$. (**a**) The illustration of the preparation of AuNPs-Apt$_1$ and AuNPs-Apt$_2$; (**b**) Absorbance and visual images of the AuNPs-Apt$_1$ (1), AuNPs-Apt$_2$ (2) and AuNPs-Apt$_1$/AuNPs-Apt$_2$ (3); TEM images of time-dependent nanoassembled formation of (**c**) AuNPs-Apt$_1$ (20)/AuNPs-Apt$_2$ (20), and (**d**) AuNPs-Apt$_1$ (20)/AuNPs-Apt$_2$ (5). The scale bars of the images are represented on each image.

6.3.3 The Binding confirmation of DENV-NS1 using the plasmonic shift of AuNPs-Apt1/AuNPs-Apt2 aptasensor

To acquire the maximal binding in the competitive format of the aptamer-DENV-NS1, the incubation duration of AuNPs-Apt_1 was investigated. The binding of AuNPs-Apt_1 increased by the incubation time, reaching saturation at 20 minutes for binding DENV-NS1. (**Figure 6.3a**). Further, to complete the set with the competitive binding assay, AuNPs-Apt_1 was also assayed to the AuNPs-Apt_2. The average of 5 min for the AuNPs-Apt_2 was determined as optimal incubation time for the pair aptamer-conjugated AuNPs as indicated in **Figure 6.3b**.

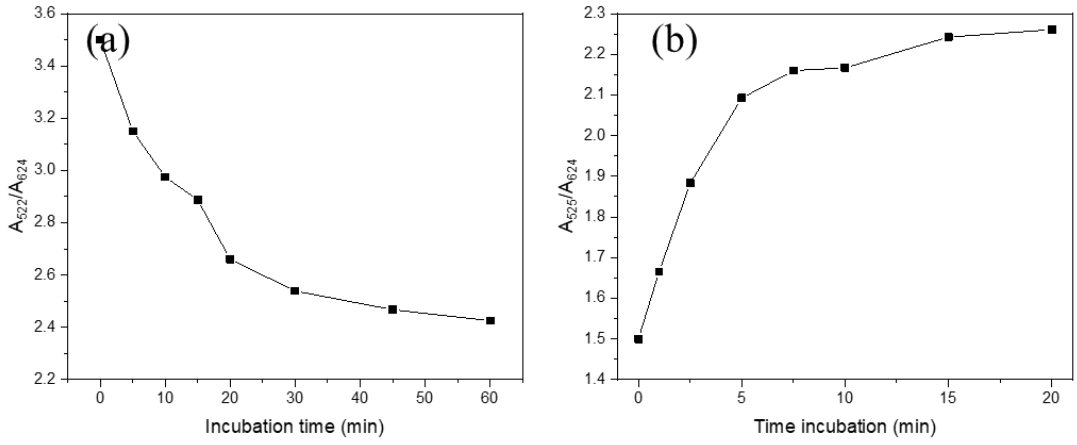

Figure 6.3 Optimization of AuNPs-Apt_1 and AuNPs-Apt_2 binding

A range of concentrations of the target analyte were used to understand the binding of DENV-NS1 to the aptasensor's system. The detection process began with AuNPs-Apt_1 binding to DENV-NS1 and proceeded with AuNPs-Apt_2 binding to the free Apt_1 on AuNPs-Apt_1. As shown in **Figure 6.4a**, at 525 nm, AuNPs-Apt1 displays a single peak. The intensity of the shoulder peak at about 624 nm increased as the concentration of DENV-NS1 increased. Furthermore, with increased DENV-NS1 concentration, a minor shift of the systems is

particularly detected. Following on from the association of AuNPs-Apt$_1$-DENV-NS1, AuNPs-Apt$_2$ was added to the mixture, which exacerbated the absorbance spectrum alteration.. At the addition of AuNPs-Apt$_2$ in the absent of DENV-NS1 in the solution, it heightened the shoulder spectra at 624 nm and lowered the absorbance peak at 525 nm (**Figure 6.4b**). These were different in reverse to the AuNPs-Apt$_1$ after the DENV-NS1 addition. In the addition of AuNPs-Apt$_2$ the agglomeration of the AuNPs-Apts was promoted since both aptamers would undergo hybridization and lead to the 3D-nanoassembly structure of AuNPs (He et al. 2019a). The interaction of AuNPs-Apt$_1$ and DENV-NS1 demonstrated reduced shoulder absorbance with increasing DENV-NS1 concentration, in contrast to the prior pattern. The absorbance at 525 nm was greater than the control signal (blank solution), indicating less AuNP aggregation in the system and less conjugation between AuNPs-Apt$_1$ and DENV-NS1 following binding to AuNPs-Apt$_2$.

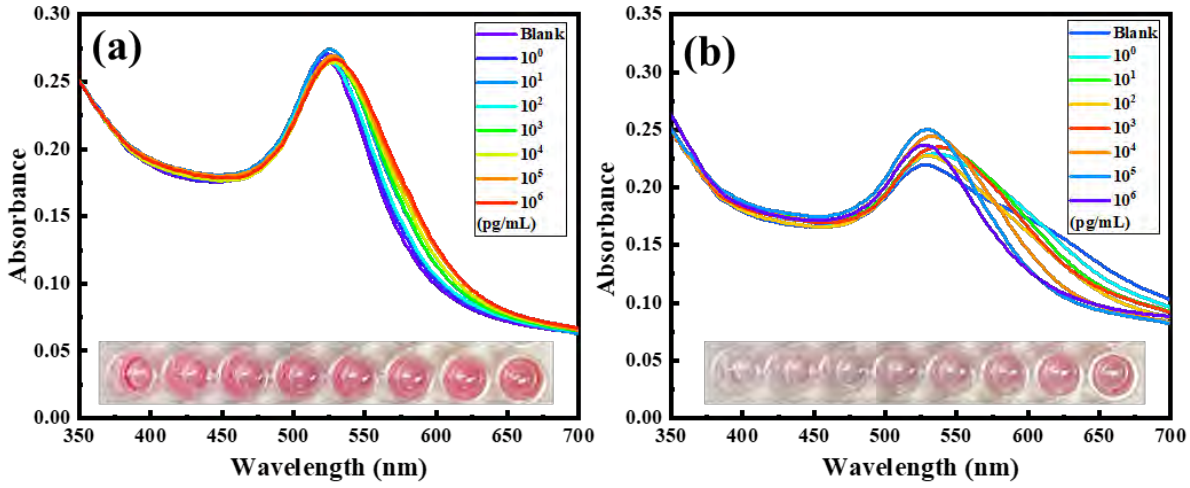

Figure 6.4 The binding confirmation of DENV-NS1 to the AuNPs-Apt. The absorbance spectra of the AuNPs-Apt$_1$ (**a**) after the addition of DENV-NS1 and (**b**) the addition of DENV-NS1 and AuNPs-Apt$_1$. The inset image is the visual color of the corresponding mixture.

6.3.4 Electrochemical characterization of 3D-nanoassembled AuNPs-Apt as MB nanocarrier

To analyze the assembly of the nanostructure of the conjugated aptamers on the DGE, electrochemical impedance spectroscopy (EIS) was used. DGE was chosen as the biosensor platform for its simplicity and ease of use in the finding of more advancement of sensitive analytical technique. Initially, the 3D-nanoassembly AuNPs on the DGE were studied to determine whether they were bound to the electrode's surface prior to detection. A typical Nyquist plot of Au-printed electrodes was shown by DGE. (**Figure 6.5a**). The electrode's impedance rose when Apt_2 was immobilized on the DGE (DGE/Apt_2). Subsequently, on the DGE/Apt_2, AuNPs-Apt_1 was captured and the assemble of AuNPs on the DGE's surface improves its electrical characteristics, as demonstrated by decreased impedance. In contrast to prior assembled layer, the assembly of AuNPs-Apt_1/AuNPs-Apt_2 complex on the electrode oppositely resulted to higher impedance. The building layer on the DGE by AuNPs-Apt_1/AuNPs-Apt_2 is indicating a different electronical characteristic than AuNPs-Apt_1. In the case of detection, the presence of bigger biomolecules, such as DENV-NS1 within the 3D-nanoassembled structure on the DGE exhibited a significantly greater impedance. These results show that an AuNPs-Apt1 single layer gives better charge transfer layer than a 3D-nanoassembled structure of AuNPs on the DGE created by aptamer hybridization.

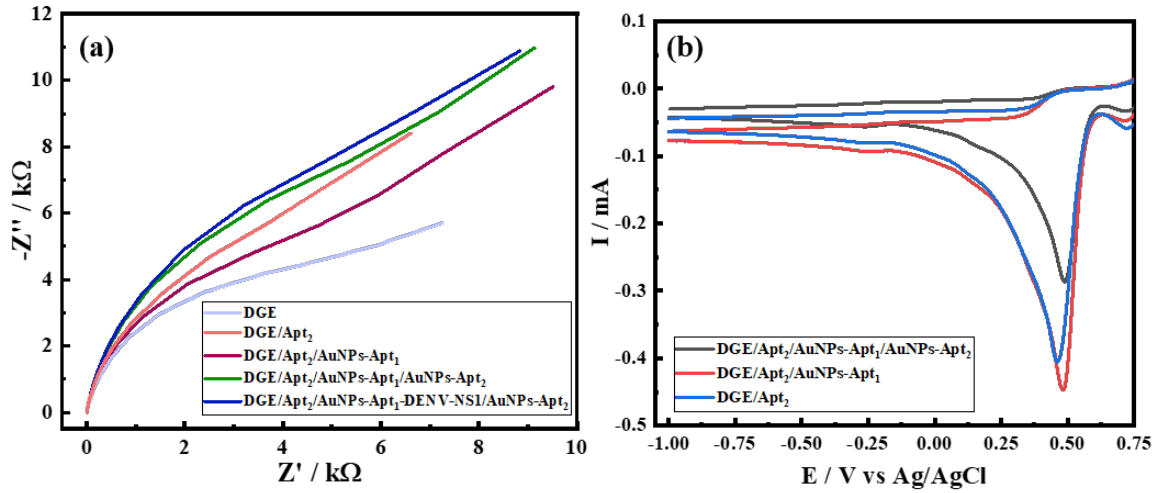

Figure 6.5 Electrochemical performance of 3D-nanoassembly AuNPs on a disposable gold electrode (DGE). (**a**) Electrochemical Impedance Spectroscopy (EIS) and (**b**) Cyclic voltammetry (CV) of the captured AuNPs-Apt_1/AuNPs-Apt_2 on Apt_2-functionalized DGE with a scan rate of 75 mV/s;

The DGE was also subjected to cyclic voltammetry to further understand the redox behavior on the working electrode's surface (Dutta Chowdhury et al. 2018). To understand the difference between AuNPs-Apt_1 and AuNPs-Apt_2, the surface of the DGE was profiled. DGE/Apt_2/AuNPs-Apt_1 was discovered to be the sole layer of AuNPs on the DGE with a comparable oxidation current to DGE/Apt. However, DGE/Apt2/AuNPs-Apt_1/AuNPs-Apt_2 resulted in 3D-nanoassembly AuNPs isolating DGE's surface, lowering the electron current on the electrode's surface and reducing the oxidation peak in the cyclic voltammetry profile. **Figure 6.5b** shows a peak in the run with a potential of approximately 490 mV, suggesting a typical reduction-oxidation profile of gold printed electrodes (Rodovalho et al. 2018).

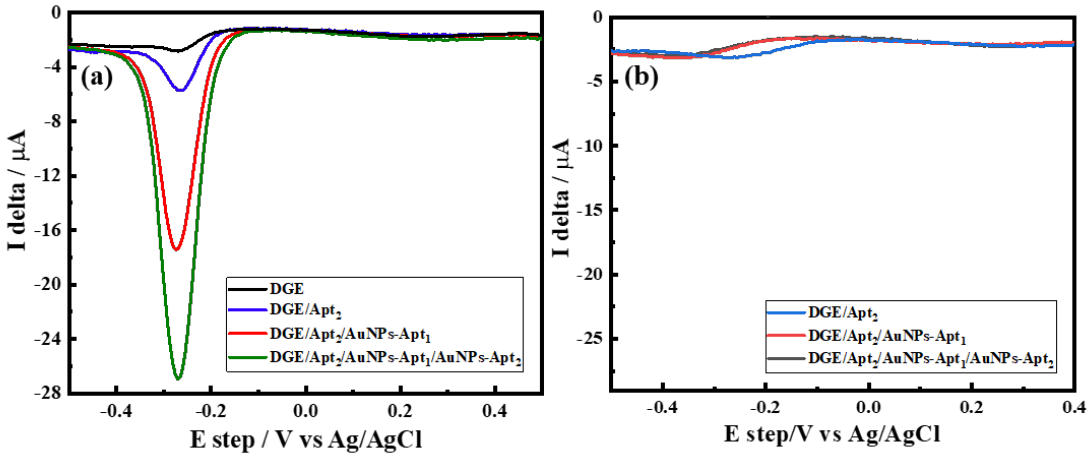

Figure 6.6 Electrochemical performance of captured 3D-nanoassembly AuNPs-Apt$_1$/AuNPs-Apt$_2$ (**a**) with MB and (**b**) without MB.

In this developed aptasensor, aptamer which was anchored on the AuNPs and assembled with the anti-sense to form the 3D-nano network acted as redox molecules' chelation sites on the electrochemical interfacial surface. To test this, AuNPs-Apt$_1$ and AuNPs-Apt$_2$ were mixed up in MB solution before being introduced on the DGE/Apt$_2$. This allowed a greater amount of MB to be intercalated within the aptamer. The current obtained in DPV analysis was used to calculate the loaded quantity of the MB. (Khezrian et al. 2013)(**Figure 6.6a**). The standard oxidation peak of the MB was founded at –0.28 mV (Taghdisi et al. 2019). Because Apt$_2$ was directly coupled to DGE, MB molecules complexed and demonstrated stronger DPV current versus untreated DGE, rising from –3 µA to – 4.5 µA in intensity. This implies that Apt$_2$ was effectively conjugated, and that MB was intercalated on the capturing probing. In electrochemical detection, this is determined as the noise/background signal. Furthermore, in the vicinity of trapped AuNPs-Apt on the surface of DGE/Apt$_2$, the DPV analysis revealed a strong MB signal in DGE/Apt$_2$/AuNPs-Apt$_1$ and DGE/Apt$_2$/AuNPs-Apt$_1$/AuNPs-Apt$_2$, with current intensities of –16 µA and –27 µA, respectively. Based on the preliminary study from the MB within the AuNPs-Apt, the signal-to-noise ratio was calculated around 3-folds for AuNPs-Apt$_1$-based nano-assembly and 6-folds for AuNPs-Apt$_1$/AuNPs-Apt$_2$-based 3D-

nanoassembly structure. These signals were demonstrated to be 2.4% in variance on 10 independence DGEs, showing an appropriate signal transducer for the electrochemical aptasensor (**Figure 6.7**). In a control experiment of AuNPs-Apt nanoassembly in the absence ofthe absence of MB, an ignorable hump of oxidation current was observed between potential values of – 250 mV to – 450 mV (**Figure 6.6b**), like the bare DGE's potential value with the current around – 2.5 µA. It is clearly shown that the MB as a redox probe is the only responsible source of current in this electrochemical detection.

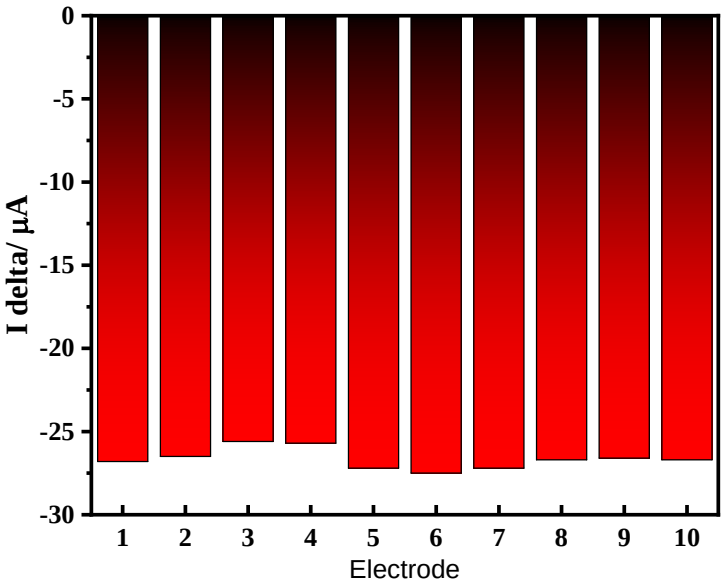

Figure 6.7 Reproducibility of the electrochemical baseline signal in 10 electrodes in DPV analysis

6.3.5 The electrochemical detection of DENV-NS1 using the AuNPs-Apt1/AuNPs-Apt2 aptasensor

The electrochemical detection of the DENV-NS1 was carried out after incubating the AuNPs-Apt complex/DENV-NS1 in MB solution. MB's oxidation peak was observed at a potential of around – 250 mV, shown in **Figure 6.8a**. As the concentration of the DENV-NS1 increased, the differential current, known as I delta in DPV analysis (ΔI), increased. Moreover, the dominant peak from – 250 mV was coupled to peak at potential around –320 mV,,

representing the MB contribution to DGE. A higher concentration of the DENV-NS1 resulted in lowering oxidation peak in the DPV while increasing the I delta value from a negative value to a less negative value. In the absence of a target, the conjugated aptamers-AuNPs contain the maximum number of MB, resulting in strong peak at –250 mV. After a gradual increase of DENV-NS1, the peak of MB decreased gradually and shifted towards –320 mV, which is the signal of DGE in the presence of MB. In case of a high concentration of target DENV-NS1, all apt_1 are completely blocked, and there is no space for MB loading on the electrode surface. As a result, the peak intensity in DPV is almost insignificant, like the bare electrode without MB.

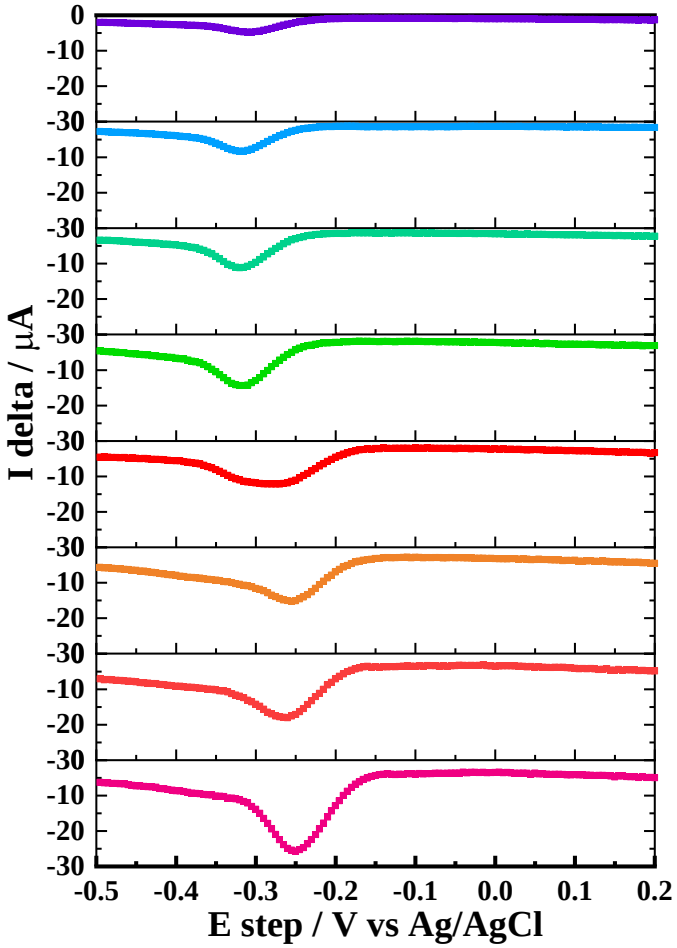

Figure 6.8 DPV analysis of the aptasensor in response to the DENV-NS1 detection using the proposed aptasensor on Apt_2-immobilized Disposable Gold Electrode (DGE).

The detection result was plotted with y-axis indicating the change of I delta ($\Delta I - \Delta I_{blank}$) at step potential of –250 mV and x-axis indicating the concentration of DENV-NS1 (**Figure 6.9**). The linear response was obtained from the plot with R^2 coefficient of 99.2% along the range of 1 pg/mL – 1 ng/mL concentration of DENV-NS1. At 1 ng/mL concentration of DENV-NS1, It was found to be saturated, with a larger cluttering signal at higher concentrations. The calculated detection limit was calculated at 30 fg/mL. This result emphasizes the advantage of the 3D-nanoassembly structure of AuNPs-Apt as a nanocarrier in electrochemical detection. A comparative study on previously published works was summarized in **Table 6.1** (Junior et al. 2021; Nawaz et al. 2018; Santos et al. 2018), showing that the detection limit of the proposed aptasensor was superior in terms of detection limit and dynamic range.

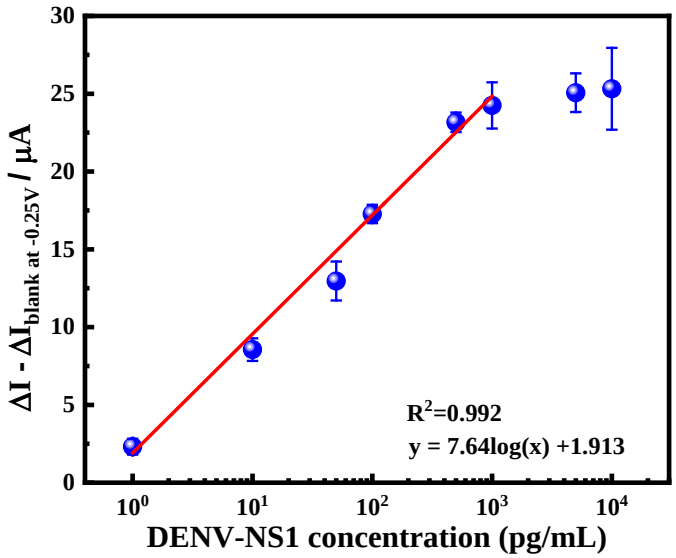

Figure 6.9 semi-*log* plot of change of differential current (ΔI) vs. concentration of DENV-NS1 in the electrochemical detection of DENV-NS1 using the proposed aptasensor on Apt_2-immobilized Disposable Gold Electrode (DGE)

Table 6.1 Comparative study of the previous work related to DENV NS1 detection

Detection Principle	Conjugate	C_{LOD} (ng/mL)	Linear range (ng/mL)
Immunofluorescence	Antibody	15	15–500
Electrochemical (EIS[1], SPCE[2])	Antibody	0.3	1–200
Electrochemical (Capacitive)	Antibody	0.34	1–5000
Electrochemical (EIS)	Aptamer	0.05	0.01–1000
Colorimetric	ELISA kit[3]	1	1–100
Colorimetric	ELISA kit[4]	1.5×10^{-2}	–
Electrochemical (DPV)	Aptamer	3.0×10^{-5}	0.001–1

[1]EIS = Electrochemical Impedance Spectroscopy
[2]SPCE = Screen-Printed Carbon Electrode
[3]TANAKA Kikinzoku Kogyo (TKK) ELISA kit
[4]J. Mitra & Co. Pvt. Ltd Dengue NS1 Ag Microlisa kit in dried DENV vector (mosquito)

Various kinds of non-target analytes, such as Norovirus-like particles (NoV-LPs), inactivated Influenza virus A/H1N1, and A/H3N2 was assayed to demonstrate the specificity of the aptasensor. As shown in **Figure 6.10**, the aptasensor indicated similar signal between the sample containing non-target analyte and the blank solution ranging from 98% – to 102%. On the opposite side, the aptasensor indicates change of signal decreasing down to 40% of electrochemical signal at the detection of 100 pg/mL DENV-NS1. It showed that the aptasensor could distinguish the target analyte in picogram level within the nanogram level noise matrixes. Furthermore, the proposed aptasensor could detect DENV-NS1 with a relative standard deviation (RSD) ranging from 6.1% to 10.2% in a spike solution of 2% human blood. (**Table**

6.2). However, despite a considerably low RSD value, the developed aptasensor still showed an interfering effect in serum, probably coming from the buffer constituents and the lysates protein (Tate and Ward 2004). The conventional strategy was employed up to 50-folds dilution, requiring a pre-treatment and pre-dilution for the highly complex analyte.

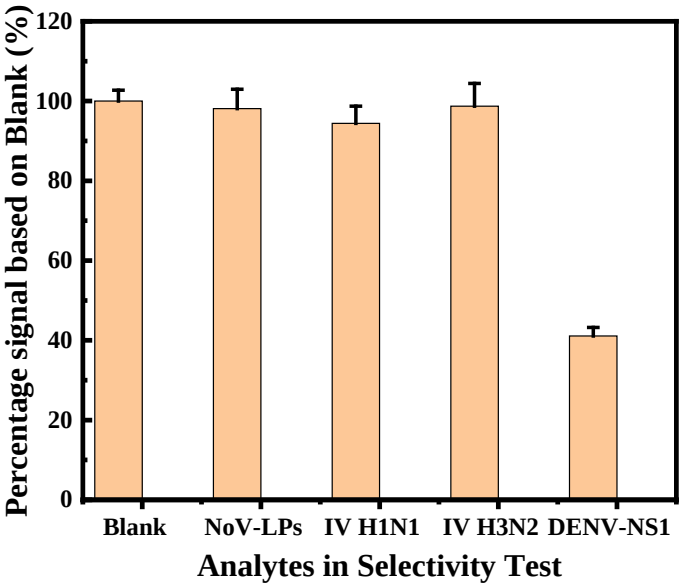

Figure 6.10 The selectivity test of the proposed aptasensor used in electrochemical detection

Table 6.3 The recovery test of the dual-approach of DENV-NS1 in human serum using AuNPs-Apt_1/AuNPs-Apt_2 based aptasensor

Sample No.[1]	DENV-NS1 concentration (pg/mL)	Recovery of DENV-NS1 concentration (%)			
		CL.D[2]	RSD[3] (%)	EC.D[4]	RSD (%)
1	2500	98.6	8.50	99.4	10.20
2	1000	112.5	6.15	120.5	8.71
3	500	115.4	4.12	105.1	6.70

[1]DENV-NS1 were spiked in 2% human serum with three independent detections for each sample.
[2]CL.D: colorimetric detection
[3]EC.D: electrochemical detection.
[4]RSD: relative standard deviation calculated from three samples detection.

6.4. Conclusions

This research described an enhanced electrochemical aptasensor that attributed from 3D-nanoassembled aptamers-conjugated AuNPs to amplify the redox signal via aptamer-duplex intercalation. The 3D-nanoassembled formation was observed and optimized by the visual color change and assessed on its function for electrochemical detection. DENV-NS1 was detected based on the competitive occupation of the aptamer, preventing the formation of the duplex. The less the duplex was formed, it will reduce the amount of the moiety of the 3D-nanoassembled AuNPs to the redox molecules. By this approach, it demonstrated a LOD of 30 fg/mL. The developed strategy aimed to deliver an elevated concept of the general approach in aptamer-based detection and establish an early-diagnostic method for low virus concentration or low available biomarkers by considering the mechanism of signal amplification.

Chapter 7

Conclusion

Conclusion

The proposed capture immunoassay utilizing nanocarrier and nanozymes enhanced the signal amplification in terms of detection limit and functionality of the immunoassay. The optimization and three-dimensional space of the nanoencapsulation and framework increased the active signal molecules of the nanomaterials. They simultaneously brought folds of the signal transducer in an individual antibody-antigen conjugation within the immunoassay. The immunoassay has been applied to detect Influenza Virus (IV/A), Norovirus (NoV), Dengue Virus NS1 protein, and SARS-CoV-2. It showed high sensitivity and selectivity toward the target infectious disease agents depending on the conjugated biorecognition of the immunoassay system. The detection limits of the developed assay in the range of femtogram level of IV/A, NoV, Dengue NS1 protein, Spike protein, and Nucleocapsid protein of SARS-CoV-2 were successfully shown to identify the subtype of the IV/A/H1N1 and IV/A/H3N2. In addition, a positive reaction was also detectable by the naked eye. It was also interesting that the stepwise comparative study on the precedence nanomaterials composing the nano-enrichment strategy indicated folds of signal amplification in the immunoassay. These included TMB-NPs to TMB-NPs@PLGA, solvent-dependent nanoprecipitation dye@PLGA, ZIF-67 to oxidized ZIF-67-forming Co_3O_4 to embedment of PtNPs, and a single assembly layer to the three-dimensional assembly of gold-aptamer (AuNPs-Apt) as redox species chelating space. This proposed immunoassay showed adaptable and highly sensitive virus detection with application in a colorimetric and electrochemical system. Due to the feasible nanomaterials and adjustment to existing immunoassay, this enhancement method could be easily assembled and integrated into a current diagnostic concept for excellent monitoring systems to promote public hygiene.

References

Abraham, P.R., Bharathy, R., Kumar, P., Kumar, A., 2021. Dengue NS1 antigen kit shows high sensitivity for detection of recombinant dengue virus-2 NS1 antigen spiked with Aedes aegypti mosquitoes. Sci. Rep. 11, 1–8.

Achadu, O.J., Takemura, K., Khoris, I.M., Park, E.Y., 2020. Plasmonic/magnetic molybdenum trioxide and graphitic carbon nitride quantum dots-based fluoroimmunosensing system for influenza virus. Sens. Actuators, B 321, 128494.

Ahmed, S.R., Hossain, M.A., Park, J.Y., Kim, S.-H., Lee, D., Suzuki, T., Lee, J., Park, E.Y., 2014. Metal enhanced fluorescence on nanoporous gold leaf-based assay platform for virus detection. Biosens. Bioelectron. 58, 33-39.

Ahmed, S.R., Kim, J., Suzuki, T., Lee, J., Park, E.Y., 2016a. Detection of influenza virus using peroxidase‐mimic of gold nanoparticles. Biotechnol. Bioeng. 113(10), 2298-2303.

Ahmed, S.R., Kim, J., Suzuki, T., Lee, J., Park, E.Y., 2016b. Enhanced catalytic activity of gold nanoparticle-carbon nanotube hybrids for influenza virus detection. Biosensors and Bioelectronics 85, 503–508.

Ahmed, S.R., Kim, J., Suzuki, T., Neethirajan, S., Lee, J., Park, E.Y., 2017a. In situ self-assembly of gold nanoparticles on hydrophilic and hydrophobic substrates for influenza virus-sensing platform. Sci. Rep. 7, 44495.

Ahmed, S.R., Takemeura, K., Li, T.-C., Kitamoto, N., Tanaka, T., Suzuki, T., Park, E.Y., 2017b. Size-controlled preparation of peroxidase-like graphene-gold nanoparticle hybrids for the visible detection of norovirus-like particles. Biosens. Bioelectron. 87, 558–565.

Arima, A., Tsutsui, M., Yoshida, T., Tatematsu, K., Yamazaki, T., Yokota, K., Kuroda, S.i., Washio, T., Baba, Y., Kawai, T., 2020. Digital Pathology Platform for Respiratory

Tract Infection Diagnosis via Multiplex Single-Particle Detections. ACS Sens. 5(11), 3398–3403.

Aydin, S., 2015. A short history, principles, and types of ELISA, and our laboratory experience with peptide/protein analyses using ELISA. Peptides 72, 4–15.

Baeissa, A., Dave, N., Smith, B.D., Liu, J., 2010. DNA-functionalized monolithic hydrogels and gold nanoparticles for colorimetric DNA detection. ACS Appl. Mater. Interfaces 2(12), 3594–3600.

Barman, S., Hossain, M., Yoon, H., Park, J.Y., 2018. Trimetallic Pd@ Au@ Pt nanocomposites platform on-COOH terminated reduced graphene oxide for highly sensitive CEA and PSA biomarkers detection. Biosensors and Bioelectronics 100, 16-22.

Baynton, K.J., Bewtra, J.K., Biswas, N., Taylor, K.E., 1994. Inactivation of horseradish peroxidase by phenol and hydrogen peroxide: a kinetic investigation. Biochimica et Biophysica Acta (BBA)-Protein Structure and Molecular Enzymology 1206(2), 272–278.

Bhardwaj, J., Chaudhary, N., Kim, H., Jang, J., 2019. Subtyping of influenza A H1N1 virus using a label-free electrochemical biosensor based on the DNA aptamer targeting the stem region of HA protein. Anal. Chim. Acta 1064, 94–103.

Bilati, U., Allémann, E., Doelker, E., 2005. Development of a nanoprecipitation method intended for the entrapment of hydrophilic drugs into nanoparticles. Eur. J. Pharm. Sci. 24(1), 67–75.

Boonyakida, J., Utomo, D.I.S., Soma, F.N., Park, E.Y., 2022. Two-step purification of tag-free norovirus-like particles from silkworm larvae (Bombyx mori). Protein Expression Purif. 190, 106010.

Bosch, A., Gkogka, E., Le Guyader, F.S., Loisy-Hamon, F., Lee, A., van Lieshout, L., Marthi, B., Myrmel, M., Sansom, A., Schultz, A.C., 2018. Foodborne viruses: Detection, risk assessment, and control options in food processing. International journal of food microbiology 285, 110-128.

Busch, R.T., Karim, F., Weis, J., Sun, Y., Zhao, C., Vasquez, E.S., 2019. Optimization and structural stability of gold nanoparticle–antibody bioconjugates. ACS omega 4(12), 15269-15279.

Cao, X., Liu, M., Zhao, M., Li, J., Xia, J., Zou, T., Wang, Z., 2022. Synergetic PtNP@ Co3O4 hollow nanopolyhedrals as peroxidase-like nanozymes for the dual-channel homogeneous biosensing of prostate-specific antigen. Analytical and bioanalytical chemistry, 1921–1932.

Chang, Y.-F., Wang, S.-F., Huang, J.C., Su, L.-C., Yao, L., Li, Y.-C., Wu, S.-C., Chen, Y.-M.A., Hsieh, J.-P., Chou, C., 2010. Detection of swine-origin influenza A (H1N1) viruses using a localized surface plasmon coupled fluorescence fiber-optic biosensor. Biosens. Bioelectron. 26(3), 1068-1073.

Chen, Y.-J., Chen, M., Hsieh, Y.-C., Su, Y.-C., Wang, C.-H., Cheng, C.-M., Kao, A.-P., Wang, K.-H., Cheng, J.-J., Chuang, K.-H., 2018. Development of a highly sensitive enzyme-linked immunosorbent assay (ELISA) through use of poly-protein G-expressing cell-based microplates. Scientific reports 8.

Chen, Y., Xianyu, Y., Wang, Y., Zhang, X., Cha, R., Sun, J., Jiang, X., 2015. One-step detection of pathogens and viruses: combining magnetic relaxation switching and magnetic separation. ACS Nano 9(3), 3184–3191.

Cheng, N., Song, Y., Zeinhom, M.M., Chang, Y.-C., Sheng, L., Li, H., Du, D., Li, L., Zhu, M.-J., Luo, Y., 2017. Nanozyme-mediated dual immunoassay integrated with

smartphone for use in simultaneous detection of pathogens. ACS Appl. Mater. Interfaces 9(46), 40671-40680.

Cheng, Q., Yang, Y., Peng, Y., Liu, M., 2020. Pt nanoparticles with high oxidase-like activity and reusability for detection of ascorbic acid. Nanomaterials 10(6), 1015.

Chowdhury, A.D., Ganganboina, A.B., Park, E.Y., Doong, R.-a., 2018. Impedimetric biosensor for detection of cancer cells employing carbohydrate targeting ability of Concanavalin A. Biosens. Bioelectron. 122, 95-103.

Colón-González, F.J., Sewe, M.O., Tompkins, A.M., Sjödin, H., Casallas, A., Rocklöv, J., Caminade, C., Lowe, R., 2021. Projecting the risk of mosquito-borne diseases in a warmer and more populated world: a multi-model, multi-scenario intercomparison modelling study. The Lancet Planetary Health 5(7), e404–e414.

Dahmana, H., Mediannikov, O., 2020. Mosquito-Borne Diseases Emergence/Resurgence and How to Effectively Control It Biologically. Pathogens 9(4), 310.

Dai, Z., Liu, S., Bao, J., Ju, H., 2009. Nanostructured FeS as a mimic peroxidase for biocatalysis and biosensing. Chemistry-A European Journal 15(17), 4321–4326.

Dang, V.D., Ganganboina, A.B., Doong, R.-A., 2020. Bipyridine-and Copper-Functionalized N-doped Carbon Dots for Fluorescence Turn Off–On Detection of Ciprofloxacin. ACS Appl. Mater. Interfaces 12(29), 32247–32258.

de Graaf, M., van Beek, J., Vennema, H., Podkolzin, A., Hewitt, J., Bucardo, F., Templeton, K., Mans, J., Nordgren, J., Reuter, G., 2015. Emergence of a novel GII. 17 norovirus–End of the GII. 4 era? Eurosurveillance 20(26), 1–8.

de Lima, L.F., Ferreira, A.L., Torres, M.D., de Araujo, W.R., de la Fuente-Nunez, C., 2021. Minute-scale detection of SARS-CoV-2 using a low-cost biosensor composed of pencil graphite electrodes. Proceedings of the National Academy of Sciences 118(30).

Dhal, A., Kalyani, T., Ghorai, S., Sahu, N.K., Jana, S.K., 2020. Recent development of electrochemical immunosensor for the diagnosis of dengue virus NSI protein: A review. Sensors International, 100030.

Duchamp, M.B., Casalegno, J., Gillet, Y., Frobert, E., Bernard, E., Escuret, V., Billaud, G., Valette, M., Javouhey, E., Lina, B., 2010. Pandemic A (H1N1) 2009 influenza virus detection by real time RT‐PCR: is viral quantification useful? Clin. Microbiol. Infect. 16(4), 317–321.

Dutta Chowdhury, A., Agnihotri, N., Doong, R.-a., De, A., 2017. Label-free and nondestructive separation technique for isolation of targeted DNA from DNA–protein mixture using magnetic Au–Fe3O4 nanoprobes. Analytical chemistry 89(22), 12244-12251.

Dutta Chowdhury, A., Ganganboina, A.B., Nasrin, F., Takemura, K., Doong, R.-a., Utomo, D.I.S., Lee, J., Khoris, I.M., Park, E.Y., 2018. Femtomolar detection of dengue virus DNA with serotype identification ability. Anal. Chem. 90(21), 12464-12474.

Eivazzadeh-Keihan, R., Pashazadeh-Panahi, P., Mahmoudi, T., Chenab, K.K., Baradaran, B., Hashemzaei, M., Radinekiyan, F., Mokhtarzadeh, A., Maleki, A., 2019. Dengue virus: a review on advances in detection and trends–from conventional methods to novel biosensors. Microchim. Acta 186(6), 1–24.

Fan, C., Jiang, X., Chen, J., Wang, X., Qian, S., Zhao, C., Ding, L., Sun, D., Tang, Y., 2021. Low‐load Pt nanoclusters anchored on graphene hollow spheres for efficient hydrogen evolution. Small Structures 2(1), 2000017.

Farjami, E., Clima, L., Gothelf, K.V., Ferapontova, E.E., 2010. DNA interactions with a methylene blue redox indicator depend on the DNA length and are sequence specific. Analyst 135(6), 1443-1448.

Fu, Y., Zhao, X., Zhang, J., Li, W., 2014. DNA-based platinum nanozymes for peroxidase mimetics. The Journal of Physical Chemistry C 118(31), 18116-18125.

Ganganboina, A.B., Chowdhury, A.D., Khoris, I.M., Doong, R.-a., Li, T.-C., Hara, T., Abe, F., Suzuki, T., Park, E.Y., 2020a. Hollow magnetic-fluorescent nanoparticles for dual-modality virus detection. Biosens. Bioelectron. 170, 112680.

Ganganboina, A.B., Chowdhury, A.D., Khoris, I.M., Nasrin, F., Takemura, K., Hara, T., Abe, F., Suzuki, T., Park, E.Y., 2020b. Dual modality sensor using liposome-based signal amplification technique for ultrasensitive norovirus detection. Biosens. Bioelectron., 112169.

Ganganboina, A.B., Chowdhury, A.D., Khoris, I.M., Nasrin, F., Takemura, K., Hara, T., Abe, F., Suzuki, T., Park, E.Y., 2020c. Dual modality sensor using liposome-based signal amplification technique for ultrasensitive norovirus detection. Biosens. Bioelectron. 157, 112169.

Ganganboina, A.B., Doong, R.-a., 2018. The biomimic oxidase activity of layered V_2O_5 nanozyme for rapid and sensitive nanomolar detection of glutathione. Sens. Actuators, B 273, 1179-1186.

Ganganboina, A.B., Doong, R.-A., 2019. Graphene Quantum Dots Decorated Gold-Polyaniline Nanowire for Impedimetric Detection of Carcinoembryonic Antigen. Sci. Rep. 9(1), 7214.

Ganganboina, A.B., Dutta Chowdhury, A., Doong, R.-a., 2018. N-doped graphene quantum dots-decorated V_2O_5 nanosheet for fluorescence turn off–on detection of cysteine. ACS Appl. Mater. Interfaces 10(1), 614-624.

Ganganboina, A.B., Khoris, I.M., Chowdhury, A.D., Li, T.-C., Park, E.Y., 2020d. Ultrasensitive Detection of the Hepatitis E Virus by Electrocatalytic Water Oxidation Using Pt-Co3O4 Hollow Cages. ACS Appl. Mater. Interfaces 12(45), 50212–50221.

Gao, L., Zhuang, J., Nie, L., Zhang, J., Zhang, Y., Gu, N., Wang, T., Feng, J., Yang, D., Perrett, S., 2007. Intrinsic peroxidase-like activity of ferromagnetic nanoparticles. Nature nanotechnology 2(9), 577.

Gao, Z., Ye, H., Tang, D., Tao, J., Habibi, S., Minerick, A., Tang, D., Xia, X., 2017. Platinum-decorated gold nanoparticles with dual functionalities for ultrasensitive colorimetric in vitro diagnostics. Nano Letters 17(9), 5572-5579.

Ge, J., Lei, J., Zare, R.N., 2012. Protein–inorganic hybrid nanoflowers. Nat. Nanotechnol. 7(7), 428-432.

Giorgi-Coll, S., Marín, M.J., Sule, O., Hutchinson, P.J., Carpenter, K.L., 2020. Aptamer-modified gold nanoparticles for rapid aggregation-based detection of inflammation: an optical assay for interleukin-6. Microchim. Acta 187(1), 1–11.

Gulzar, A., Gai, S., Yang, P., Li, C., Ansari, M.B., Lin, J., 2015. Stimuli responsive drug delivery application of polymer and silica in biomedicine. J. Mater. Chem. B 3(44), 8599–8622.

Gupta, R., Kumar, A., Kumar, S., Pinnaka, A.K., Singhal, N.K., 2021. Naked eye colorimetric detection of Escherichia coli using aptamer conjugated graphene oxide enclosed Gold nanoparticles. Sens. Actuators, B 329, 129100.

Hall, A.J., Vinjé, J., Lopman, B., Park, G.W., Yen, C., Gregoricus, N., Parashar, U., 2011. Updated norovirus outbreak management and disease prevention guidelines. Morbidity and Mortality Weekly Report: Recommendations and Reports 60(3), 1–15.

Han, J.-H., Lee, D., Chew, C.H.C., Kim, T., Pak, J.J., 2016. A multi-virus detectable microfluidic electrochemical immunosensor for simultaneous detection of H1N1, H5N1, and H7N9 virus using ZnO nanorods for sensitivity enhancement. Sens. Actuators, B 228, 36-42.

Harrison, L.C., DiCaprio, E., 2018. Hepatitis E virus: an emerging foodborne pathogen. Frontiers in Sustainable Food Systems 2, 14.

He, M.-Q., Chen, S., Yao, K., Meng, J., Wang, K., Yu, Y.-L., Wang, J.-H., 2019a. Precisely Tuning LSPR Property via “Peptide-Encoded” Morphological Evolution of Gold Nanorods for Quantitative Visualization of Enzyme Activity. Anal. Chem. 92(1), 1395–1401.

He, M.Q., Chen, S., Yao, K., Wang, K., Yu, Y.L., Wang, J.H., 2019b. Oriented assembly of gold nanoparticles with freezing‐driven surface DNA manipulation and its application in SERS‐based MicroRNA assay. Small Methods 3(5), 1900017.

Hu, R., Wen, W., Wang, Q., Xiong, H., Zhang, X., Gu, H., Wang, S., 2014. Novel electrochemical aptamer biosensor based on an enzyme–gold nanoparticle dual label for the ultrasensitive detection of epithelial tumour marker MUC1. Biosens. Bioelectron. 53, 384–389.

Huang, Y., Ren, J., Qu, X., 2019. Nanozymes: classification, catalytic mechanisms, activity regulation, and applications. Chemical reviews 119(6), 4357-4412.

Hwang, H.J., Ryu, M.Y., Park, C.Y., Ahn, J., Park, H.G., Choi, C., Ha, S.-D., Park, T.J., Park, J.P., 2017. High sensitive and selective electrochemical biosensor: Label-free detection of human norovirus using affinity peptide as molecular binder. Biosensors and Bioelectronics 87, 164–170.

Idili, A., Parolo, C., Alvarez-Diduk, R., Merkoçi, A., 2021. Rapid and efficient detection of the SARS-CoV-2 spike protein using an electrochemical aptamer-based sensor. ACS Sens. 6(8), 3093–3101.

Ison, M.G., 2011. Antivirals and resistance: influenza virus. Current opinion in virology 1(6), 563–573.

Iswardy, E., Tsai, T.-C., Cheng, I.-F., Ho, T.-C., Perng, G.C., Chang, H.-C., 2017. A bead-based immunofluorescence-assay on a microfluidic dielectrophoresis platform for rapid dengue virus detection. Biosens. Bioelectron. 95, 174–180.

Jiang, B., Duan, D., Gao, L., Zhou, M., Fan, K., Tang, Y., Xi, J., Bi, Y., Tong, Z., Gao, G.F., 2018. Standardized assays for determining the catalytic activity and kinetics of peroxidase-like nanozymes. Nature protocols 13(7), 1506-1520.

Jiao, L., Yan, H., Xu, W., Wu, Y., Gu, W., Li, H., Du, D., Lin, Y., Zhu, C., 2019. Self-Assembly of All-Inclusive Allochroic Nanoparticles for the Improved ELISA. Anal. Chem. 91(13), 8461-8465.

Junior, B.B., Batistuti, M.R., Pereira, A.S., de Sousa Russo, E.M., Mulato, M., 2021. Electrochemical aptasensor for NS1 detection: Towards a fast dengue biosensor. Talanta 233, 122527.

Kabir, M.A., Zilouchian, H., Younas, M.A., Asghar, W., 2021. Dengue Detection: Advances in Diagnostic Tools from Conventional Technology to Point of Care. Biosensors 11(7), 206.

Kang, S.W., Lee, Y.W., Park, Y., Choi, B.-S., Hong, J.W., Park, K.-H., Han, S.W., 2013. One-pot synthesis of trimetallic Au@ PdPt core–shell nanoparticles with high catalytic performance. ACS nano 7(9), 7945-7955.

Karim, M.N., Anderson, S.R., Singh, S., Ramanathan, R., Bansal, V., 2018. Nanostructured silver fabric as a free-standing NanoZyme for colorimetric detection of glucose in urine. Biosensors and Bioelectronics 110, 8-15.

Khezrian, S., Salimi, A., Teymourian, H., Hallaj, R., 2013. Label-free electrochemical IgE aptasensor based on covalent attachment of aptamer onto multiwalled carbon nanotubes/ionic liquid/chitosan nanocomposite modified electrode. Biosens. Bioelectron. 43, 218–225.

Khoris, I.M., Chowdhury, A.D., Li, T.-C., Suzuki, T., Park, E.Y., 2020a. Advancement of capture immunoassay for real-time monitoring of hepatitis E virus-infected monkey. Anal. Chim. Acta.

Khoris, I.M., Chowdhury, A.D., Li, T.-C., Suzuki, T., Park, E.Y., 2020b. Advancement of capture immunoassay for real-time monitoring of hepatitis E virus-infected monkey. Analytica Chimica Acta 1110, 64-71.

Khoris, I.M., Ganganboina, A.B., Park, E.Y., 2021a. Self-Assembled Chromogenic Polymeric Nanoparticle-Laden Nanocarrier as a Signal Carrier for Derivative Binary Responsive Virus Detection. ACS Appl. Mater. Interfaces 13(31), 36868–36879.

Khoris, I.M., Ganganboina, A.B., Suzuki, T., Park, E.Y., 2021b. Self-assembled chromogen-loaded polymeric cocoon for respiratory virus detection. Nanoscale 13(1), 388–396.

Khoris, I.M., Takemura, K., Lee, J., Hara, T., Abe, F., Suzuki, T., Park, E.Y., 2019. Enhanced colorimetric detection of norovirus using in-situ growth of Ag shell on Au NPs. Biosens. Bioelectron. 126, 425-432.

Kim, J., Tran, V.T., Oh, S., Jang, M., Lee, D.K., Hong, J.C., Park, T.J., Kim, H.-J., Lee, J., 2021. Clinical trial: Magnetoplasmonic elisa for urine-based active tuberculosis detection and anti-tuberculosis therapy monitoring. ACS central science 7(11), 1898-1907.

Kim, M.S., Kweon, S.H., Cho, S., An, S.S.A., Kim, M.I., Doh, J., Lee, J., 2017. Pt-decorated magnetic nanozymes for facile and sensitive point-of-care bioassay. ACS applied materials & interfaces 9(40), 35133-35140.

Kitamoto, N., Tanaka, T., Natori, K., Takeda, N., Nakata, S., Jiang, X., Estes, M.K., 2002. Cross-reactivity among several recombinant calicivirus virus-like particles (VLPs) with monoclonal antibodies obtained from mice immunized orally with one type of VLP. Journal of clinical microbiology 40(7), 2459–2465.

Kocbek, P., Obermajer, N., Cegnar, M., Kos, J., Kristl, J., 2007. Targeting cancer cells using PLGA nanoparticles surface modified with monoclonal antibody. J. Controlled Release 120(1-2), 18-26.

Kou, B., Huang, W., Neill, F.H., Palzkill, T.G., Estes, M.K., Atmar, R.L., 2015. Norovirus Antigen Detection with a Combination of Monoclonal and Single Chain Antibodies. Journal of clinical microbiology, JCM. 02371–02315.

Kuo, P.-C., Lien, C.-W., Mao, J.-Y., Unnikrishnan, B., Chang, H.-T., Lin, H.-J., Huang, C.-C., 2018. Detection of urinary spermine by using silver-gold/silver chloride nanozymes. Analytica chimica acta 1009, 89-97.

Kushwaha, A., Takamura, Y., Nishigaki, K., Biyani, M., 2019. Competitive non-SELEX for the selective and rapid enrichment of DNA aptamers and its use in electrochemical aptasensor. Sci. Rep. 9(1), 1-11.

Laconi, A., Fortin, A., Bedendo, G., Shibata, A., Sakoda, Y., Awuni, J.A., Go-Maro, E., Arafa, A., Ali, A.S.M., Terregino, C., 2020. Detection of avian influenza virus: a comparative study of the in silico and in vitro performances of current RT-qPCR assays. Sci. Rep. 10(1), 1–9.

Lai, S.-C., Huang, Y.-Y., Shu, P.-Y., Chang, S.-F., Hsieh, P.-S., Wey, J.-J., Tsai, M.-H., Ben, R.-J., Hsu, Y.-M., Fang, Y.-C., 2019. Development of an enzyme-linked immunosorbent assay for rapid detection of dengue virus (DENV) NS1 and differentiation of DENV serotypes during early infection. J. Clin. Microbiol. 57(7), e00221-00219.

Lampejo, T., 2020. Influenza and antiviral resistance: an overview. Eur. J. Clin. Microbiol. Infect. Dis., 1–8.

Lee, G.-C., Jeon, E.-S., Kim, W.-S., Le, D.T., Yoo, J.-H., Chong, C.-K., 2010. Evaluation of a rapid diagnostic test, NanoSign® Influenza A/B Antigen, for detection of the 2009 pandemic influenza A/H1N1 viruses. Virology journal 7(1), 244.

Lee, J., Takemura, K., Park, E.Y., 2018. Plasmonic/magnetic graphene-based magnetofluoro-immunosensing platform for virus detection. Sens. Actuators, B 276, 254-261.

Leong, S.S., Ng, W.M., Lim, J., Yeap, S.P., 2018. Dynamic Light Scattering: Effective Sizing Technique for Characterization of Magnetic Nanoparticles. Handbook of Materials Characterization, pp. 77–111. Springer.

Li, J., Cao, Y., Hinman, S.S., McKeating, K.S., Guan, Y., Hu, X., Cheng, Q., Yang, Z., 2018. Efficient label-free chemiluminescent immunosensor based on dual functional cupric oxide nanorods as peroxidase mimics. Biosensors and Bioelectronics 100, 304–311.

Li, J., Stayshich, R.M., Meyer, T.Y., 2011a. Exploiting sequence to control the hydrolysis behavior of biodegradable PLGA copolymers. J. Am. Chem. Soc. 133(18), 6910–6913.

Li, M., Luo, M., Li, F., Wang, W., Liu, K., Liu, Q., Wang, Y., Lu, Z., Wang, D., 2016. Biomimetic copper-based inorganic–protein nanoflower assembly constructed on the nanoscale fibrous membrane with enhanced stability and durability. The Journal of Physical Chemistry C 120(31), 17348-17356.

Li, T.-C., Yamakawa, Y., Suzuki, K., Tatsumi, M., Razak, M., Uchida, T., Takeda, N., Miyamura, T., 1997. Expression and self-assembly of empty virus-like particles of hepatitis E virus. Journal of virology 71(10), 7207-7213.

Li, T.-C., Yoshimatsu, K., Yasuda, S.P., Arikawa, J., Koma, T., Kataoka, M., Ami, Y., Suzaki, Y., Mai, L.T.Q., Hoa, N.T., 2011b. Characterization of self-assembled virus-like particles of rat hepatitis E virus generated by recombinant baculoviruses. The Journal of general virology 92(Pt 12), 2830.

Li, Z., Zhang, S., Yu, T., Dai, Z., Wei, Q., 2019. Aptamer-based fluorescent sensor array for multiplexed detection of cyanotoxins on a smartphone. Anal. Chem. 91(16), 10448–10457.

Lin, C., Guo, Y., Zhao, M., Sun, M., Luo, F., Guo, L., Qiu, B., Lin, Z., Chen, G., 2017. Highly sensitive colorimetric immunosensor for influenza virus H5N1 based on enzyme-encapsulated liposome. Anal. Chim. Acta 963, 112-118.

Lin, Y., Zhou, Q., Zeng, Y., Tang, D., 2018. Liposome-coated mesoporous silica nanoparticles loaded with L-cysteine for photoelectrochemical immunoassay of aflatoxin B1. Microchim. Acta 185(6), 311.

Liu, X., Zhang, H., Qin, S., Wang, Q., Yang, X., Wang, K., 2019. Optical fiber amplifier for quantitative and sensitive point-of-care testing of myoglobin and miRNA-141. Biosens. Bioelectron. 129, 87–92.

Liu, Y., Yang, G., Baby, T., Chen, D., Weitz, D.A., Zhao, C.X., 2020. Stable polymer nanoparticles with exceptionally high drug loading by sequential nanoprecipitation. Angew. Chem. Int. Ed. 59(12), 4720–4728.

Long, L., Zong, M., Xie, Y., Chai, Q., Liu, J., Wu, X., 2021. Hollow Pt Nanocage@ Mesoporous SiO2 Nanoreactors as a Nanozyme for Colorimetric Immunoassays of Viral Diagnosis. ACS Applied Nano Materials.

Loynachan, C.N., Thomas, M.R., Gray, E.R., Richards, D.A., Kim, J., Miller, B.S., Brookes, J.C., Agarwal, S., Chudasama, V., McKendry, R.A., 2018. Platinum nanocatalyst amplification: redefining the gold standard for lateral flow immunoassays with ultrabroad dynamic range. ACS Nano 12(1), 279-288.

Lu, J., Zhang, H., Li, S., Guo, S., Shen, L., Zhou, T., Zhong, H., Wu, L., Meng, Q., Zhang, Y., 2020. Oxygen-vacancy-enhanced peroxidase-like activity of reduced Co3O4

nanocomposites for the colorimetric detection of H2O2 and glucose. Inorganic Chemistry 59(5), 3152-3159.

Luo, M., Xuan, M., Huo, S., Fan, J., Chakraborty, G., Wang, Y., Zhao, H., Herrmann, A., Zheng, L., 2020. Four‐Dimensional Deoxyribonucleic Acid–Gold Nanoparticle Assemblies. Angew. Chem. Int. Ed. 59(39), 17250–17255.

Mavrikou, S., Moschopoulou, G., Tsekouras, V., Kintzios, S., 2020. Development of a Portable, Ultra-Rapid and Ultra-Sensitive Cell-Based Biosensor for the Direct Detection of the SARS-CoV-2 S1 Spike Protein Antigen. Sensors 20(11), 3121.

Miao, L., Zhu, C., Jiao, L., Li, H., Du, D., Lin, Y., Wei, Q., 2018. Smart drug delivery system-inspired enzyme-linked immunosorbent assay based on fluorescence resonance energy transfer and allochroic effect induced dual-modal colorimetric and fluorescent detection. Anal. Chem. 90(3), 1976-1982.

Morya, V., Walia, S., Mandal, B.B., Ghoroi, C., Bhatia, D., 2020. Functional DNA based hydrogels: development, properties and biological applications. ACS Biomater. Sci. Eng. 6(11), 6021–6035.

Nagaich, U., 2018. Polymeric nanocapsules: An emerging drug delivery system. J. Adv. Pharm. Technol. Res. 9(3), 65.

Nasrin, F., Chowdhury, A.D., Ganganboina, A.B., Achadu, O.J., Hossain, F., Yamazaki, M., Park, E.Y., 2020. Fluorescent and electrochemical dual-mode detection of Chikungunya virus E1 protein using fluorophore-embedded and redox probe-encapsulated liposomes. Microchimica Acta 187(12), 1−11.

Nawaz, M.H., Hayat, A., Catanante, G., Latif, U., Marty, J.L., 2018. Development of a portable and disposable NS1 based electrochemical immunosensor for early diagnosis of dengue virus. Anal. Chim. Acta 1026, 1-7.

Nguyen, T.T.-Q., Kim, E.R., Gu, M.B., 2022. A new cognate aptamer pair-based sandwich-type electrochemical biosensor for sensitive detection of Staphylococcus aureus. Biosens. Bioelectron. 198, 113835.

Oaew, S., Charlermroj, R., Pattarakankul, T., Karoonuthaisiri, N., 2012. Gold nanoparticles/horseradish peroxidase encapsulated polyelectrolyte nanocapsule for signal amplification in Listeria monocytogenes detection. Biosensors and Bioelectronics 34(1), 238–243.

Oh, S., Kim, J., Tran, V.T., Lee, D.K., Ahmed, S.R., Hong, J.C., Lee, J., Park, E.Y., Lee, J., 2018. Magnetic nanozyme-linked immunosorbent assay for ultrasensitive influenza A virus detection. ACS Appl. Mater. Interfaces 10(15), 12534-12543.

Ohfuji, S., Kondo, K., Ito, K., Kase, T., Maeda, A., Fukushima, W., Masuda, T., Kano, M., 2019. Nationwide epidemiologic study of norovirus-related hospitalization among Japanese older adults. BMC infectious diseases 19(1), 400.

Pachfule, P., Kandambeth, S., Díaz, D.D., Banerjee, R., 2014. Highly stable covalent organic framework–Au nanoparticles hybrids for enhanced activity for nitrophenol reduction. Chemical Communications 50(24), 3169-3172.

Panferov, V.G., Safenkova, I.V., Zherdev, A.V., Dzantiev, B.B., 2021. The steadfast Au@ Pt soldier: Peroxide-tolerant nanozyme for signal enhancement in lateral flow immunoassay of peroxidase-containing samples. Talanta 225, 121961.

Pang, B., Xu, J., Liu, Y., Peng, H., Feng, W., Cao, Y., Wu, J., Xiao, H., Pabbaraju, K., Tipples, G., 2020. Isothermal amplification and ambient visualization in a single tube for the detection of SARS-CoV-2 using loop-mediated amplification and CRISPR technology. Analytical Chemistry 92(24), 16204-16212.

Parkash, O., Abdullah, M.A., Yean, C.Y., Sekaran, S.D., Shueb, R.H., 2021. Development and Evaluation of an Electrochemical Biosensor for Detection of Dengue-Specific IgM Antibody in Serum Samples. Diagnostics 11(1), 33.

Petersen, E., Koopmans, M., Go, U., Hamer, D.H., Petrosillo, N., Castelli, F., Storgaard, M., Al Khalili, S., Simonsen, L., 2020. Comparing SARS-CoV-2 with SARS-CoV and influenza pandemics. Lancet Infect. Dis.

Qiu, G., Gai, Z., Tao, Y., Schmitt, J., Kullak-Ublick, G.A., Wang, J., 2020. Dual-functional plasmonic photothermal biosensors for highly accurate severe acute respiratory syndrome coronavirus 2 detection. ACS Nano 14(5), 5268–5277.

Ramana, D., Capoor, A., Sashidhar, R., Bhat, R.V., 1995. Limitations in the use of horseradish peroxidase as an enyzme probe in the development of a homogeneous immunoassay for aflatoxin B 1. Fresenius' journal of analytical chemistry 352(1-2), 43-48.

Ren, R., Cai, G., Yu, Z., Zeng, Y., Tang, D., 2018. Metal-polydopamine framework: an innovative signal-generation tag for colorimetric immunoassay. Anal. Chem. 90(18), 11099-11105.

Rodovalho, V., Araujo, G., Vaz, E., Ueira-Vieira, C., Goulart, L., Madurro, J., Brito-Madurro, A., 2018. Peptide-based electrochemical biosensor for juvenile idiopathic arthritis detection. Biosens. Bioelectron. 100, 577–582.

Russo, L., Leva Bueno, J., Bergua, J.F., Costantini, M., Giannetto, M., Puntes, V., de la Escosura-Muñiz, A., Merkoçi, A., 2018. Low-Cost Strategy for the Development of a Rapid Electrochemical Assay for Bacteria Detection Based on AuAg Nanoshells. ACS Omega 3(12), 18849-18856.

Salatin, S., Barar, J., Barzegar-Jalali, M., Adibkia, K., Kiafar, F., Jelvehgari, M., 2017. Development of a nanoprecipitation method for the entrapment of a very water soluble drug into Eudragit RL nanoparticles. Res. Pharm. Sci. 12(1), 1.

Samuni, A., Maimon, E., Goldstein, S., 2017. Mechanism of HRP-catalyzed nitrite oxidation by H2O2 revisited: Effect of nitroxides on enzyme inactivation and its catalytic activity. Free Radical Biology and Medicine 108, 832–839.

Santos, A., Bueno, P.R., Davis, J.J., 2018. A dual marker label free electrochemical assay for Flavivirus dengue diagnosis. Biosens. Bioelectron. 100, 519-525.

Seo, G., Lee, G., Kim, M.J., Baek, S.-H., Choi, M., Ku, K.B., Lee, C.-S., Jun, S., Park, D., Kim, H.G., 2020. Rapid detection of COVID-19 causative virus (SARS-CoV-2) in human nasopharyngeal swab specimens using field-effect transistor-based biosensor. ACS Nano 14(4), 5135–5142.

Sercombe, L., Veerati, T., Moheimani, F., Wu, S.Y., Sood, A.K., Hua, S., 2015. Advances and challenges of liposome assisted drug delivery. Front. Pharmacol. 6, 286.

Shams Nateri, A., Ekrami, E., 2008. Determination of bicomponent dye solutions by means of zero‐crossing‐point derivative spectrophotometry. Color Res. Appl. 33(4), 307–311.

Shang, J., Gao, X., 2014. Nanoparticle counting: towards accurate determination of the molar concentration. Chem. Soc. Rev. 43(21), 7267–7278.

Sheibani, S., Capua, L., Kamaei, S., Akbari, S.S.A., Zhang, J., Guerin, H., Ionescu, A.M., 2021. Extended gate field-effect-transistor for sensing cortisol stress hormone. Commun. Mater. 2(1), 1–10.

Shen, S., Wu, Y., Liu, Y., Wu, D., 2017. High drug-loading nanomedicines: progress, current status, and prospects. Int. J. Nanomed. 12, 4085.

Stern, E., Vacic, A., Li, C., Ishikawa, F.N., Zhou, C., Reed, M.A., Fahmy, T.M., 2010. A nanoelectronic enzyme‐linked immunosorbent assay for detection of proteins in physiological solutions. small 6(2), 232-238.

Sun, Y., Zheng, L., Yang, Y., Qian, X., Fu, T., Li, X., Yang, Z., Yan, H., Cui, C., Tan, W., 2020. Metal–Organic Framework Nanocarriers for Drug Delivery in Biomedical Applications. Nano-Micro Lett. 12, 1–29.

Suthanthiraraj, P.P.A., Sen, A.K., 2019. Localized surface plasmon resonance (LSPR) biosensor based on thermally annealed silver nanostructures with on-chip blood-plasma separation for the detection of dengue non-structural protein NS1 antigen. Biosens. Bioelectron. 132, 38–46.

Suzuki, A., Mizumoto, K., Akhmetzhanov, A.R., Nishiura, H., 2019. Interaction Among Influenza Viruses A/H1N1, A/H3N2, and B in Japan. Int. J. Environ. Res. Public Health 16(21), 4179.

Taghdisi, S.M., Danesh, N.M., Nameghi, M.A., Ramezani, M., Alibolandi, M., Hassanzadeh-Khayat, M., Emrani, A.S., Abnous, K., 2019. A novel electrochemical aptasensor based on nontarget-induced high accumulation of methylene blue on the surface of electrode for sensing of α-synuclein oligomer. Biosens. Bioelectron. 123, 14–18.

Takemura, K., Adegoke, O., Takahashi, N., Kato, T., Li, T.-C., Kitamoto, N., Tanaka, T., Suzuki, T., Park, E.Y., 2017. Versatility of a localized surface plasmon resonance-based gold nanoparticle-alloyed quantum dot nanobiosensor for immunofluorescence detection of viruses. Biosens. Bioelectron. 89, 998–1005.

Takemura, K., Ganganboina, A.B., Khoris, I.M., Chowdhury, A.D., Park, E.Y., 2021. Plasmon Nanocomposite-Enhanced Optical and Electrochemical Signals for Sensitive Virus Detection. ACS Sens. 6(7), 2605–2612.

Tang, Q., Zhang, L., Tan, X., Jiao, L., Wei, Q., Li, H., 2019. Bioinspired synthesis of organic–inorganic hybrid nanoflowers for robust enzyme-free electrochemical immunoassay. Biosens. Bioelectron. 133, 94-99.

Tao, Y., Lin, Y., Huang, Z., Ren, J., Qu, X., 2013. Incorporating Graphene Oxide and Gold Nanoclusters: A Synergistic Catalyst with Surprisingly High Peroxidase‐Like Activity Over a Broad pH Range and its Application for Cancer Cell Detection. Advanced materials 25(18), 2594-2599.

Tate, J., Ward, G., 2004. Interferences in immunoassay. The clinical biochemist reviews 25(2), 105.

Vázquez-Guardado, A., Mehta, F., Jimenez, B., Biswas, A., Ray, K., Baksh, A., Lee, S., Saraf, N., Seal, S., Chanda, D., 2021. DNA-Modified Plasmonic Sensor for the Direct Detection of Virus Biomarkers from the Blood. Nano Lett. 21(18), 7505–7511.

Venkataramanan, N.S., 2016. Cooperativity of intermolecular hydrogen bonds in microsolvated DMSO and DMF clusters: a DFT, AIM, and NCI analysis. J. Mol. Model. 22(7), 151.

Vysotskii, V., Uryupina, O.Y., Gusel'nikova, A., Roldugin, V., 2009. On the feasibility of determining nanoparticle concentration by the dynamic light scattering method. Colloid J. 71(6), 739.

Wang, C., Gao, J., Tan, H., 2018a. Integrated antibody with catalytic metal–organic framework for colorimetric immunoassay. ACS Appl. Mater. Interfaces 10(30), 25113-25120.

Wang, C., Zhao, Q., 2020. A reagentless electrochemical sensor for aflatoxin B1 with sensitive signal-on responses using aptamer with methylene blue label at specific internal thymine. Biosens. Bioelectron. 167, 112478.

Wang, H., Fu, W., Chen, Y., Xue, F., Shan, G., 2021. ZIF-67-derived Co3O4 hollow nanocage with efficient peroxidase mimicking characteristic for sensitive colorimetric biosensing of dopamine. Spectrochimica Acta Part A: Molecular and Biomolecular Spectroscopy 246, 119006.

Wang, H., Wan, K., Shi, X., 2018b. Recent advances in nanozyme research. Advanced Materials, 1805368.

Wang, R., Ongagna-Yhombi, S.Y., Lu, Z., Centeno-Tablante, E., Colt, S., Cao, X., Ren, Y., Cárdenas, W.B., Mehta, S., Erickson, D., 2019. Rapid diagnostic platform for colorimetric differential detection of dengue and Chikungunya viral infections. Anal. Chem. 91(8), 5415–5423.

Wang, S., Chen, W., Liu, A.L., Hong, L., Deng, H.H., Lin, X.H., 2012. Comparison of the peroxidase‐like activity of unmodified, amino‐modified, and citrate‐capped gold nanoparticles. ChemPhysChem 13(5), 1199-1204.

Wang, S., Chen, Z., Choo, J., Chen, L., 2016. Naked-eye sensitive ELISA-like assay based on gold-enhanced peroxidase-like immunogold activity. Anal. Bioanal.Chem. 408(4), 1015-1022.

Wasik, D., Mulchandani, A., Yates, M.V., 2018. Point-of-use nanobiosensor for detection of dengue virus NS1 antigen in adult Aedes aegypti: a potential tool for improved dengue surveillance. Anal. Chem. 90(1), 679–684.

Weerathunge, P., Ramanathan, R., Torok, V.A., Hodgson, K., Xu, Y., Goodacre, R., Behera, B.K., Bansal, V., 2019. Ultrasensitive colorimetric detection of murine norovirus using NanoZyme aptasensor. Anal. Chem. 91(5), 3270–3276.

Wei, T., Du, D., Zhu, M.-J., Lin, Y., Dai, Z., 2016. An improved ultrasensitive enzyme-linked immunosorbent assay using hydrangea-like antibody–enzyme–inorganic three-in-one nanocomposites. ACS Appl. Mater. Interfaces 8(10), 6329–6335.

WHO, W., 2015. WHO estimates of the global burden of foodborne diseases: foodborne disease burden epidemiology reference group 2007–2015. Geneva, Switzerland.

Wu, K., Liu, J., Saha, R., Su, D., Krishna, V.D., Cheeran, M.C.-J., Wang, J.-P., 2020. Magnetic Particle Spectroscopy for Detection of Influenza A Virus Subtype H1N1. ACS Appl. Mater. Interfaces 12(12), 13686–13697.

Wu, L., Wan, G., Hu, N., He, Z., Shi, S., Suo, Y., Wang, K., Xu, X., Tang, Y., Wang, G., 2018. Synthesis of porous CoFe2O4 and its application as a peroxidase mimetic for colorimetric detection of H2O2 and organic pollutant degradation. Nanomaterials 8(7), 451.

Wu, L., Yin, W., Tang, K., Li, D., Shao, K., Zuo, Y., Ma, J., Liu, J., Han, H., 2016. Enzymatic biosensor of horseradish peroxidase immobilized on Au-Pt nanotube/Au-graphene for the simultaneous determination of antioxidants. Analytica chimica acta 933, 89-96.

Wu, Z., Zeng, T., Guo, W.-J., Bai, Y.-Y., Pang, D.-W., Zhang, Z.-L., 2019. Digital single virus immunoassay for ultrasensitive multiplex avian influenza virus detection based on fluorescent magnetic multifunctional nanospheres. ACS Appl. Mater. Interfaces 11(6), 5762–5770.

Xi, Z., Wei, K., Wang, Q., Kim, M.J., Sun, S., Fung, V., Xia, X., 2021. Nickel–Platinum Nanoparticles as Peroxidase Mimics with a Record High Catalytic Efficiency. Journal of the American Chemical Society 143(7), 2660-2664.

Xia, X., Zhang, J., Lu, N., Kim, M.J., Ghale, K., Xu, Y., McKenzie, E., Liu, J., Ye, H., 2015. Pd–Ir core–shell nanocubes: a type of highly efficient and versatile peroxidase mimic. ACS Nano 9(10), 9994-10004.

Xu, L., Chopdat, R., Li, D., Al-Jamal, K.T., 2020a. Development of a simple, sensitive and selective colorimetric aptasensor for the detection of cancer-derived exosomes. Biosens. Bioelectron. 169, 112576.

Xu, S., Ouyang, W., Xie, P., Lin, Y., Qiu, B., Lin, Z., Chen, G., Guo, L., 2017. Highly uniform gold nanobipyramids for ultrasensitive colorimetric detection of influenza virus. Anal. Chem. 89(3), 1617–1623.

Xu, W., Jiao, L., Ye, H., Guo, Z., Wu, Y., Yan, H., Gu, W., Du, D., Lin, Y., Zhu, C., 2020b. pH-responsive allochroic nanoparticles for the multicolor detection of breast cancer biomarkers. Biosens. Bioelectron. 148, 111780.

Yakes, B.J., Papafragkou, E., Conrad, S.M., Neill, J.D., Ridpath, J.F., Burkhardt III, W., Kulka, M., DeGrasse, S.L., 2013. Surface plasmon resonance biosensor for detection of feline calicivirus, a surrogate for norovirus. International journal of food microbiology 162(2), 152–158.

Yan, H., Jiao, L., Wang, H., Xu, W., Wu, Y., Gu, W., Du, D., Lin, Y., Zhu, C., 2019. A “sense-and-treat” ELISA using zeolitic imidazolate framework-8 as carriers for dual-modal detection of carcinoembryonic antigen. Sens. Actuators, B 297, 126760.

Yanagisawa, N., Wada, K., Spengler, J.D., Sanchez-Pina, R., 2018. Health preparedness plan for dengue detection during the 2020 summer Olympic and Paralympic games in Tokyo. PLoS Negl.Trop. Dis. 12(9), e0006755.

Yao, Y., Chen, X., Zhang, X., Liu, Q., Zhu, J., Zhao, W., Liu, S., Sui, G., 2020. Rapid Detection of Influenza Virus Subtypes Based on an Integrated Centrifugal Disc. ACS Sens. 5(5), 1354–1362.

Ye, H., Yang, K., Tao, J., Liu, Y., Zhang, Q., Habibi, S., Nie, Z., Xia, X., 2017. An enzyme-free signal amplification technique for ultrasensitive colorimetric assay of disease biomarkers. ACS Nano 11(2), 2052-2059.

Yeh, J.-Y., Matsagar, B.M., Chen, S.S., Sung, H.-L., Tsang, D.C., Li, Y.-P., Wu, K.C.-W., 2020. Synergistic effects of Pt-embedded, MIL-53-derived catalysts (Pt@ Al2O3) and NaBH4 for water-mediated hydrogenolysis of biomass-derived furfural to 1, 5-pentanediol at near-ambient temperature. Journal of Catalysis 390, 46-56.

Zhan, L., Guo, S.-z., Song, F., Gong, Y., Xu, F., Boulware, D.R., McAlpine, M.C., Chan, W.C., Bischof, J.C., 2017. The role of nanoparticle design in determining analytical performance of lateral flow immunoassays. Nano letters 17(12), 7207-7212.

Zhang, H., Miller, B.L., 2019. Immunosensor-based label-free and multiplex detection of influenza viruses: State of the art. Biosens. Bioelectron. 141, 111476.

Zhang, X., Zhi, H., Zhu, M., Wang, F., Meng, H., Feng, L., 2021. Electrochemical/visual dual-readout aptasensor for Ochratoxin A detection integrated into a miniaturized paper-based analytical device. Biosens. Bioelectron. 180, 113146.

Zhang, Y., Wang, H., Stewart, S., Jiang, B., Ou, W., Zhao, G., He, X., 2019. Cold-Responsive Nanoparticle Enables Intracellular Delivery and Rapid Release of Trehalose for Organic-Solvent-Free Cryopreservation. Nano Lett. 19(12), 9051-9061.

Zhang, Z., Dong, L., Zhu, Q., 2018. Rational engineering of synergically stabilized aptamer-cDNA duplex probes for strand displacement based electrochemical sensors. Electrochim. Acta 282, 588–594.

Zheng, A.-X., Cong, Z.-X., Wang, J.-R., Li, J., Yang, H.-H., Chen, G.-N., 2013. Highly-efficient peroxidase-like catalytic activity of graphene dots for biosensing. Biosensors and Bioelectronics 49, 519–524.

Zhou, Y., Liu, B., Yang, R., Liu, J., 2017. Filling in the gaps between nanozymes and enzymes: challenges and opportunities. Bioconjugate Chem. 28(12), 2903-2909.

Zhu, L., Liu, X., Yang, J., He, Y., Li, Y., 2020a. Application of Multiplex Microfluidic Electrochemical Sensors in Monitoring Hematological Tumor Biomarkers. Anal. Chem. 92(17), 11981–11986.

Zhu, X., Wang, X., Han, L., Chen, T., Wang, L., Li, H., Li, S., He, L., Fu, X., Chen, S., 2020b. Multiplex reverse transcription loop-mediated isothermal amplification combined with nanoparticle-based lateral flow biosensor for the diagnosis of COVID-19. Biosensors and Bioelectronics 166, 112437.